Modification of Parallel Blade-Vortex Interactions Using Leading Edge Blowing

Christopher Weiland

Thesis submitted to the faculty of the Virginia Polytechnic Institute and State University in partial fulfillment of the requirements for the degree of

Master of Science
In
Mechanical Engineering

Approved By:

Dr. Pavlos Vlachos, Committee Chair
Dr. Demetri Telionis
Dr. Martin Johnson

December 14, 2006
Blacksburg, Virginia

Keywords: Leading Edge Blowing, Digital Particle Image Velocimetry, Blade-Vortex Interaction

Copyright 2006, Christopher Weiland

Modification of Blade-Vortex Interactions Using Leading Edge Blowing

Christopher Weiland

ABSTRACT

The interaction of an unsteady wake with a solid body can induce sizable loading of the structure, which has many detrimental side effects in both the structural and acoustic senses. These interactions are ubiquitous in nature and engineering. A flow control technique is sought to mitigate this interaction, thereby decreasing the level of structural vibration.

This thesis investigates the effectiveness of steady leading-edge blowing (LEB) flow control for modifying the vortex induced vibrations on an airfoil in the wake of a circular cylinder. The airfoil was allowed to oscillate perpendicular to the fluid flow direction in response to the impinging Von-Karman vortex street. The flow field and airfoil vibrations were simultaneously captured using Digital Particle Image Velocimetry (DPIV) and accelerometer measurements in a time-resolved sense. The results indicate that LEB can significantly reduce the degree of unsteady loading due to the blade vortex interaction (BVI). In some cases, the LEB jet appears to break the coherency of a vortex incident on the airfoil, and in other cases the jet increase the mean stand-off distance of the vortex as it convects over the airfoil surface. It was also found that, for large circular cylinders, if the airfoil is within the mean closure point of the circular cylinder wake, the LEB can increase the level of BVI.

The Proper Orthogonal Decomposition (POD) was also used to analyze the DPIV data. POD is mathematically superior for reducing a data rich field into fundamental modes; a suitable basis function for the reduction is chosen mathematically and it is not left to the researcher to pick the basis function. A comparison of the energy in these modes is useful in ascertaining the dynamics of the BVI. For one of the two cases examined with POD, it was found for no LEB the fundamental (i.e. most energetic) mode is given by the vortex shedding of the circular cylinder upstream. The addition of LEB reduces the energy contained in this fundamental mode. Thus the LEB jet has the effect of reducing the flow field coherency; the structure of the large vortices is broken up into smaller vortices. For the other case, the LEB jet has the opposite effect: the jet has the ability to organize the circular cylinder wake into coherent structures. This acts to increase the coherency of the circular cylinder wake and increases the level of BVI.

This thesis is organized as follows. The first chapter contains the complete DPIV analysis of the LEB for several sizes of circular cylinders and blowing coefficients. A subset of the work presented in this first chapter was presented at the 2006 ASME FEDSM meeting in Miami, Florida. The second chapter presents the POD analysis of two specific cases analyzed in the first chapter. The information contained in the second chapter is to be presented at the 2007 ASME FEDSM meeting in San Diego, California. As space requirements for the ASME paper limited the amount of information that could be presented in that meeting, the Appendix contains additional information on the POD analysis of the cases presented in Chapter 2.

Acknowledgements

I would like to extend my thanks to Techsburg, in particular Dr. John Fleming and Dr. Jason Anderson, for funding this research project. It has been a pleasure to work with both of you. I have learned much from our conversations regarding this research and feel lucky to have been given the opportunity to work on this research project.

I would also like to thank my committee members, namely Dr. Pavlos Vlachos, Dr. Demetri Telionis, and Dr. Martin Johnson, for their help in advising and conducting this research. I thank Dr. Andrew Duggleby for help in understanding the nature and significance of the Proper Orthogonal Decomposition (POD) results, which has provided a wealth of information. In particular, I would like to thank my committee chair, Dr. Pavlos Vlachos, for allowing me the opportunity to further my education under his guidance.

Several of the graduate students here at the Complex ThermoFluids Systems Laboratory (CTFS) have been instrumental in helping this research proceed smoothly. Dr. Ali Etebari and Jose Rullan, being the senior laboratory members when I first arrived, helped assimilate me into the "graduate student lifestyle." I appreciate all of the time you both took to help me. I thank John Charonko for the use of his POD code, which has provided an interesting dynamic to the analysis of this data. In fact, the CTFS group as a whole has, in some way or another, been vital to the success of this project. I thank you all for your help, and can only hope that I have been as good a friend to you as you have been to me. Our daily interactions helped me to retain my sanity (albeit in a limited capacity).

Although this work is of my own effort, much of the Digital Particle Image Velocimetry presented herein was taken with the help of Patrick Leung, a former graduate student here at CTFS. Anyone who knew Patrick can certainly attest that his passing came much too soon. Patrick was an excellent student, researcher, and most importantly, a good friend to all who knew him. He is deeply missed by all whose life was touched by his kindness, selflessness, and generosity. I learned much from him in the short time I was blessed to have known him. I sincerely thank him for all of his help with this research, and for his friendship, which I will always remember.

Table of Contents

Table of Figures

Table of Tables

Nomenclature

c, L = airfoil chord length
C_μ = blowing momentum coefficient
d = miss distance of the vortex over the airfoil
D = cylinder diameter
f_s = cylinder shedding frequency
h_{slot} = flow control jet slot height
l = section of airfoil over which BVI occurs
L = lift per unit length of the airfoil
t = airfoil maximum thickness
t_{ref} = relative time for DPIV images
t^* = noise disturbance reception time
U_∞ = freestream velocity
U_j = flow control jet velocity
v = component of velocity normal to freestream
x = observer position in airfoil fixed frame
X = position parallel to airfoil chord
y, Y = position orthogonal to airfoil chord
Γ = vortex circulation
ρ_∞ = freestream density

1 Digital Particle Image Velocimetry Analysis of Blade-Vortex Interactions with Leading Edge Blowing

1.1 INTRODUCTION

The interaction of an unsteady wake with a body can induce sizable loading of the structure, and can have many detrimental side effects. For example, the familiar "chopping" sound of helicopters is attributed to the interaction of a vortex with a helicopter blade, known in the community as blade slap noise (Preisser et al, 1994; Abello and George 2003). This situation is commonly referred to as a blade vortex interaction (BVI). More precisely, a tip vortex is generated by a rotor upstream of another rotor due to the pressure difference between the upper and lower lifting surfaces. The tip vortex induces an unsteady pressure projection onto a subsequent rotor as it sweeps through its revolution (Figure 1.1). The extent of this pressure loading determines the degree of unsteady lift and rotor vibration, and thus radiated noise.

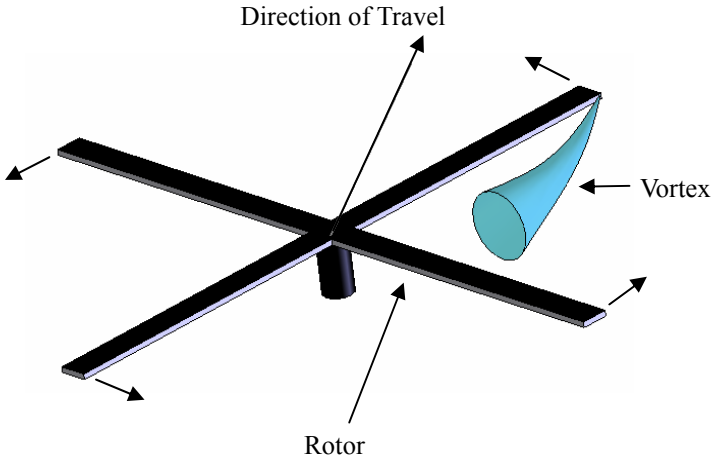

Figure 1.1. Helicopter BVI model.

BVI is inherently an unsteady three-dimensional problem. It has been shown that the most unfavorable situation for blade loading occurs when the axis of the vortex filament is parallel to the span of the blade (Kuo and Hsiesh, 1994; Hardin and Lamkin, 1986). This orientation is termed the parallel interaction (Figure 1.2).

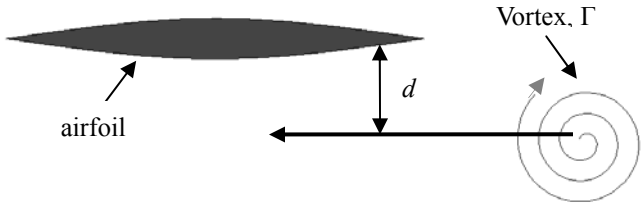

Figure 1.2. Parallel BVI problem parameters.

The incident vortex can influence the rotor in two ways. The first is a direct collision, in which the vortex strikes the airfoil and is split. The vortex disintegrates and pressure loading of the airfoil is reduced. The impinging vortex can induce secondary vortices, which can also play a role in the development of the major vortices traveling over the airfoil surface (Rockwell, 1998; Horner et al, 1996). The second case occurs when the vortex passes very near the airfoil surface. In this case, the vortex maintains its character for a longer

distance over the airfoil and loading is substantially increased (Wilder and Telionis, 1998). Fundamental studies of the BVI have been studied from a two-dimensional standpoint, such as in this experiment (Bull et al, 1996 and Wilder and Telionis, 1998) and in the three-dimensional sense, whereby a streamwise vortex passes close to a solid body (Mayori and Rockwell, 1994 and Wittmer and Devenport, 1995). These studies do much to further our understanding of how a vortex passes close to a body, but do not address the elimination of the forcing vortex to decrease the level of BVI. It is important to note that the noise generated during the helicopter flight is due to two parts: the interaction of the blade with the vortex in a parallel sense (BVI), and the interaction of the blade with the vortex in a streamwise sense, termed a blade wake interaction (BWI). The BVI is certainly the more dominant of the two forms of noise generation. The BVI causes an apparent angle of attack seen by the airfoil, and because this interaction occurs so quickly very distinctive frequencies are generated as a result of the impulsive interaction. The BWI results in the generation of broadband noise (Wittmer and Devenport, 1995).

There are several factors which influence the degree of unsteady loading on the airfoil or rotor. Hardin and Lampkin studied the BVI problem in a simplified two dimensional, shock free model and deduced that that noise radiation, or acoustic pressure time history due to the BVI is (Hardin and Lamkin, 1986)

$$p(x,t^*) \approx \frac{\Gamma L l}{\rho_\infty d^2} \tag{1.1}$$

Here Γ is the incident vortex strength, L is the lift per unit length of the blade, l is the interaction length (i.e. the length over which the vortex affects the airfoil), ρ_∞ is the density of the local fluid, and d is the stand-off distance between the vortex and the blade surface.

It is immediately apparent that there are several methods for reducing the noise generation due to BVI, the most practical being reducing the vortex strength, decreasing the lift placed on the airfoil, or increasing the distance between the vortex and the airfoil.

Decreasing the tip vortex strength has received much attention over the years, whether by blowing (Liu et al., 1999; Liu et al., 2001), winglets or spoilers (Smith and Sigl, 1995; Mullins et al., 1996), or by changing the blade shape itself (Liu et al., 2001). The purpose of these ideas is to diffuse or spread out the vortex so that the degree of BVI is lessened. However, a lifting body must produce a tip vortex due to the pressure difference between the upper and lower lifting surfaces, and any attempt to altar the tip vortex strength or structure will most likely result in increased drag and torque requirements for the helicopter. Smith and Sigl (1995) showed that passive wing devices can diffuse the tip vortex by as much as 20% with an 8% increase in drag. Active devices diffused the tip vortex over 50%, such as the "NASA star tip," which diffused the tip vortex 100% but incurred a performance penalty of a 67% increase in airfoil drag. However, the "stubwing" design diffused the tip vortex by 47% with a 9% decrease in drag. Thus with proper design, it seems likely that devices can effectively lower the vortex strength with minimal aerodynamic penalties.

Changing the lift of the airfoil can be accomplished using a number of methods, such as increasing the total number of rotors, increasing the length of each rotor, or reducing the weight of the helicopter (Hardin and Lamkin, 1986). It should be pointed out that the reduction in lift only need take place at the location of the BVI. The interaction normally takes place over about 10% of the airfoil span (Lee, 1994), but the location along the span of the airfoil at which the interaction takes place can change during different flight maneuvers.

One of the most important parameters governing the BVI problem is the miss, or stand-off, distance between the airfoil and vortex. This conclusion is intuitively correct, as it makes sense that increasing the distance between the unsteady event and the airfoil will no doubt decrease the unsteady loading on the airfoil. With Hardin and Lamkin's model of the BVI, it was shown that doubling the miss distance will result in a 12 dB reduction in noise (1996). Malovrh and Gandhi (2005) showed that by increasing the vortex stand-off distance from zero (i.e., the blade penetrates the vortex) to half a chord length, a 14.4 dB reduction in BVI noise

is attained. They also showed that changing the miss distance of the convecting vortex resulted in little reduction as long as the vortex was penetrated by the airfoil. Ideas for increasing the miss distance include active trailing edge flaps to influence the vortex trajectory, and thus the miss distance. Hassan et al report noise reductions of 5 dB through the use of the trailing edge flaps (Hassan et al., 1992). However, the trailing edge flaps introduced a 58% penalty in the power requirements. Other ideas include the higher harmonic blade pitch control method, whereby the blade pitch angle is varied via excitation of a smart material embedded in the rotor. By aeroelastic deformation the blade pitch can be controlled and the miss distance is increased. Thus, the BVI noise is reduced and tests have shown reductions on the order of 6 dB, but this is at the expense of increased vibration levels and low frequency noise addition (Yu, 1996).

The underlying problem of the BVI is that the exciting vortex in the rotor wake maintains its coherency during the interaction and is allowed to project its unsteady pressure loading onto the airfoil. If the trailing vortex were destroyed before it were allowed to interact with the airfoil, its vorticity would rapidly diffuse and its effect on the blade loading would be dramatically decreased. Leading Edge Blowing (LEB) is a concept developed to minimize the interaction of an unsteady wake with an airfoil. In this idea, the airfoil blows a continuous jet upstream against the wake motion. The idea can potentially reduce the BVI in one of two methods. The first is elimination of the vortex itself. In this scenario, the jet will break up the vortex due to collision, which mimics the effects of a head-on vortex collision. The second method is to increase the miss distance of the airfoil either by moving the stagnation point of the airfoil upstream and establishing a "buffer zone" over the airfoil body, or angling the jet so as to push convecting vortices further from the airfoil surface. The effect of local lift decrease as a function of the LEB jet was not examined, but could also possibly contribute to a decrease in BVI. The concept of LEB for minimizing the BVI problem was experimentally studied and the results of this experiment are explored in this paper.

1.2 EXPERIMENTAL SETUP

The use of LEB flow control to limit the degree of interaction between a cylinder wake and an airfoil was studied using DPIV. The experiments simulate the interaction of an unsteady forcing wake and an airfoil. In addition to DPIV flow field measurements, the airfoil vibration was also measured at simultaneous points in time.

The experiments were conducted in a water tunnel in the Engineering Sciences and Mechanics fluid mechanics laboratory at Virginia Tech. The water tunnel is able to produce a freestream of up to 1 m/s with 3% turbulence within a test section of 2'x2'x5'. The experimental apparatus is shown in Figure 1.3. A double arc (sharp leading and trailing edge) airfoil with a chord of 3.4" and span of 8" was placed downstream and parallel to a circular cylinder at zero degrees angle of attack along the centerline of the circular cylinder. The airfoil is symmetric with a maximum thickness of 0.58"; airfoil parameters are given in Table 1.1. A slot, used for the injection of a water jet, runs almost the entire span of the airfoil and is located on the bottom side of the leading edge only. The airfoil is allowed to translate in response to the wake of the cylinder, and linear springs act to restore the airfoil to its rest position. The airfoil is constrained to move only in direction perpendicular to the flow direction by two rods on linear bearings. Two accelerometers are attached to a strut rigidly mounted to the airfoil. Plexiglas side walls are used to mitigate end effects of the airfoil and the circular cylinder and to permit optical access. The system was rigidly mounted in the test section and its natural frequency experimentally determined to be 12 Hz.

Table 1.1. Airfoil parameters.

airfoil slot height (m):	0.0016
airfoil slot length (m):	0.2007
airfoil area (m^2):	0.00032
airfoil thickness (m):	0.0147
airfoil chord (m):	0.0864
airfoil span (m):	0.2032

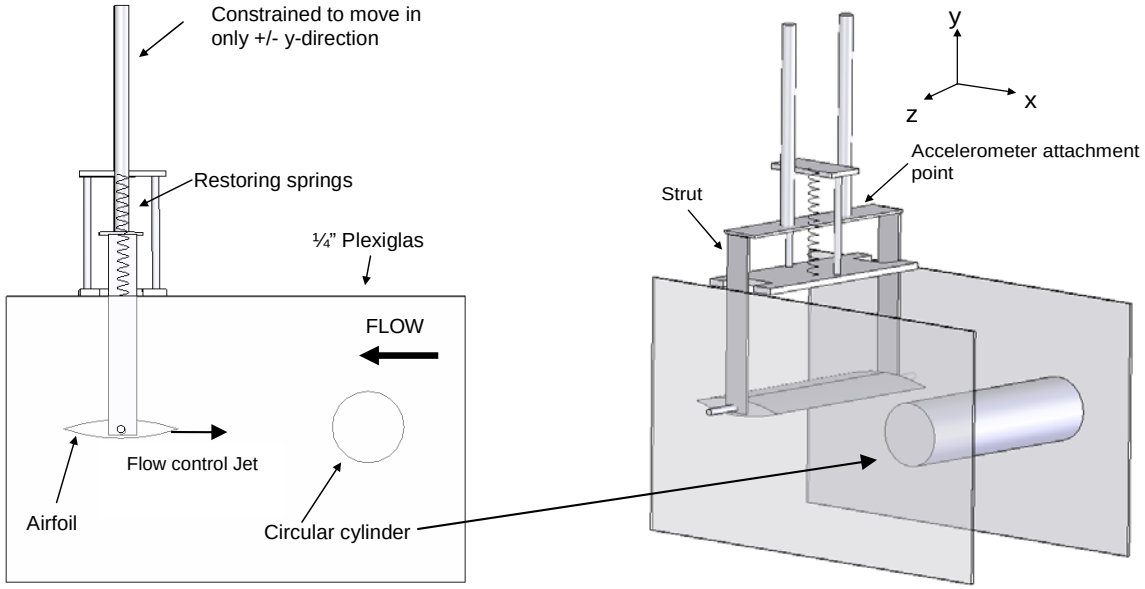

Figure 1.3. Experimental apparatus to study the LEB effect on a parallel BVI.

DPIV allows instantaneous point measurements of all velocity components in a planar interrogation region. Post processing of the data allows calculation of other flow variables, such as vorticity and shear stress. Thus, the velocity fluctuations at a point or entire field may be computed from the DPIV data time history. The DPIV measurements were taken for approximately 4.25 seconds at an 800 Hz sampling rate.

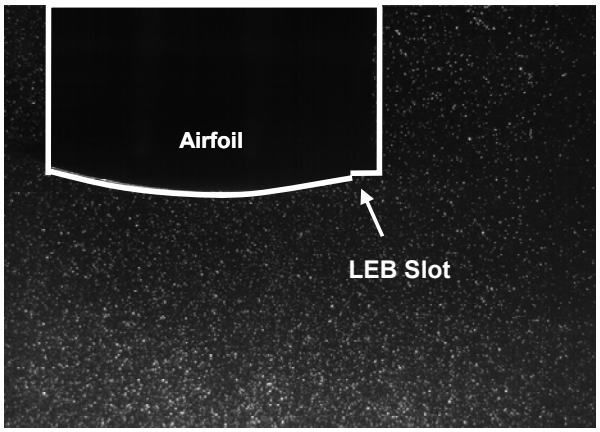

Figure 1.4. Typical DPIV raw image of the flow field.

The flow field was illuminated with a Lee Lasers 45W Nd:YAG laser, and a series of lenses and mirrors were employed to focus the beam and then open it again into a thin laser sheet of approximately 1 mm thickness

oriented in a plane parallel to the flow direction and perpendicular to the airfoil span. The flow was seeded with 11 micron neutrally buoyant spherical hollow glass particles with a specific gravity of 1.1, manufactured by Potters Industries. Motion of the particles was tracked with an IDT XS-3 high-speed camera. The interrogation region for the DPIV measurements was 1280 pixels by 964 pixels with a resolution of 121 μm/pixel. A sample raw image is shown in Figure 1.4. The images were processed using in-house developed DPIV software. An iterative multigrid DPIV algorithm was used using two passes of 32x32 pixel and 16x16 pixel interrogation windows respectively. The vector grid spacing was uniform at 8 pixels, for a total number of velocity vectors of 18369. The data were validated first using a median filter to remove significantly bad vectors and then several adaptive mean validation routines were performed. As seen in Figure 1.3 the cylinder and airfoil are contained by Plexiglas walls which permit optical clarity and help to reduce any three dimensionality of the flow.

Mean subtracted point velocity measurements in the flow field were analyzed using a power spectrum density routine written in MATLAB; this analysis allows us to identify the major frequency components in the flow field and comparison of these forcing frequencies with the ensuing airfoil vibration frequencies allows a determination of what is forcing the airfoil vibration. To measure the flow velocity and accelerometer spectra, the Hamming window function was used to resolve a lowest frequency of ½ Hz with 70% overlap between windows. To study the spectral components of the flow field around the airfoil, the following procedure is used. Given a point in the interrogation zone, the *v* component of the velocity fluctuations are computed using the power spectrum density routine as previously described. Each signal has a frequency spectrum indicative of the nature of the flow at that point. If we draw a line through that point transverse to the flow (Figure 1.5), and take the power spectrum density at each one of those points, we can analyze a slice of the spectral characteristics of the flow field (in a plane) that is incident on the airfoil. Note in Figure 1.5 that the frequency component is expressed as normalized by the Strouhal shedding frequency of the circular cylinder, and thus we can visualize the mean path of the vortices as they pass over the airfoil.

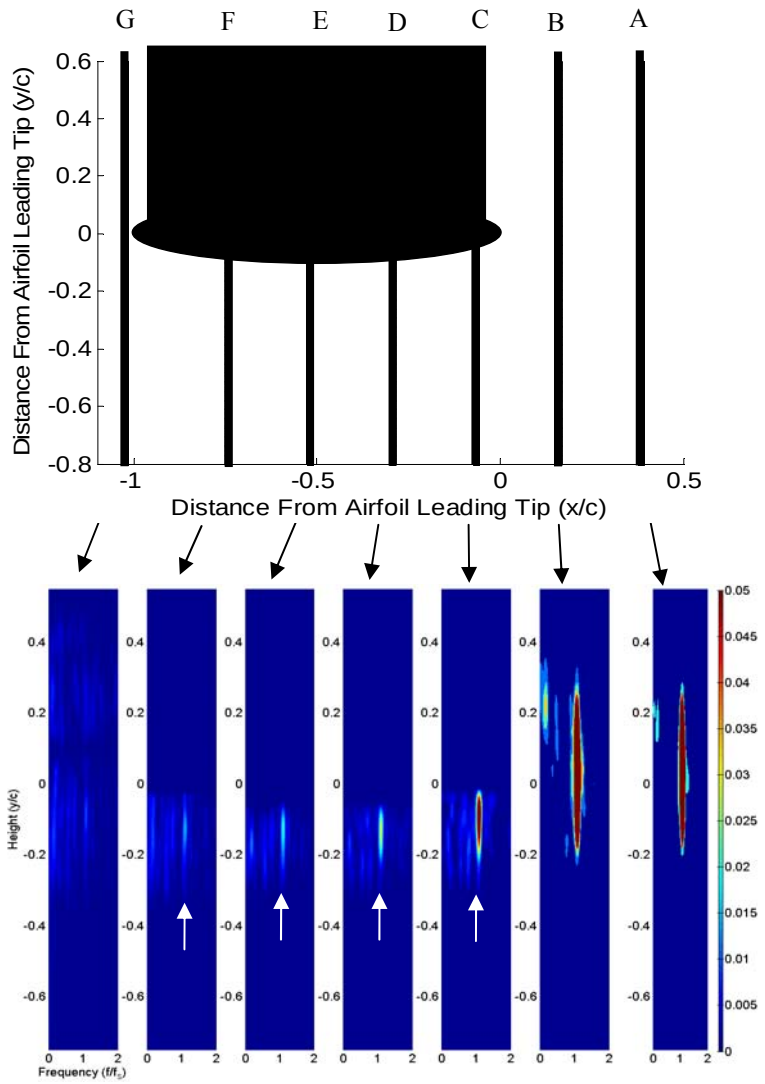

Figure 1.5. PSD interrogation planes for the *v* velocity component fluctuations.

Four circular cylinders (CC) of varying diameters were mounted upstream of the airfoil at the same mounting location (D_{wake}). The test matrix and calculated flow variables are shown in Table 1.2. Because of this, the level of the cylinder wake development varies from case to case. The same freestream velocity was kept constant between cases, so the Reynolds (Re) number and thus strength of the circular cylinder wake varies from case to case. Because of the variance in cross-flow Reynolds number (i.e. wake strength) and the distance between the tip of the airfoil and the circular cylinder, a quantitative comparison between cases is not possible, but within the realm of each circular cylinder diameter, a comparison on the effect of LEB on the airfoil vibrations is quantitatively possible. Note that the plane jets studied are turbulent as the transitional Reynolds number for a plane jet is 33 (Andrade, 1939). The circular cylinder shedding frequency (F_s) was calculated using the Strouhal relationship, shown in Equation (3). The non-dimensional distance reported in Table 1.2 is given by

$$D = \frac{D_{wake} - \left(\frac{D_{cyl}}{2}\right)}{\frac{D_{cyl}}{2}} \tag{2}$$

Table 1.2. LEB test matrix.

Cylinder Diameter (m, D_{cyl})	D	F_s (Hz)	Re (CC)	Plane Jet Velocity (m/s)	C_μ	Re (jet)
0.013	9.0	8.7	6985	0.00	0.00	0
				0.27	0.05	381
				0.44	0.14	638
				0.56	0.22	800
0.019	5.8	5.8	10478	0.00	0.00	0
				0.27	0.05	381
				0.44	0.14	638
				0.54	0.21	782
0.032	3.3	3.5	17463	0.00	0.00	0
				0.29	0.06	418
				0.44	0.14	638
				0.54	0.21	782
0.051	1.9	2.2	27940	0.00	0.00	0
				0.54	0.21	782

$$f_s = \frac{0.2U_\infty}{D} \tag{3}$$

The degree of jet blowing is reported using a momentum coefficient, C_μ, defined as

$$C_\mu = 2\frac{U_j^2 h_{slot}}{U_\infty^2 t} \tag{4}$$

Here U_j is the velocity of the water jet leaving the airfoil, h_{slot} is the height of the blowing slot, U_∞ is the freestream velocity incident on the airfoil, and t is the maximum airfoil thickness (approximately 0.5").

For the purpose of flow control, water was fed into the airfoil by two ¼ inch tubes on either side of the airfoil via two electronically controlled positive displacement pumps working in parallel and capable of delivering a maximum of 11 liters/min to the airfoil. The flow rate was recorded using an ultrasonic flow meter. The airfoil has a blowing slot on its leading edge located on the bottom side of the airfoil; the airfoil jet is asymmetric about its centerline.

1.3 EXPERIMENTAL RESULTS OF BVI MODIFICATION

This section presents the experimental results of the BVI modification as a result of the LEB. The test matrix is given in Table 1.2 and covers a wide range of shedding frequencies and wake strengths. Note that in all cases, the distance between the airfoil leading edge and the centerline of the circular cylinder remains constant. Thus, the distance between the leading edge of the airfoil and the circular cylinder does not remain constant. Because of this, it is difficult to make quantitative comparisons regarding the effects of the momentum coefficient and the circular cylinder size (i.e. wake strength) on the effectivness of LEB in a global sense. We can, however, compare each specific case individually and develop an idea for how the LEB jet effects the wake structure and how the wake structure affects the airfoil vibrations.

1.3.1 Results – Case 1

In this case, the circular cylinder diameter is on the order of the airfoil thickness with a shedding frequency of 8.7 Hz. It should be noted that this is close to the natural frequency of the system (12 Hz, see

Appendix I – Characterization of Test Apparatus), and thus changes in the vibration level of the airfoil will be strongly affected by even small changes in the interaction. The LEB is very effective at reducing airfoil vibrations as shown by Figure 1.6, which shows the percentage in the RMS velocity fluctuations of the airfoil as a function of C_μ. At a C_μ=0.22, the velocity fluctuations are reduced by about 60%.

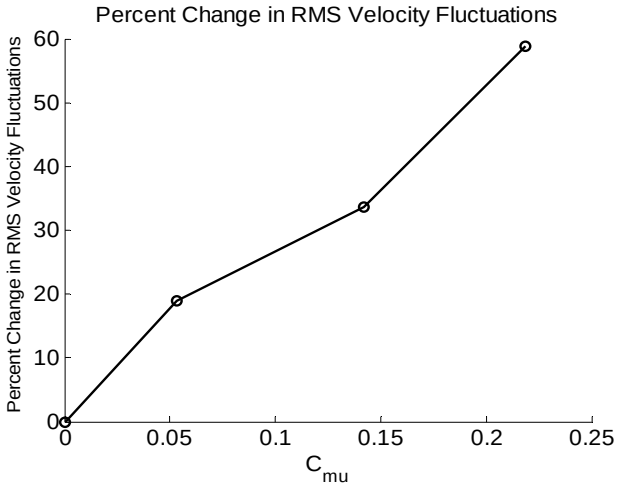

Figure 1.6. RMS reduction of the airfoil vibration as a function of C_μ for Case 1.

Figure 1.7 and Figure 1.8 show the airfoil response and vibration reduction for all cases of C_μ, respectively. Note that the impeller driving the water tunnel oscillated at a frequency of 35 Hz. The majority of the airfoil response occurs at a frequency of approximately 9 Hz, close to the shedding frequency of the cylinder. Note that the PSD magnitude is reported using a log scale.

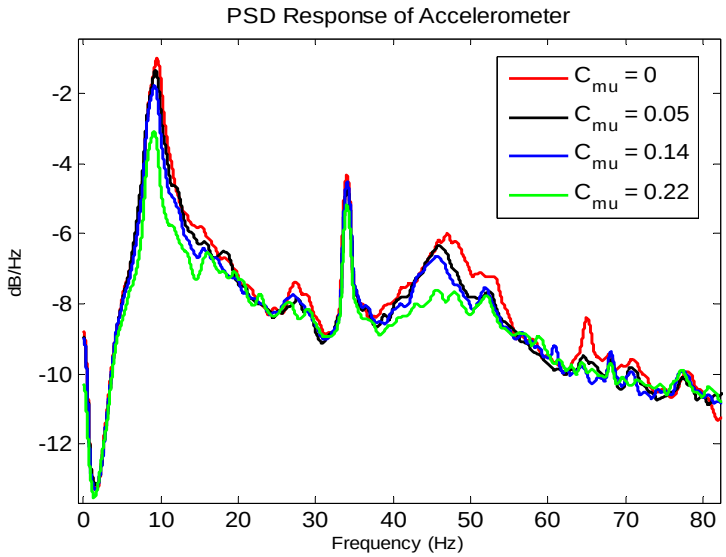

Figure 1.7. PSD magnitudes of the airfoil vibrations for Case 1.

The airfoil velocity fluctuations decrease up to a maximum of about 26 dB *re* C_μ*=0* for a C_μ=0.22. Caution must be used in interpreting these accelerometer results, as small changes in the BVI will result in large changes in the airfoil vibration levels since the interaction frequency is very close to the natural frequency of the system.

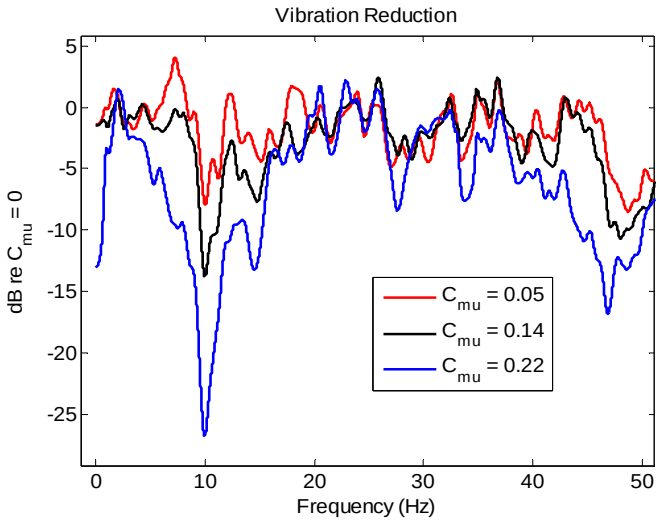

Figure 1.8. Power reductions of the airfoil vibrations for Case 1.

The airfoil vibrations are caused by the close passage of vortices over the airfoil surface, where the low pressure vortex projects an unsteady force on the surface. Figure 1.9 and Figure 1.10 compare the time averaged frequency *v* components from the DPIV data for C_μ=0 and 0.22, respectively. It is immediately apparent that for C_μ=0 the vortex maintains its character over the length of the airfoil; consider the main frequency in Figure 1.9, subplots A-F where the vortex motion is tracked by the white arrow. For C_μ=0.22, the coherency of the *v* fluctuations shifts from a very particular frequency (the Strouhal shedding frequency, or f/f_s=1) to a broader distribution, with no clear Strouhal frequency propagating down the airfoil surface. That is, the energy contained in the convecting vortices for C_μ=0 is spread over a wide range of frequencies for C_μ=0.22.

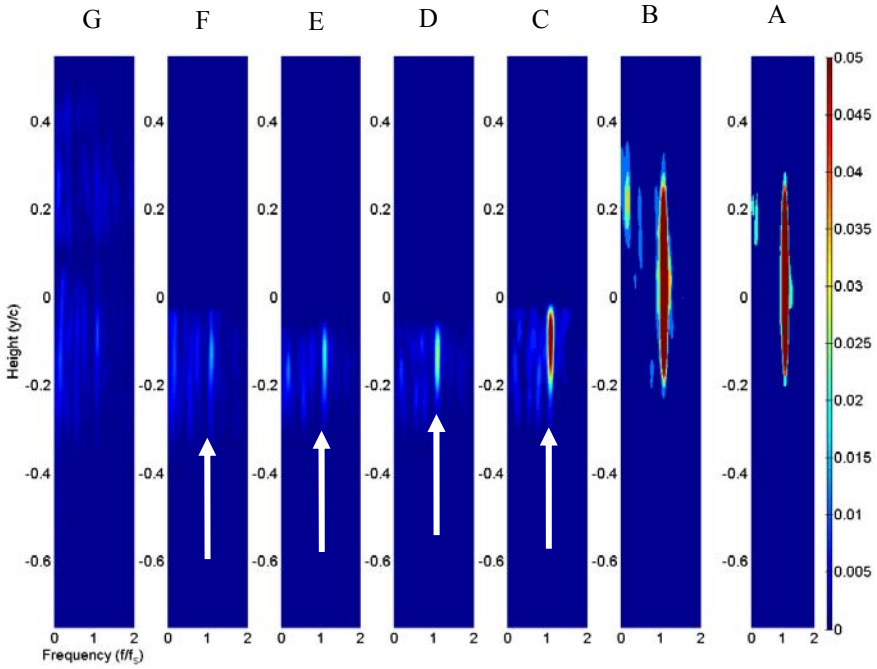

Figure 1.9. Results of PSD interrogation planes for C_μ = 0 (Case 1).

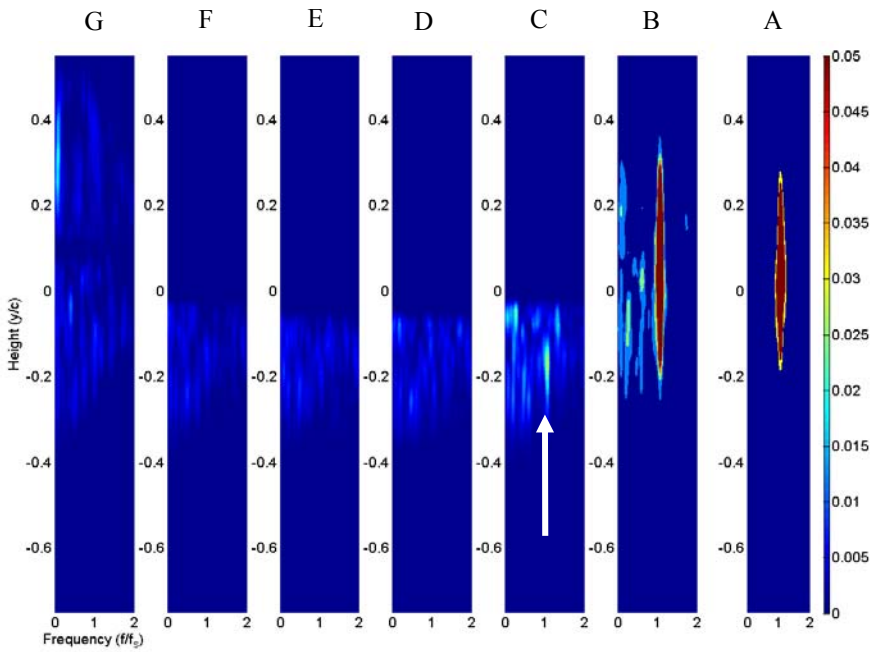

Figure 1.10. Results of PSD interrogation planes for C_μ = 0.21 (Case 1).

The DPIV results also allow us to visualize the flow patterns near the airfoil surface, and to see exactly what effect the jet has on the close passing vortices. Figure 1.11 - Figure 1.14 show instantaneous DPIV measurements of the interrogation region at 0.0625s intervals. The Figures follow one convecting vortex as it passes over the airfoil and is typical of the data seen for the case C_μ=0. The vortex stretches (Figure 1.12) as it passes under the airfoil, but for the most part maintains its character over the length of the airfoil chord.

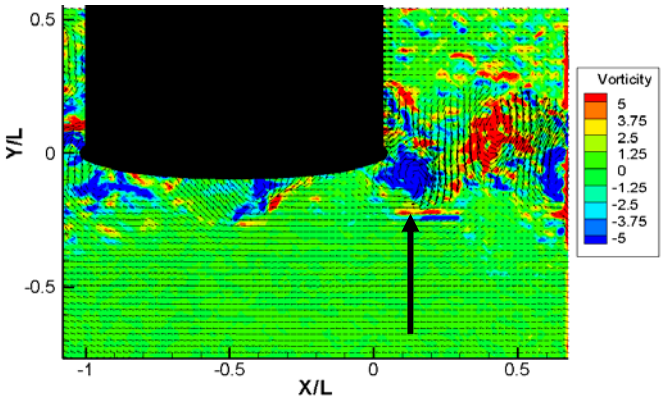

Figure 1.11. Instantaneous DPIV flow field for t_{ref} = 0s (C_μ = 0, Case 1).

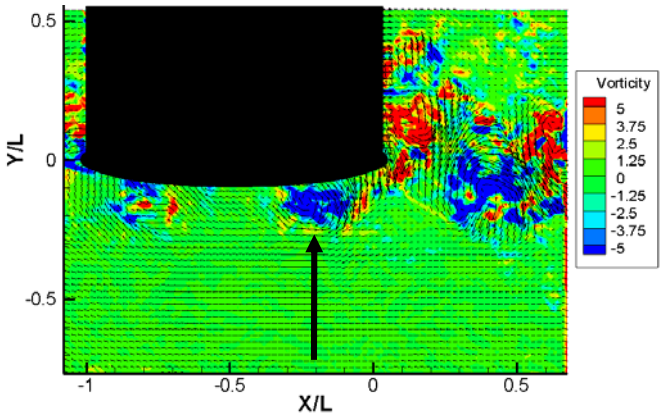

Figure 1.12. Instantaneous DPIV flow field for t_{ref} = 0.0625s (C_μ = 0, Case 1).

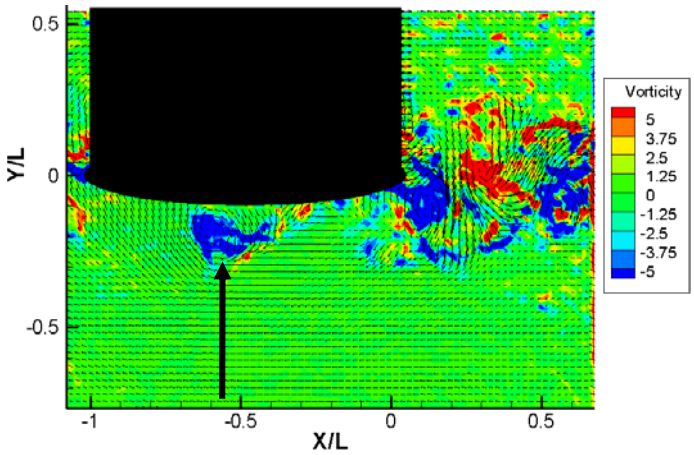

Figure 1.13. Instantaneous DPIV flow field for t_{ref} = 0.125s (C_μ = 0, Case 1).

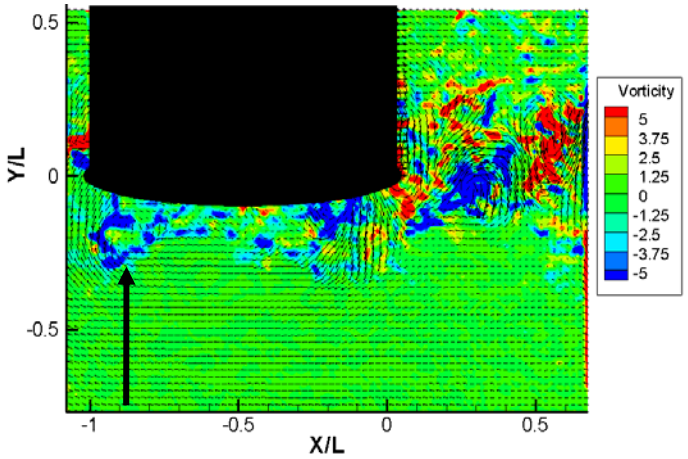

Figure 1.14. Instantaneous DPIV flow field for t_{ref} = 0.1875 (C_μ = 0, Case 1).

Figure 1.15 - Figure 1.18 show the interaction of the LEB jet with the convecting vortices and the series of events that transpire for C_μ=0.22. The images are shown at time intervals of 0.0125s. In Figure 1.15, the vortex first approaches the airfoil, and appears unaffected. By Figure 1.17, a region of high vorticity is present where the vortex should be, but examination of the flow field vectors show the absence of any coherency. It should be noted that the vorticity generated along the jet interface is of the same sign as the incident vortices for top side or bottom vortices. A comparison of Figure 1.19 and Figure 1.20 show a large increase in the total vorticity close to the airfoil blade, but there are no clear structures to act on the airfoil.

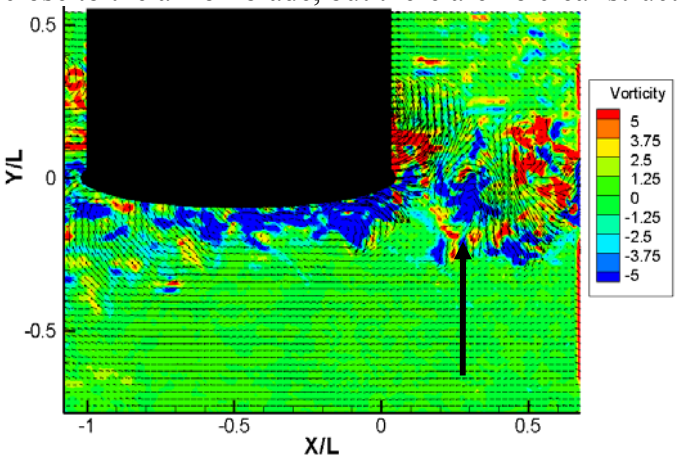

Figure 1.15. Instantaneous DPIV flow field for t_{ref} = 0s (C_μ = 0.22, Case 1).

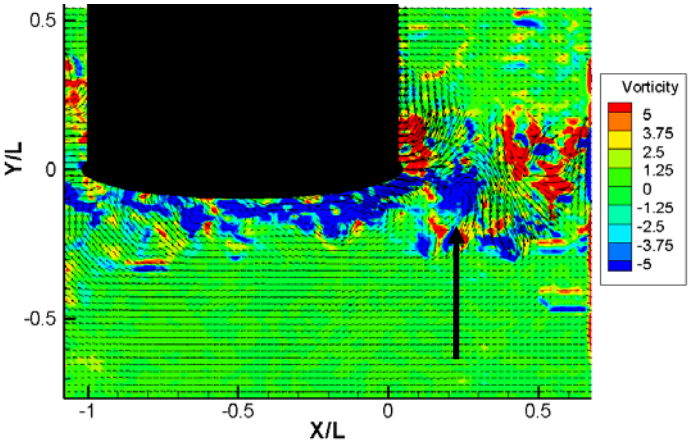

Figure 1.16. Instantaneous DPIV flow field for t_{ref} = 0.0125s (C_μ = 0.22, Case 1).

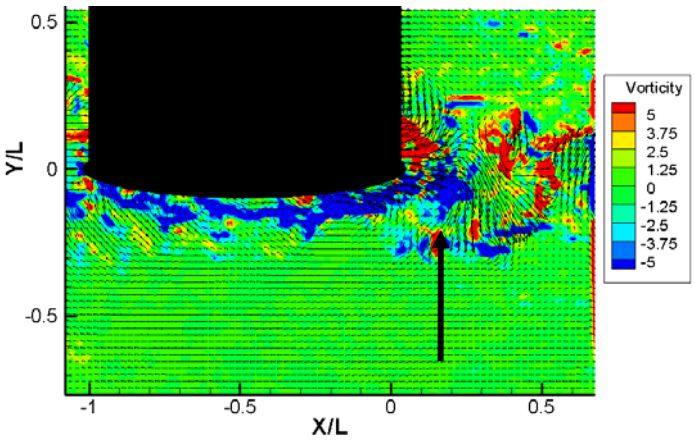

Figure 1.17. Instantaneous DPIV flow field for t_{ref} = 0.025s (C_μ = 0.22, Case 1).

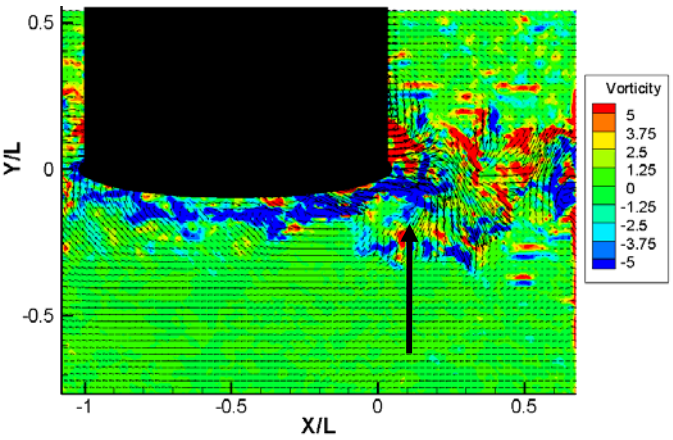

Figure 1.18. Instantaneous DPIV flow field for t_{ref} = 0.0375s (C_μ = 0.22, Case 1).

The vorticity in the region near the airfoil for C_μ=0.22 is markedly increased over that in the C_μ=0 case; this may be seen by comparing Figure 1.19 and Figure 1.20, which show the time averaged vorticity field for C_μ=0 and C_μ=0.22, respectively. This increase in vorticity for the flow field is due to the fact that the vorticity generated by the jet itself is the same sign as that of the convecting vortices. Also, the jet acts to break up the incident vortex structure into a highly irregular and turbulent flow. Although global vorticity is increased, the coherency of any forcing structures is shattered due to its interaction with the jet and thus there is no clear structure to force the airfoil vibration.

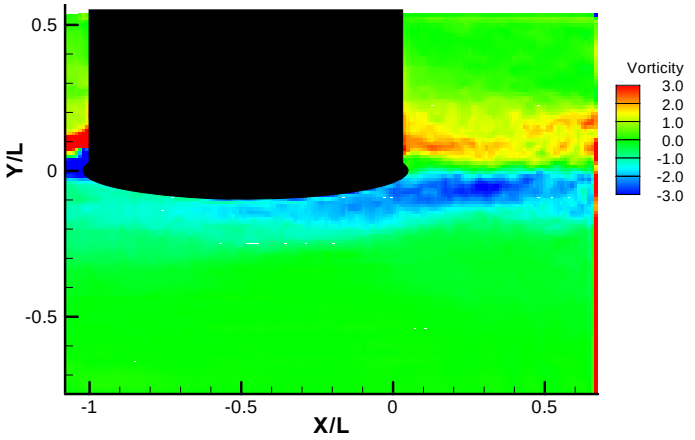

Figure 1.19. Time averaged mean vorticity field for C_μ=0 (Case 1).

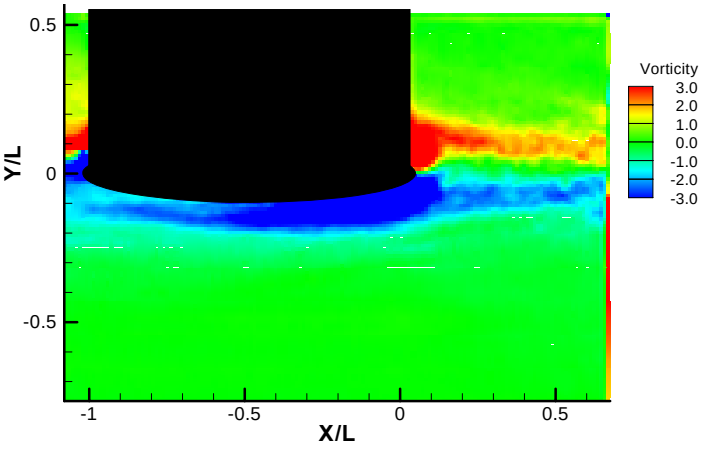

Figure 1.20. Time averaged mean vorticity field for C_μ=0.22 (Case 1).

1.3.2 Results – Case 2

In this case, the circular cylinder diameter is larger than the airfoil thickness (0.75" diameter) with a shedding frequency of 5.8 Hz. The LEB is effective at reducing airfoil vibrations as shown by Figure 1.21, which shows the percentage in the RMS velocity fluctuations of the airfoil as a function of C_μ. At a C_μ=0.22, the velocity fluctuations are reduced by about 40%. This reduction is less than that for the smaller circular cylinder shown in Case 1 by about 20% at the maximum C_μ.

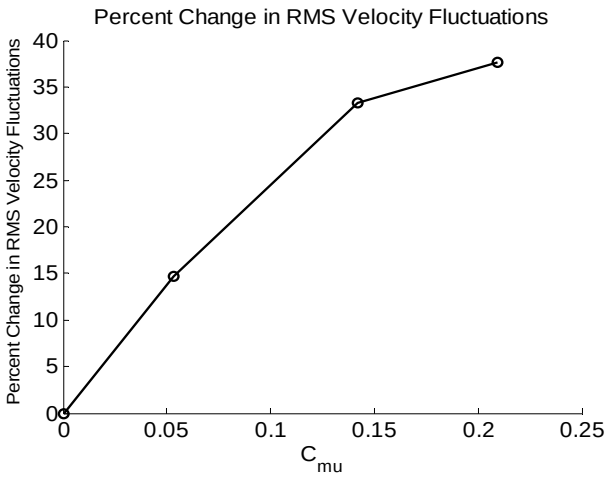

Figure 1.21. Reduction in RMS level of airfoil vibration as a function of C_μ for Case 2.

The PSD magnitude of the airfoil velocity response is shown in Figure 1.22. The major frequency component is located at approximately 6 Hz, which is the predicted shedding frequency of the circular cylinder. A smaller peak is also at approximately 12 Hz, which is the natural frequency of the system. The airfoil velocity fluctuations are shown in Figure 1.23 and decrease up to a maximum of about 12 dB *re* $C_\mu=0$ for a C_μ=0.21 at the excitation frequency. There is a broad reduction in vibration frequencies between the excitation frequency and the natural frequency of the system.

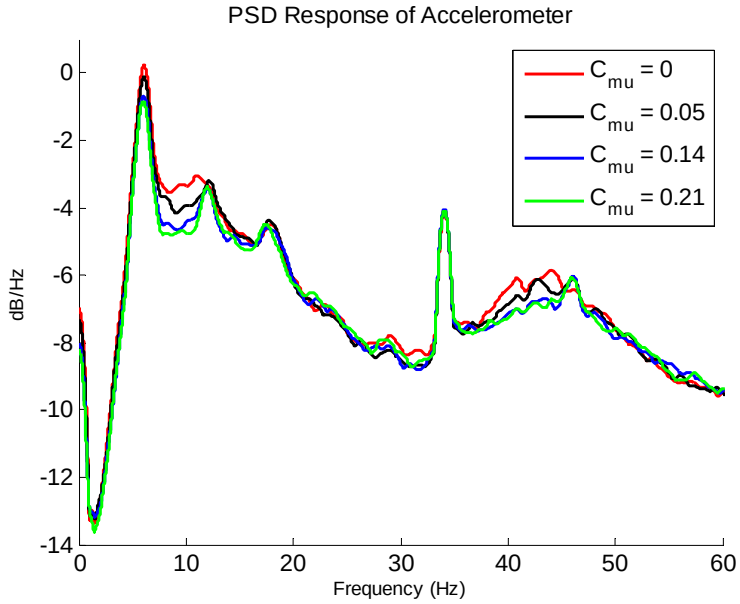

Figure 1.22. PSD magnitudes of the airfoil vibrations for Case 2.

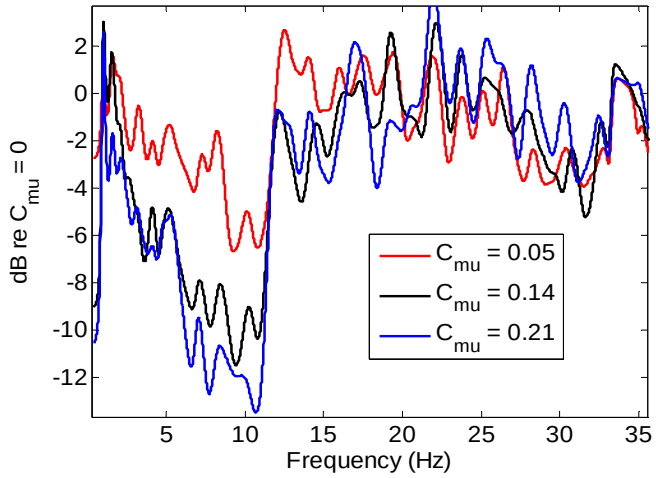

Figure 1.23. Power reductions of the airfoil vibrations for Case 2.

Thus, the airfoil motion is being caused by the close passage of the coherent structures in the cylinder wake. Figure 1.24 and Figure 1.25 compare the time averaged frequency (ν) components from the DPIV data for C_μ=0 and 0.21, respectively. It is immediately apparent that for C_μ=0 the vortex maintains its character over the length of the airfoil and persists into the airfoil wake. For C_μ=0.21, the strength of the circular cylinder shedding frequency decreases and splits into several other frequencies. Close comparison of Figure 1.24 and Figure 1.25 show that the flow field frequencies which act on the airfoil do not appear close to the airfoil surface for C_μ=0.21. That is, the unsteadiness of the flow field seen for C_μ=0 approaches the surface of the airfoil, while for C_μ=0.21 any flow field frequencies are displaced downwards, away from the airfoil surface. Thus, the miss distance is increased. Figure 1.26 - Figure 1.29 are instantaneous DPIV measurements of the system and follow one convecting vortex as it passes over the airfoil and is typical of the data seen for the case C_μ=0. The time interval between frames is 0.0375s. Note that the vortex maintains its character over the length of the airfoil chord.

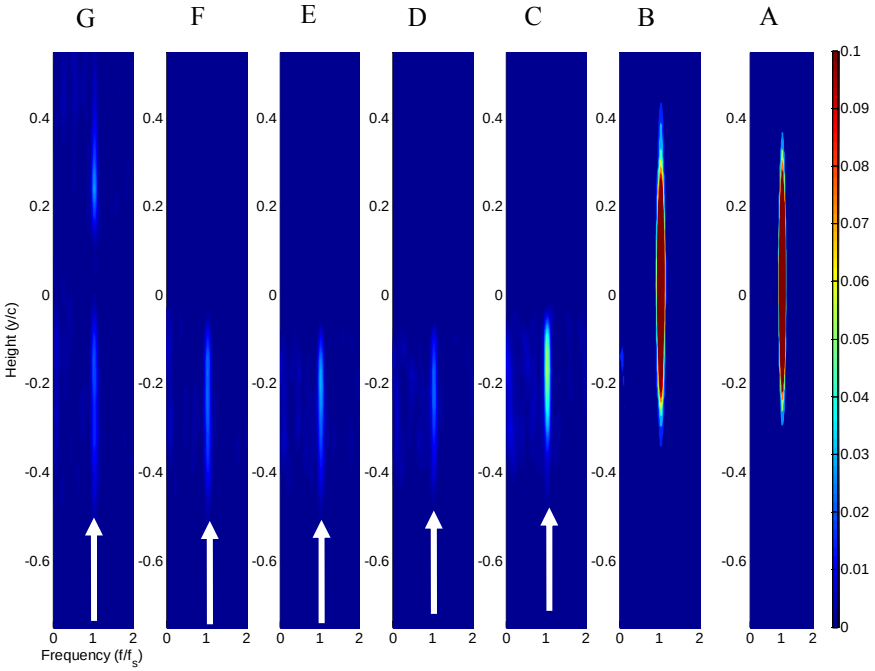

Figure 1.24. Results of PSD interrogation planes for C_μ=0 (Case 2).

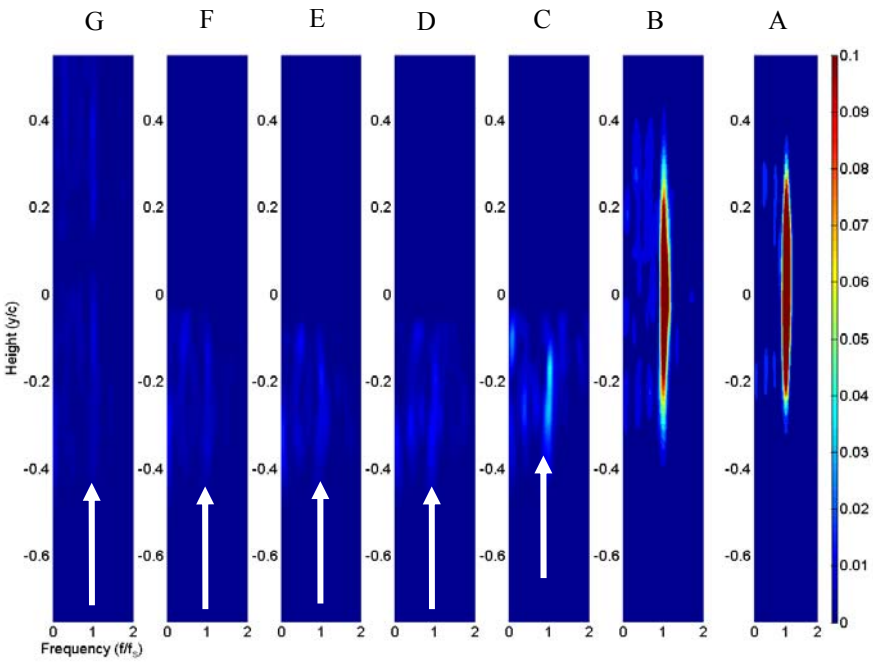

Figure 1.25. Results of PSD interrogation planes for C_μ=0.21 (Case 2).

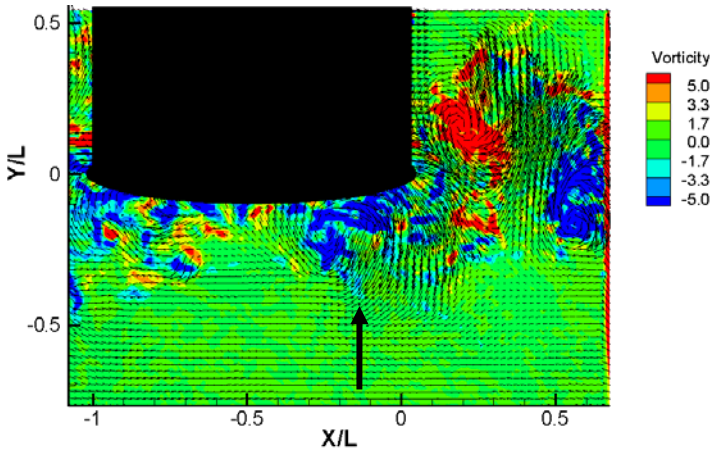

Figure 1.26. Instantaneous DPIV flow field for t_{ref} = 0s (C_μ = 0, Case 2).

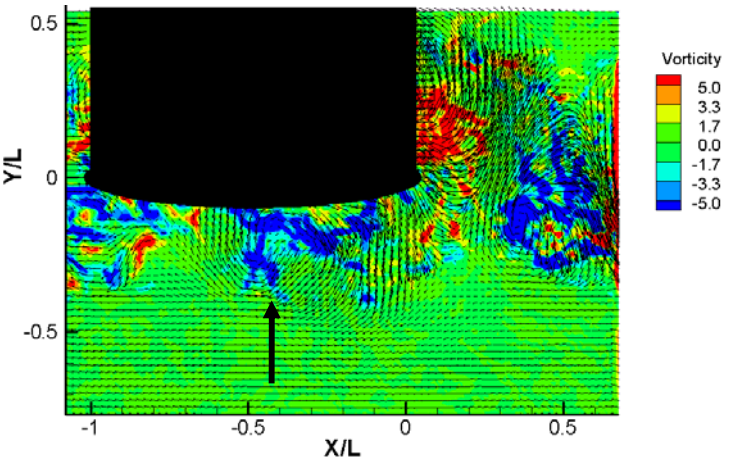

Figure 1.27. Instantaneous DPIV flow field for t_{ref} = 0.0375s (C_μ = 0, Case 2).

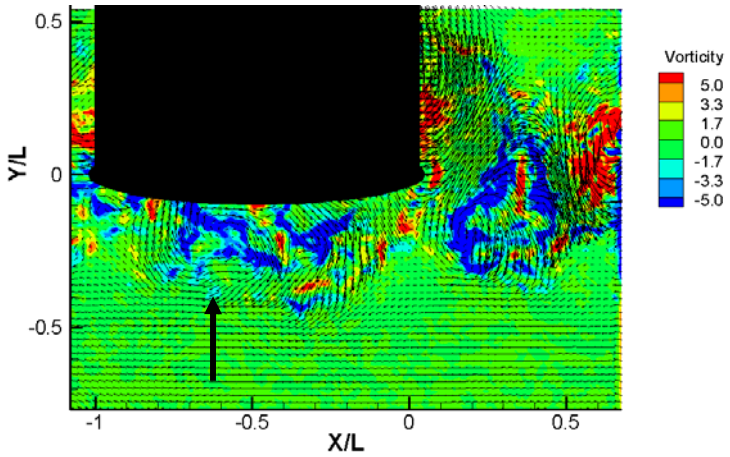

Figure 1.28. Instantaneous DPIV flow field for t_{ref} = 0.075s (C_μ = 0, Case 2).

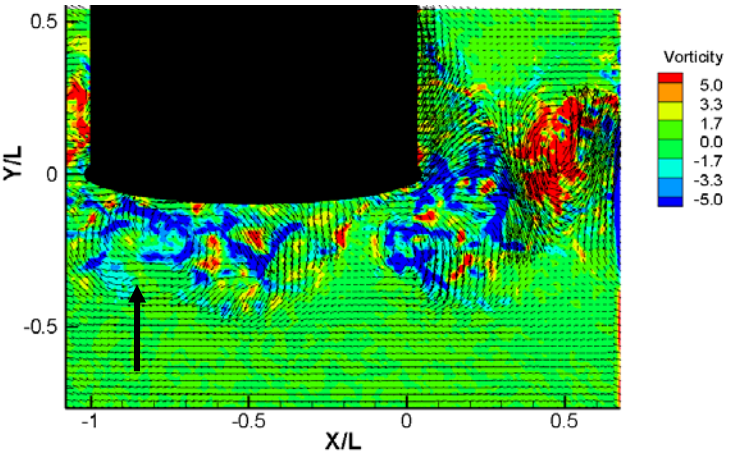

Figure 1.29. Instantaneous DPIV flow field for t_{ref} = 0.1125s (C_μ = 0, Case 2).

Figure 1.30 - Figure 1.33 show the interaction of the LEB jet with the convecting vortices for C_μ=0.21. A completely coherent vortex is seen in Figure 1.30. The vortex appears to break up and diffuse as it approaches the leading edge of the airfoil, seen in Figure 1.31. By Figure 1.32, the vortex has disintegrated.

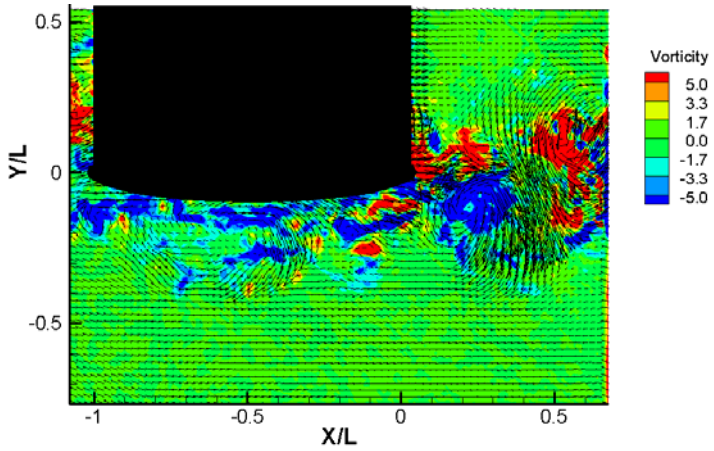

Figure 1.30. Instantaneous DPIV flow field for t_{ref} = 0s (C_μ = 0.21, Case 2).

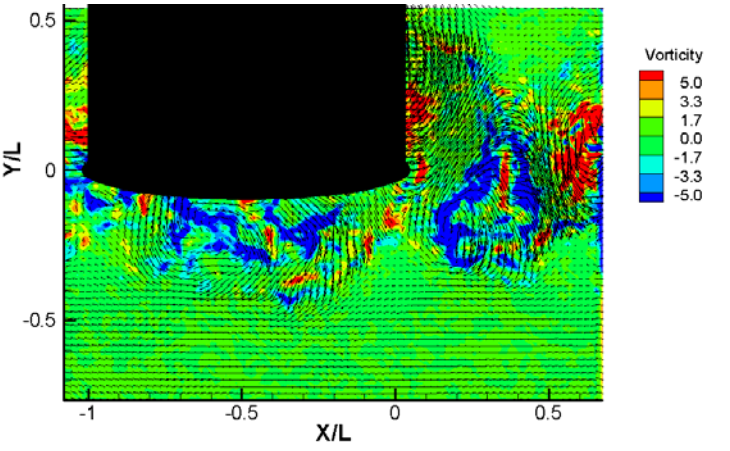

Figure 1.32. Instantaneous DPIV flow field for t_{ref} = 0.075s (C_μ = 0.21, Case 2).

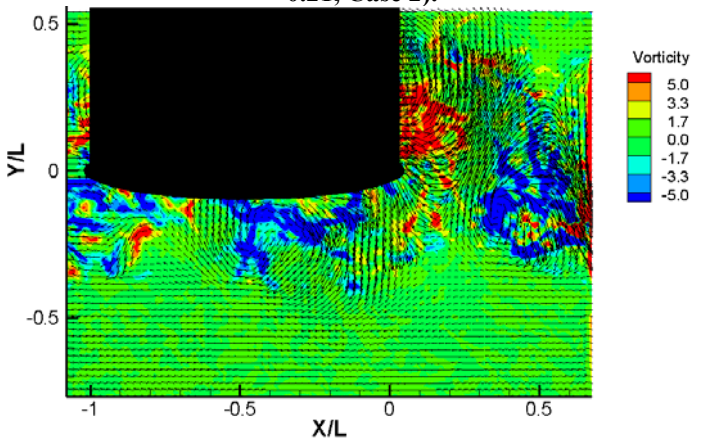

Figure 1.31. Instantaneous DPIV flow field for t_{ref} = 0.0375s (C_μ = 0.21, Case 2).

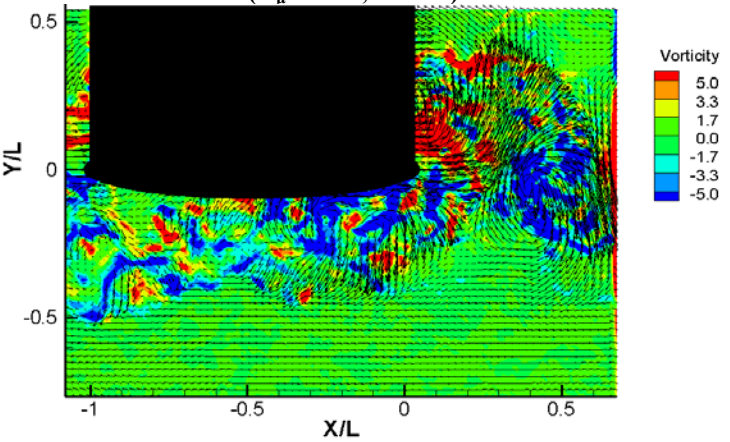

Figure 1.33. Instanteous DPIV flow field for t_{ref} = 0.1125 (C_μ = 0.21, Case 2).

1.3.3 Results – Case 3

In this case, the wake generator was almost twice the size of the airfoil maximum thickness, and the shedding frequency was 3.5 Hz. Interestingly, the LEB jet has the opposite effect when compared to Cases 1 and 2, as shown in Figure 1.34. The airfoil vibrations decrease more for C_μ=0.05 than for C_μ=0.21. However, the RMS velocity fluctuations experienced by the airfoil are larger for the blowing cases than for no blowing.

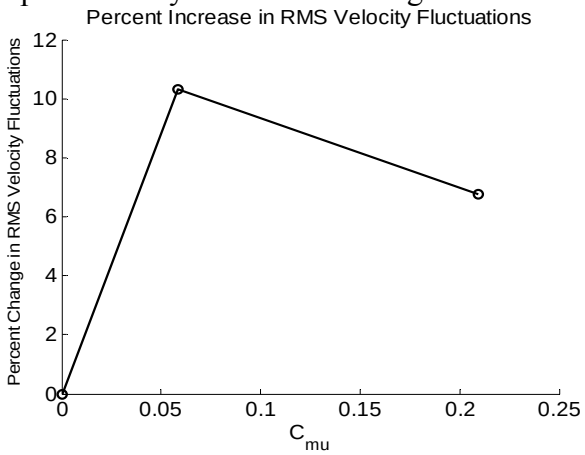

Figure 1.34. Reduction in RMS level of airfoil vibration as a function of C_μ for Case 3.

Figure 1.35 and Figure 1.36 show the airfoil response and vibration change for all cases of C_μ, respectively. The majority of the airfoil response occurs at a frequency of approximately 3.5 Hz, which is the shedding frequency of the cylinder. There is another frequency component which grows in power but decreases in frequency as a function of the blowing rate between 6.5-7 Hz.

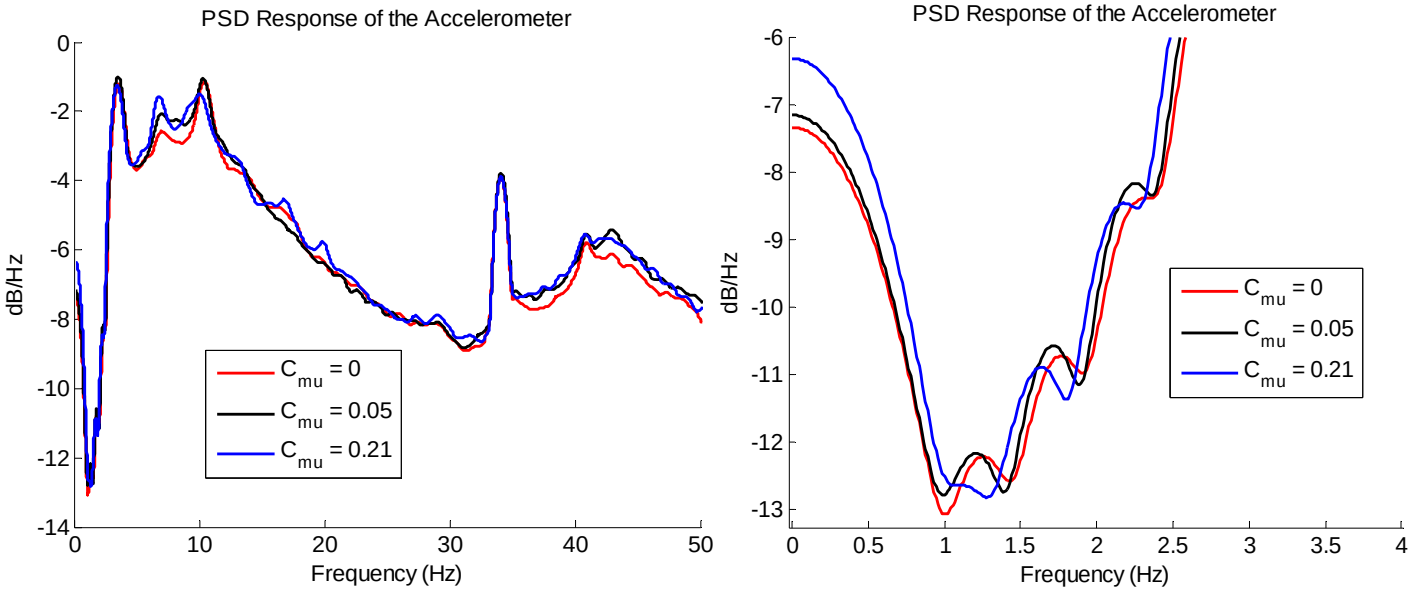

Figure 1.35. PSD of airfoil vibrations as a function of C_μ for Case 3.

Figure 1.36 shows the change in power of the velocity fluctuations as a function of the blowing rate. Decreases on the order of 5 dB *re* C_μ*=0* are seen for several frequencies, namely 1.2, 1.8, 4, and 10.5 Hz. Increases in power on the order of 10 dB *re* C_μ*=0* are seen for frequencies at 1.5, 2, 2.5, and 6.5 Hz. The

detrimental effect of increasing the power seen at these frequencies is shown to be a function of C_μ, with the largest C_μ having the greatest power additions.

Figure 1.37 - Figure 1.39 show the PSD magnitude of the airfoil velocity response. In Figure 1.38, subplots A-G, a vortex is clearly seen which propagates over the entire airfoil. A comparison of Figure 1.38, subplot C, with Figure 1.39, subplot C, shows that the power of the vortex located just aft of the leading edge increases in power for C_μ=0.05. Downstream of this point, the power in the vortices decreases when compared to the C_μ=0 case. The asymmetric LEB jet manifests itself in Figure 1.38, subplot G, where the propagation of the vortices into the wake of the airfoil shows stronger power for the topside of the airfoil (LEB jet is located only on the bottom side). For the maximum C_μ (Figure 1.39), the vortex follows a path further from the airfoil surface with less power than the previous two blowing rates, and the mean path of the vortex is displaced further from the airfoil surface. It appears in Figure 1.39, subplots E and F, that the vortices have two mean paths. This is interesting because the vortex in subplot D occurs, on the average, in one location. In subplot E, the two vortex paths are located at *y/c*=-0.25 and -0.41 and in subplot F, at *y/c*=-0.25 and -0.5. Note that the power of the vortex seen in Figure 1.37 - Figure 1.39 in subplot C does not change markedly as C_μ is increased, which indicates that the LEB jet is not affecting the structure of the vortex (i.e. the jet is not causing the vortex to burst or disintegrate), but rather its path.

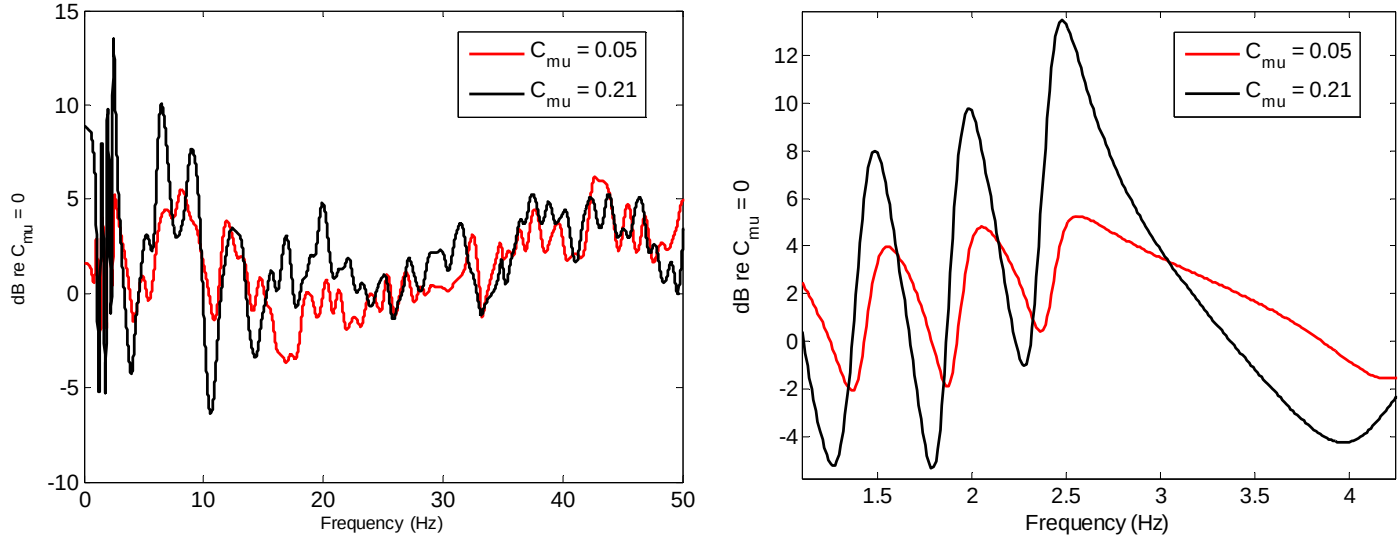

Figure 1.36. Change in power of airfoil vibrations as a function of C_μ for Case 3.

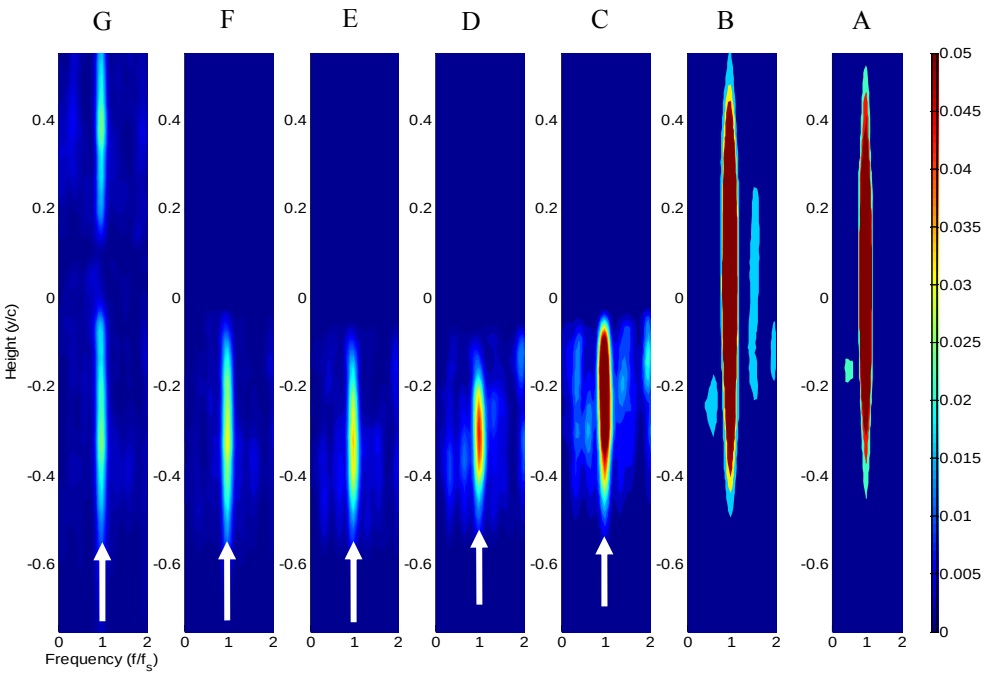

Figure 1.37. Results of PSD interrogation planes for C_μ=0 (Case 3).

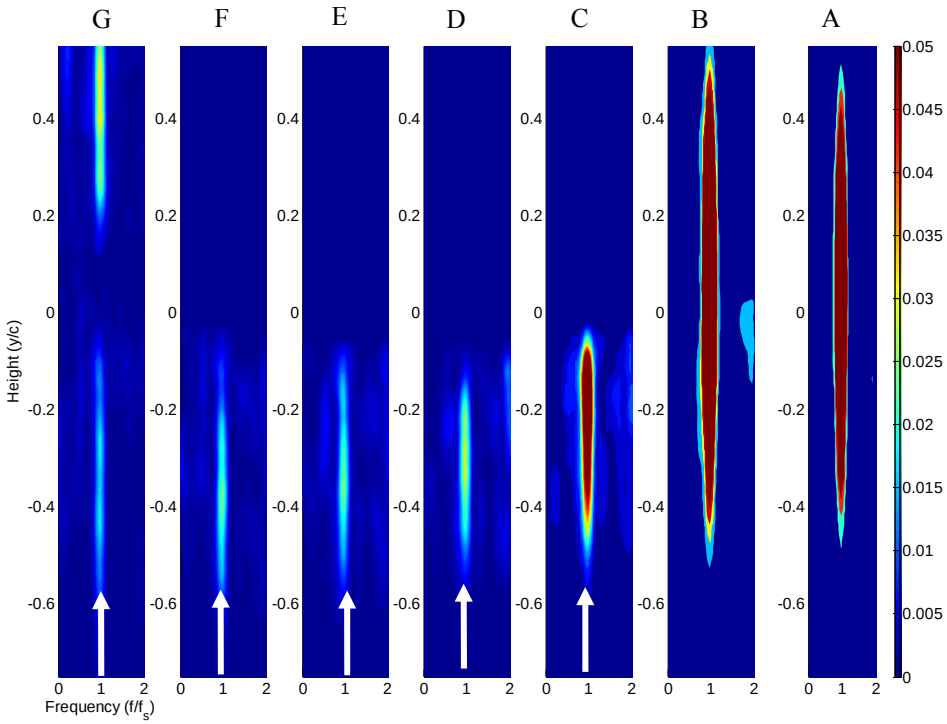

Figure 1.38. Results of PSD interrogation planes for C_μ=0.05 (Case 3).

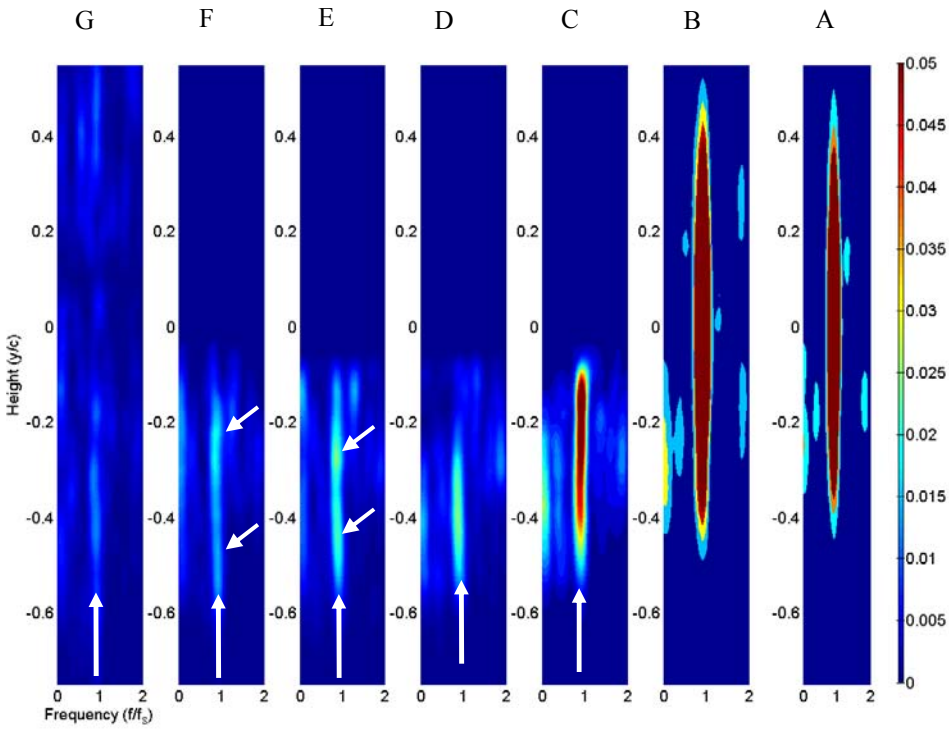

Figure 1.39. Results of PSD interrogation planes for C_μ=0.21 (Case 3).

Figure 1.40 - Figure 1.43 show instantaneous DPIV measurements of the interrogation region at 0.075s intervals. The Figures follow one convecting vortex as it passes over the airfoil and is typical of the data seen for the case C_μ=0. The vortex stretches into an ellipse with the major axis parallel to the mean flow direction as it passes over the surface of the airfoil, but maintains its coherency and ability to transmit an unsteady loading onto the airfoil surface. Note that the vortex is almost bisected by the leading edge of the airfoil.

Figure 1.44 - Figure 1.47 show instantaneous DPIV measurements of the flow field for C_μ=0.05. In this case, the LEB jet acts to push the mean path of the vortex approaching from the bottom side of the airfoil off of the airfoil surface, so that the incident vortex is not split by the sharp leading edge. Thus, the vortex propagates close to the airfoil surface at nearly its full strength. However, the asymmetry in the LEB jet at this low blowing rate causes a vortex approaching from the top side of the airfoil to not be displaced upwards. This would prevent a topside vortex from inducing a separation on the bottom side of the airfoil as it hits the sharp leading edge. Instead, the topside vortex does induce a flow separation leading to an impulsive force on the airfoil. This is possibly the source of the 1.5 Hz signal seen in Figure 1.36, since a topside vortex will impact the airfoil at half the frequency of vortex generation (i.e. every other vortex).

Figure 1.48 - Figure 1.51 show instantaneous DPIV measurements of the flow field for C_μ=0.21. Here the jet acts to displace a bottom side vortex from the airfoil surface. The images are shown at 0.075s intervals. Again, the asymmetry in the LEB jet, and its inability to influence the upper vortex from impact the sharp leading edge, is readily apparent. In fact, the levels of vibration at the 6.5 Hz level increase, because the LEB jet tends to follow the path of least resistance in the flow. When a bottom side vortex induces the local fluid to move upwards, the jet tends to point upwards, and the low pressure jet will act to draw the vortex towards itself. When a top side vortex induces motion towards the bottom side of the airfoil, the jet follows this path. Thus the jet will guide a topside vortex onto the axis of the airfoil, where its impact will impart the most separation and strongest forcing function. Bottom side vortices do not induce separation as the LEB jet produces a buffer zone around the sharp leading edge. Thus separation only occurs due to top side vortices.

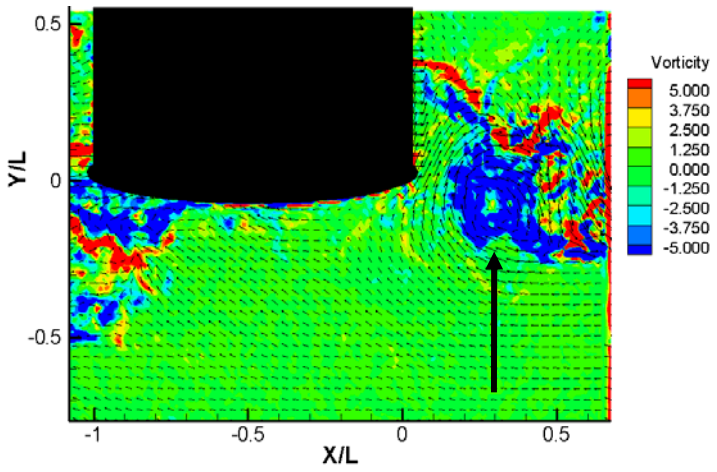

Figure 1.40. Flow field for t_{ref}=0s (C_μ = 0, Case 3).

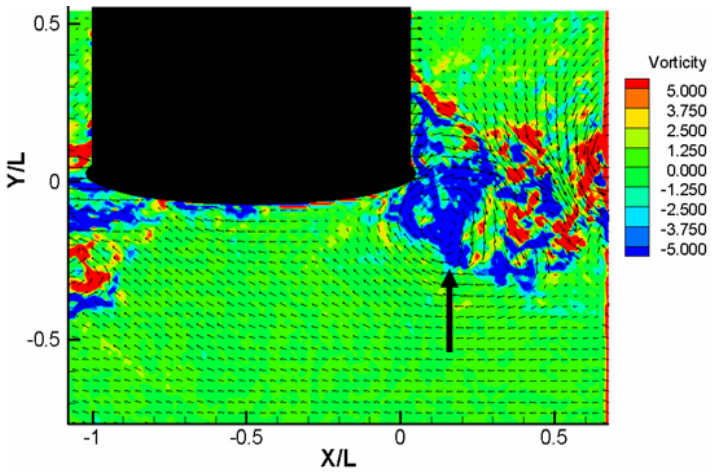

Figure 1.41. Flow field for t_{ref}=0.075s (C_μ = 0, Case 3).

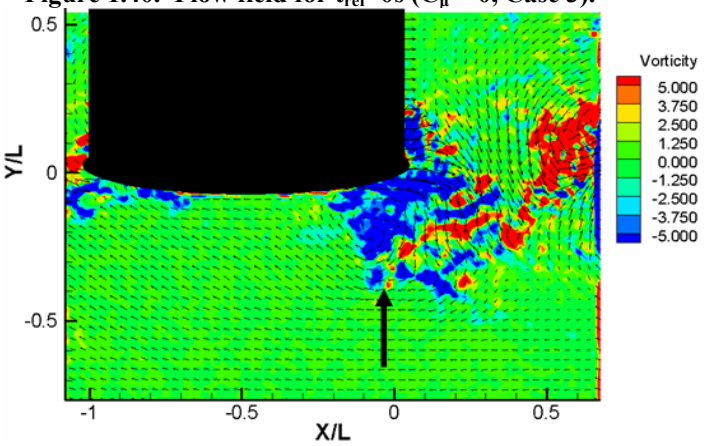

Figure 1.42. Flow field for t_{ref}=0.15s (C_μ = 0, Case 3).

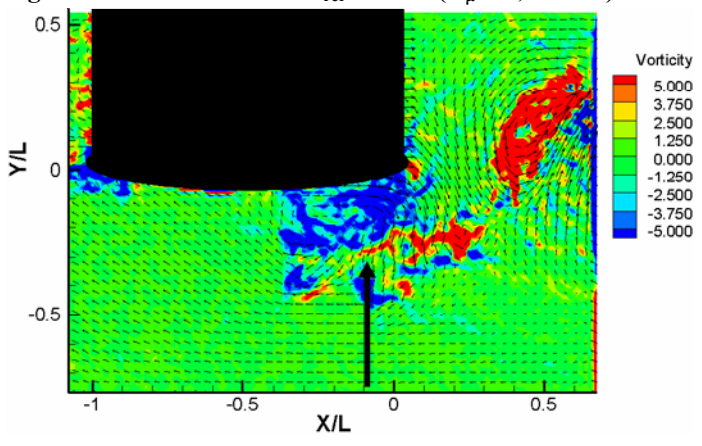

Figure 1.43. Flow field for t_{ref}=0.225s (C_μ = 0, Case 3).

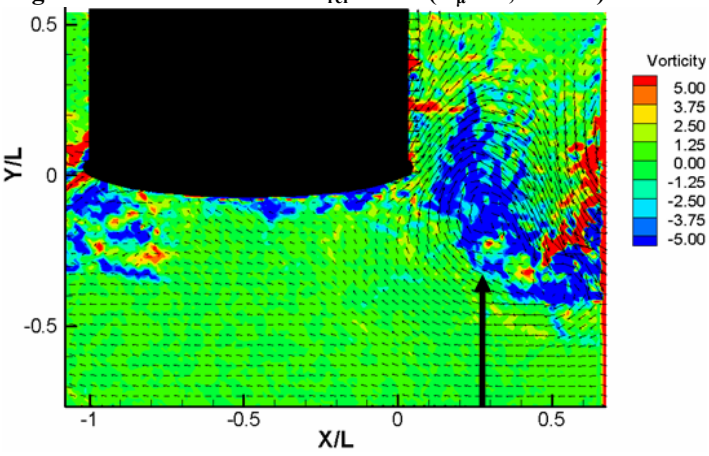

Figure 1.44. Flow field for t_{ref}=0s (C_μ = 0.05, Case 3).

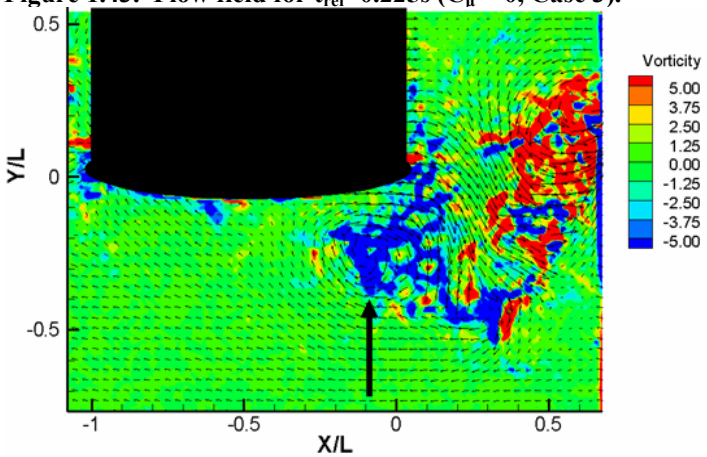

Figure 1.45. Flow field for t_{ref}=0.075s (C_μ = 0.05, Case 3).

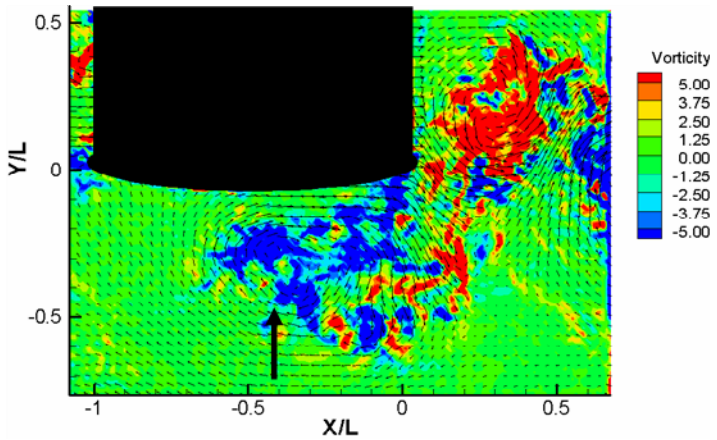

Figure 1.46. Flow field for t_{ref}=0.15s (C_μ = 0.05, Case 3).

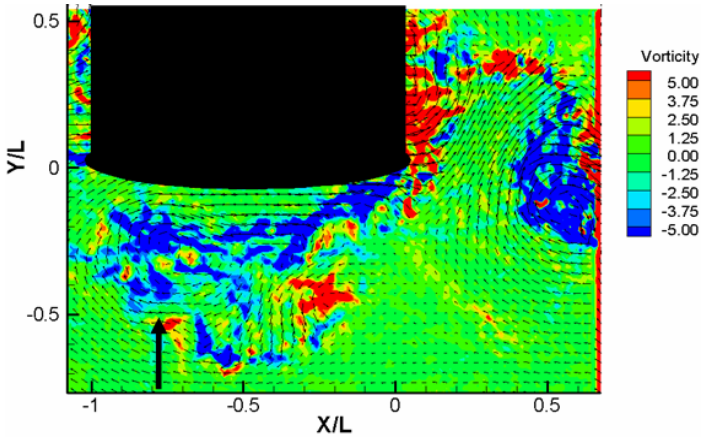

Figure 1.47. Flow field for t_{ref}=0.225s (C_μ = 0.05, Case 3).

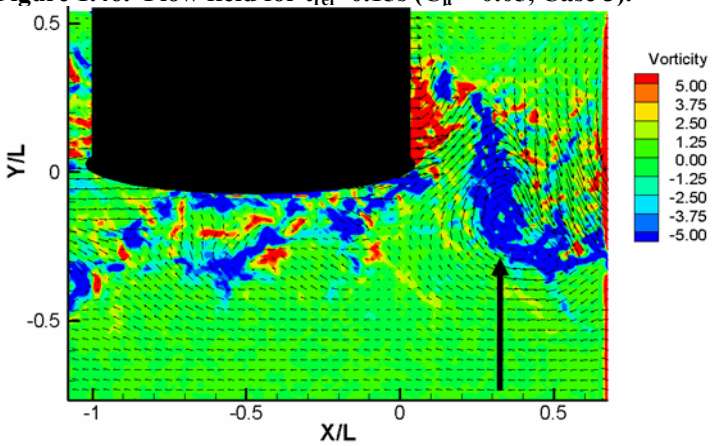

Figure 1.48. Flow field for t_{ref}=0s (C_μ = 0.21, Case 3).

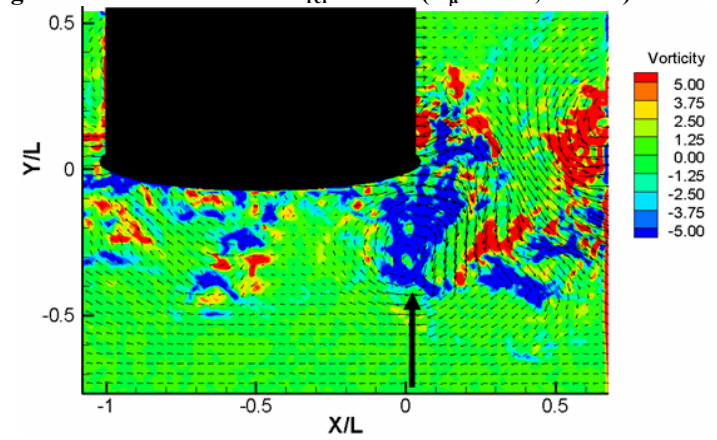

Figure 1.49. Flow field for tref=0.075s (C_μ = 0.21, Case 3).

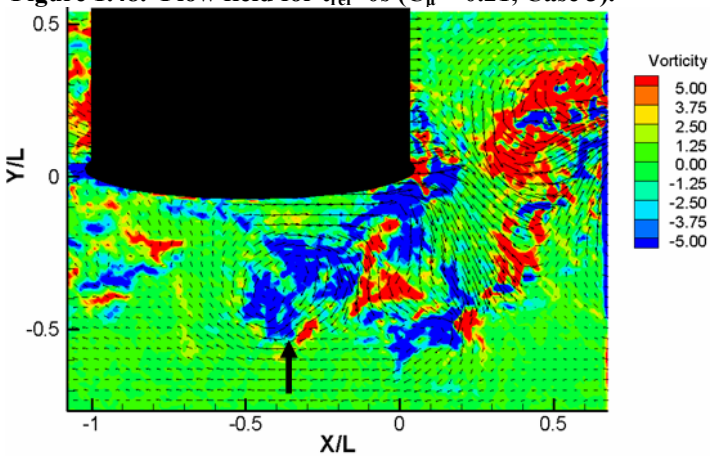

Figure 1.50. Flow field for t_{ref}=0.15s (C_μ = 0.21, Case 3).

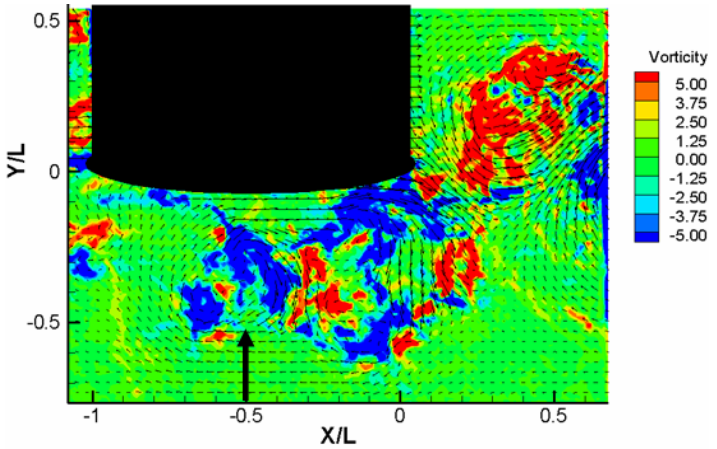

Figure 1.51. Flow field for t_{ref}=0.225s (C_μ = 0.21, Case 3).

1.3.4 Results – Case 4

In this case, the wake generator was three times the airfoil maximum thickness, and the shedding frequency of the circular cylinder was 2.2 Hz. The frequency response of the airfoil and the power increase are shown in Figure 1.52 and Figure 1.53. The increase in the RMS velocity fluctuations was 39% at C_μ=0.21, which was the only blowing strength studied. Interestingly, the airfoil vibration frequency at the shedding frequency of the circular cylinder (2.2 Hz) was increased by 14 dB *re* C_μ=*0*. The largest frequency increase is seen at 6.2 Hz, with a power increase of 16 dB *re* C_μ=*0*.

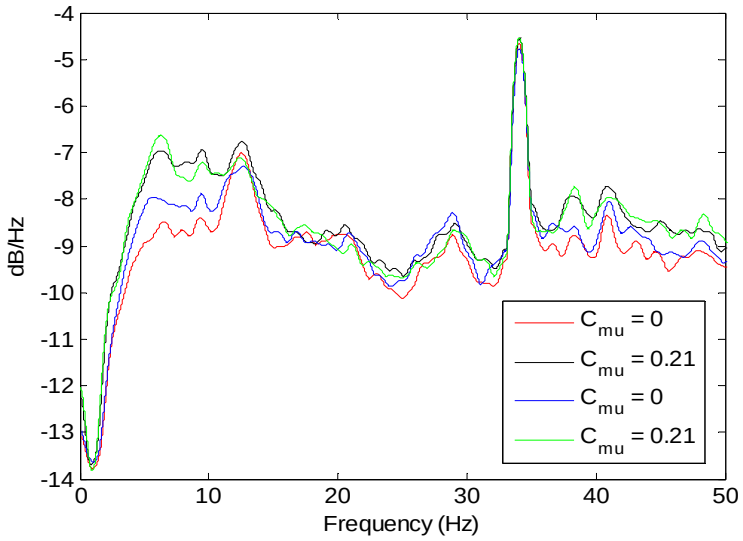

Figure 1.52. PSD magnitudes of the airfoil vibrations.

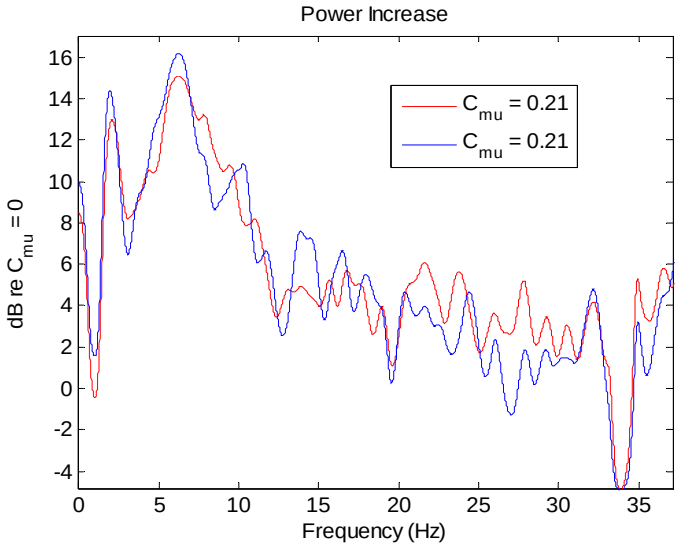

Figure 1.53. Spectral energy change with LEB.

The detrimental effect of the LEB was analyzed using the DPIV data gathered and was shown to increase the unsteady action of the wake via organization. Figure 1.54 and Figure 1.55 show the spectral components of the vertical velocity fluctuations in the wake of the circular cylinder for the two blowing cases. For C_μ=0, there were no dominant flow structures; the wake energy was spread among several frequencies. None of the frequencies seen for this case were at the Strouhal shedding frequency.

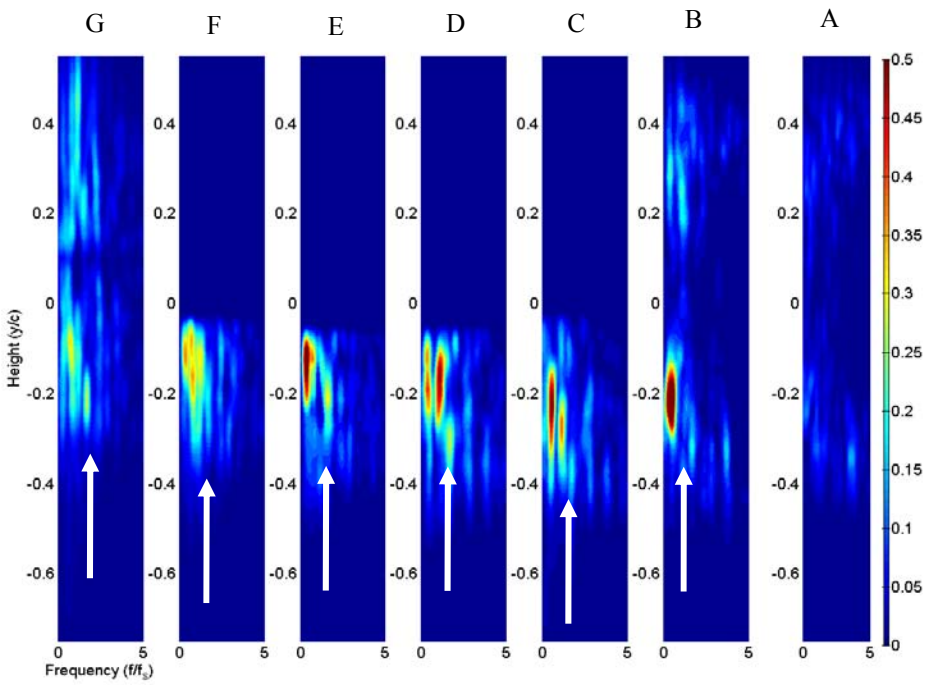

Figure 1.54. Flow field spectral components for C_μ = 0.

For C_μ=0.21, dominant spectral characteristics present themselves. In this case, all of the dominant spectral energy was centered on the predicted Strouhal shedding frequency. Note the degree of both power and size of the regions influenced by the vertical velocity fluctuations in both blowing cases. For C_μ=0.21, the wake is now strongly organized and able to load the airfoil; the cause of the 14 dB *re* C_μ*=0* power increase seen in Figure 1.53 at 2.2 Hz is now readily apparent.

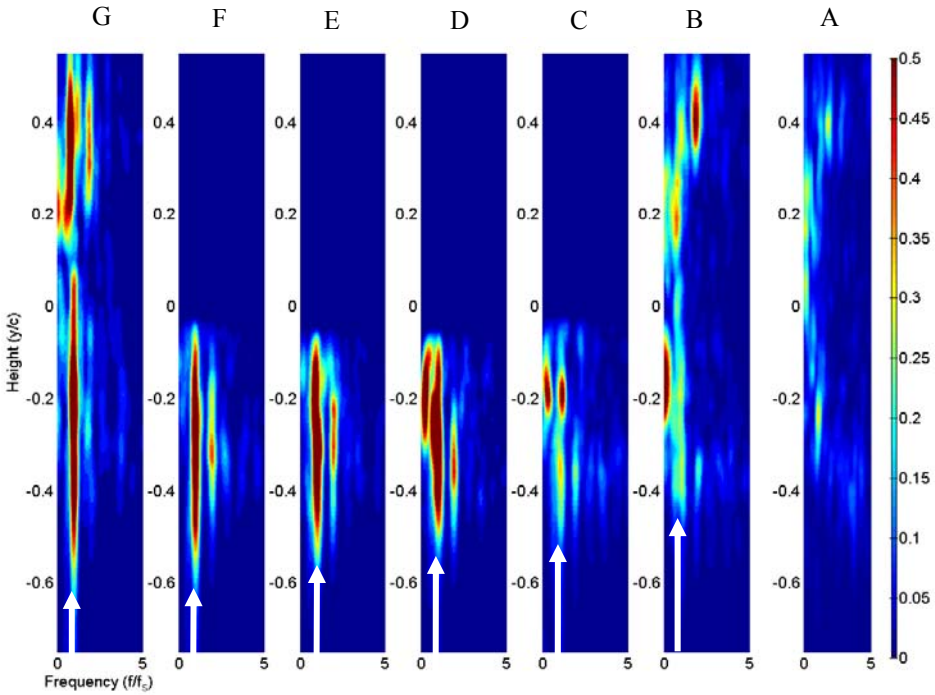

Figure 1.55. Flow field spectral components for C_μ = 0.21.

Analysis of the qualitative flow visualization proves insightful. A comparison of Figure 1.56 and Figure 1.57, which are typical of the images captures for the C_μ=0 and C_μ=0.21 cases, respectively, show an interesting phenomenon. Because the airfoil is so close to the large cylinder, it impedes the development of the vortex street, almost acting as a splitter plate. Instead of a highly coherent vortex street, a highly turbulent and undeveloped wake propagates from the circular cylinder with a strong recirculation zone directly in the wake of the cylinder, which acts to draw fluid from the airfoil leading edge upstream. For C_μ=0.21, the jet penetrates into this dead-water region and appears to "spin up" the vortices along the region of high shear between the dead-water region directly in the wake of the circular cylinder and the undisturbed flow, outside of the zone of influence of the circular cylinder wake. Five clear vortices are seen and marked with red arrows when the LEB is on. The vortices are symmetric on the trailing edge of the circular cylinder, and become skewed (with respect to the top and bottom vortices on either side of the airfoil surface). This could, perhaps be caused by the asymmetric LEB slot, which acts to inject fluid with greater velocity (energy) on the bottom side of the airfoil.

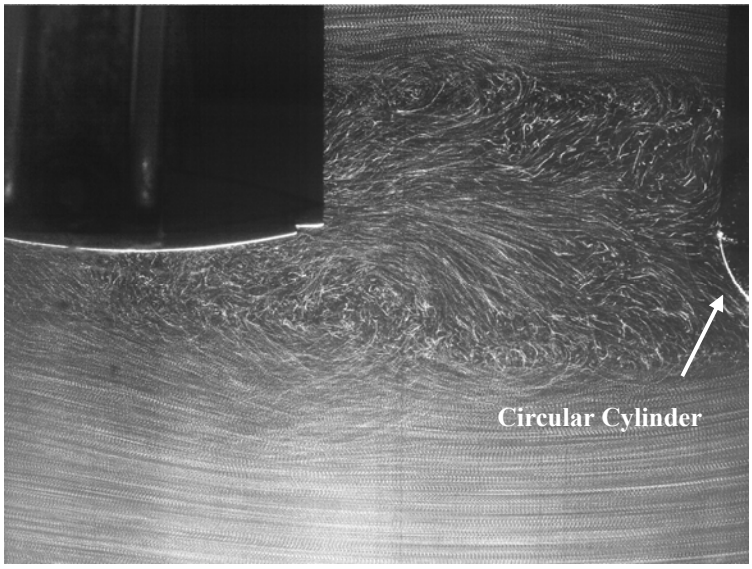

Figure 1.56. Flow visualization for Case 5, no blowing.

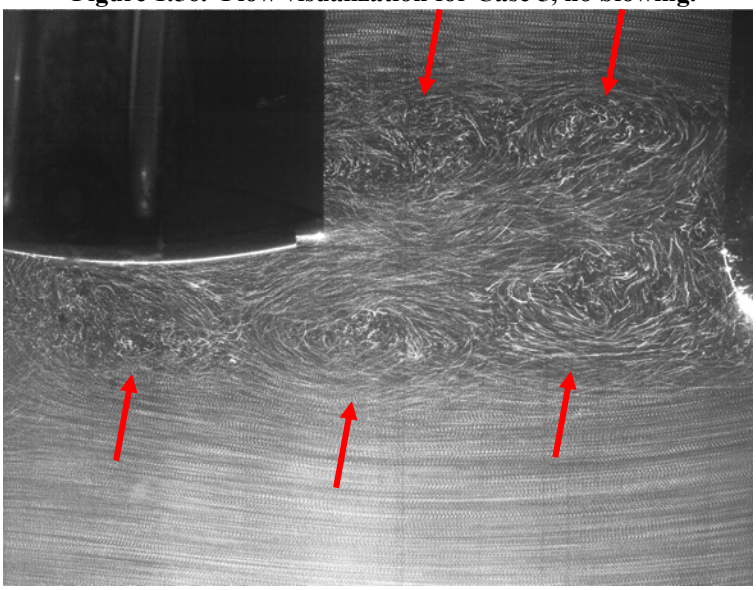

Figure 1.57. Flow visualization for Case 5, max blowing.

Figure 1.58 and Figure 1.59 present the mean vorticity field for the region of interrogation with C_μ=0 and C_μ=0.21, respectively. Note how the vorticity field for the maximum blowing case is pushed off of the airfoil surface, so that the convecting vortices move parallel to the blade surface. For no blowing, the circular cylinder wake is closing directly onto the airfoil surface. In this case, the airfoil is acting like a splitter plate, and prevents the formation of the vortex street as the airfoil is inside the mean closure point of the circular cylinder wake. The addition of the LEB jet vorticity to the total field is apparently weighted towards the lower side of the airfoil, where the blowing slot is. The spinning up of a shear layer by introducing a strong jet, or "vortex feeding," plays a primary role in the BVI for structures in close proximity to one another if LEB flow control is to be used to minimize the degree of interaction.

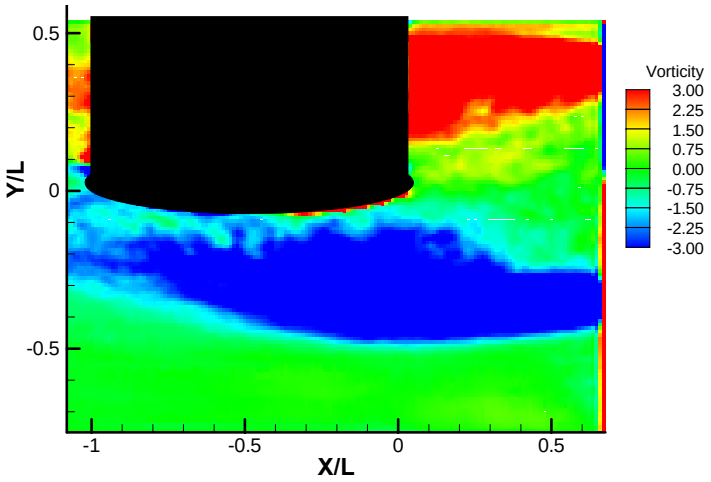

Figure 1.58. Mean vorticity field for no blowing.

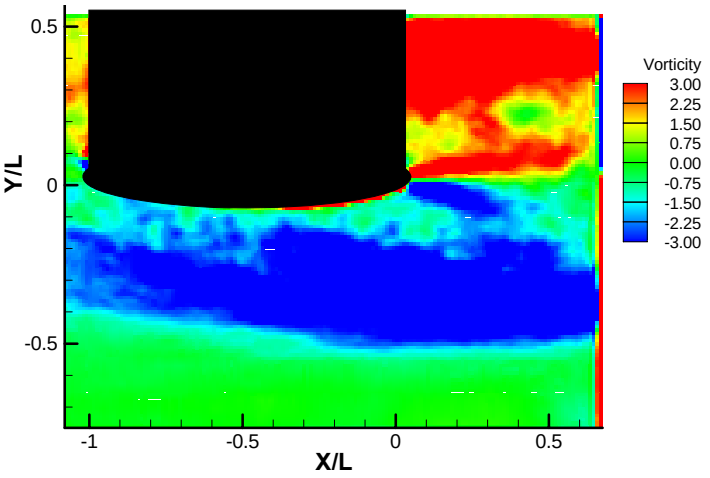

Figure 1.59. Mean vorticity field for max blowing.

1.4 CONCLUSIONS

The effect of Leading Edge Blowing (LEB) on the interaction between a circular cylinder wake and an airfoil was experimentally studied for an incompressible fluid. Results indicate that for structures on the order of the maximum airfoil thickness, the LEB effectively neutralizes or diffuses the vortices so that the interaction, and structural response, is minimized. Although flow control for the reduction of BVI has primarily focused on reducing the incident vortex strength in the past, LEB has shown that it can affect the incident vortex by breaking up its coherency, diffusing its strength over a larger region, or increasing the miss distance, all of which act to minimize the forcing which acts on an airfoil. In addition, we have shown that the global vorticity field is not a strong indicator of the unsteady loading which acts on the airfoil. Rather, it is the coherency of the forcing structure which plays the most prominent role in inducing unsteady loading.

The LEB jet can effectively neutralize or minimize the BVI when the vortices are of similar size to the airfoil thickness. However, as the vortex sizes increase, the LEB jet has less of an effect on the vortex, and this can be seen by comparing Case 1 and 2 where the wake generator is increased in size and incident vortices are diffused rather than completely broken up for a total loss of coherency. We cannot compare the RMS differences between the two cases directly due to the wake generator in Case 1 having a characteristic frequency near the natural frequency of the airfoil system and because the strength of the incident vortices changes as a function of the Reynolds number. However, for each case, the experimental data clearly indicates the LEB jet to have a positive effect on reducing the airfoil vibrations. Analysis of the PSD data indicates that the forcing frequency which acts on the airfoil surface is reduced in power when LEB is applied, and that instead of one large frequency which acts on the airfoil at the circular cylinder shedding frequency, this power is re-distributed over a wider range of frequencies.

It is interesting to note that the blowing slot asymmetry did not seem to have an adverse effect on the reduction of the airfoil vibrations. However, this may only be true for small wakes incident on the airfoil. Larger or stronger vortices might require a symmetric blowing configuration to effectively neutralize the BVI.

1.5 ACKNOWLEDGEMENTS

This research was sponsored by Techsburg, Inc. under ONR contract number N00014-03-M-0277. I extend my sincere thanks to the graduate students of CTFS for all their help in making this research proceed smoothly. In particular I thank Patrick Leung for his help with collection of the DPIV data.

1.6 REFERENCES

Abello, J., and George, A., "Wake Displacement Study of Attitude and Flight Parameter Modifications to Reduce Rotorcraft Blade-Vortex Interaction (BVI) Noise," 9th AIAA/CEAS Aeroacoustics Conference and Exhibit, 12-14 May 2003, Hilton Head, South Carolina, Paper Number AIAA 2003-3174.

Andrade, E.N.C., "The velocity distribution in a liquid-into-liquid jet. Part 2: The plane jet," Physical Soc., 51, 784-793, 1939.

Bull, M., Blazewicz, A., Pickles, J., and Bies, D. "Interaction Between a Vortex Wake and an Immersed Rectangular Plate," Experimental Thermal and Fluid Science, Vol. 12, pp. 209-220, 1996.

Hardin, J., and Lamkin, S., "Concepts for Reduction of Blade-Vortex Interaction Noise," Journal of Aircraft, Vol. 24, No. 5, 1986, pp. 120-125.

Hassan, A., Charles, B., Tadghighi, H., and Sankar, L., "Blade-Mounted Trailing Edge Flap Control for BVI Noise Reduction," NASA CR 4425, Feb. 1992.

Horner, M., Galbraith, R., Coton, F., Stewart, J., and Grant, I. "Examination of Vortex Deformation During Blade-Vortex Interaction," AIAA Journal, Vol. 34, No. 6, June 1996, pp. 1188-1194.

Kuo, C., and Hsiesh, J., "Parallel Interaction of Incident Vortex Array with Oscillating Airfoil," Journal of Aircraft, Vol. 35, No. 5, Sept-Oct 1998.

Lee, S. "Reduction of Blade-Vortex Interaction Noise Through Porous Leading Edge," AIAA Journal, Vol. 32, No. 3, March 1994.

Liu, Z., Sankar, L., and Hassan, A. "Alteration of the Tip Vortex Structure of a Hovering Rotor by Blowing," Presented at the 37th AIAA Aerospace Sciences Meeting and Exhibit, January 11-14, 1999, Reno, NV AIAA-99-0906.

Liu, Z., Russell, J., Sankar, L, and Hassan, A. "A Study of Rotor Tip Vortex Structure Alteration Techniques," Journal of Aircraft, Vol. 38, No. 3, 2001.

Malovrh, B. and Gandhi, F. "Sensitivity of Helicopter Blade-Vortex-Interaction Noise and Vibration to Interaction Parameters," Journal of Aircraft, Vol. 42, No. 3, 2005, pp. 685-697.

Mayori, A. and Rockwell, D. "Interaction of a Streamwise Vortex with a Thin Plate: A Source of Turbulent Buffeting," AIAA Journal, Vol. 32, No. 10, pp 2022-2029, October 1994.

Mullins, B., Smith, D., Rath, C., Thomas, S., "Helicopter Rotor Tip Shapes for Reduced Blade-Vortex Interaction – An Experimental Investigation. II", AIAA Paper 96-0149, 1996.

Preisser, J., Brooks, T., and Martin, R. "Recent Studies of Rotorcraft Blade-Vortex Interaction Noise," Journal of Aircraft, Vol. 31, No. 5, Sept-Oct 1994.

Rockwell, D. "Vortex-Body Interactions," Ann. Rev. Fluid Mech., Vol 30, 1998, pp 199-229.

Smith, D. and Sigl, D., "Helicopter Rotor Tip Shapes for Reduced Blade Vortex Interaction an Experimental Study", AIAA Paper 95-0192, 1995.

Wilder, M., and Telionis, D., "Parallel Blade-Vortex Interaction," Journal of Fluids and Structures, Vol. 12, 1998, pp. 801-838.

Wittmer, K. and Devenport, W., "Interaction of a Streamwise Vortex with a Full-Span Blade," Presented at the 26th AIAA Fluid Dynamics Conference, San Diego, CA, 1995. Paper No. AIAA-95-2214.

Yu, Y. "Miss Distance for Rotor Blade-Vortex Interaction Noise Reduction," Presented at the 2nd AIAA Aeroacoustics Conference, State College, PA, May 6-8, 1996.

2 Analysis of the Parallel Blade Vortex Interaction with Leading Edge Blowing Flow Control using the Proper Orthogonal Decomposition

This chapter is to be presented at the 2007 ASME FEDSM annual meeting in San Diego, California. Additional information on the Proper Orthogonal Decomposition analysis and results may be found in the Appendices.

Mr. Chris Weiland was the lead author and as such, collected and analyzed the data presented in this paper. He was also responsible for compiling the data into the form presented herein.

Dr. Pavlos Vlachos served as the lead author's advisor and was instrumental in the analysis and proof-reading of the final document.

Proceedings of FEDSM2007
5th Joint ASME/JSME Fluids Engineering Conference
July 30-August 2, 2007 San Diego, California USA

FEDSM2007-37275

ANALYSIS OF THE PARALLEL BLADE VORTEX INTERACTION WITH LEADING EDGE BLOWING FLOW CONTROL USING THE PROPER ORTHOGONAL DECOMPOSITION

Chris Weiland
Graduate Research Assistant
Virginia Tech Mechanical Engineering Department
Blacksburg, VA, USA

Pavlos Vlachos
Assistant Professor
Virginia Tech Mechanical Engineering Department
Blacksburg, VA, USA

ABSTRACT

Interactions of vortical unsteady flows with structures are often encountered in several engineering applications. Such flow structure interactions (FSI) can be responsible for generating significant loads and can have many detrimental structural and acoustic side effects, such as structural fatigue, radiated noise and even catastrophic results. Amongst the different types of FSI, the parallel Blade-Vortex Interaction is one of the most prominent.

The authors in a previous work (Weiland and Vlachos, 2006) reported an active flow control technique that successfully minimizes the parallel BVI. This technique is based on disrupting the incident vortex using a jet issued via Leading Edge Blowing (LEB), hence, hereon we term the method LEB. The effectiveness of the method was experimentally analyzed using Time-Resolved Digital Particle Image Velocimetry (TRDPIV) recorded at a rate sufficient to fully resolve the spatio-temporal dynamics of the flow field combined with simultaneous accelerometer measurements of the structure. These measurements quantitatively document the FSI dynamics. While our results demonstrated that for the range of our experimental parameters the LEB is successful in dramatically modifying the BVI, the question still remains as to which physical processes are responsible for this reduction.

This paper represents a continuation of our effort to further understand the dynamics of using active flow control to mitigate BVI. We present Proper Orthogonal Decomposition (POD) analysis of the temporally resolved planar flow fields for two extreme cases that were reported in the previous work. The two cases correspond to a large wake generator and a small wake generator. The POD technique was chosen specifically for its ability to reduce a complicated flow field into its optimal fundamental modes with a description of the energy contained in each mode, thereby simplifying the dynamics of a flow-field system for analysis.

Results of the POD analysis for the small wake generator indicate that for no LEB, the fundamental (i.e. most energetic) mode is given by the vortex shedding of the circular cylinder upstream. The addition of LEB reduces the energy contained in this fundamental mode. Thus the LEB jet has the effect of reducing the flow field coherency; the structure of

the exciting vortices is broken up into smaller vortices which have less or little effect on the transfer of energy from the wake to the airfoil. For the case of the large wake generator, the LEB jet has the opposite effect: the jet organizes the circular cylinder wake into flow structures that maintain their form, and thus the wake retains its ability to excite the airfoil into vibrations.

2.1 INTRODUCTION

The interaction of a fluid with a structure, causing unsteady loading and vibration, is ubiquitous in nature and engineering. The unsteady loading of a row of buildings due to a wind gust, the wing buffeting or fluttering phenomena and the flow induced vibrations in turbomachinery are all examples of fluid structure interactions (Jadic et al, 1998). These interactions can induce sizable loading of the structure, causing noise and significant structural fatigue (Rockwell, 1998).

A common fluid-structure interaction arises when a vortex passes over or collides with an airfoil. This interaction, termed a Blade-Vortex Interaction (BVI), is responsible for the blade-slap noise of helicopters. During certain maneuvers, a tip vortex from an upstream blade passes close to another blade. An unsteady pressure projection is thus placed upon the blade, which can respond elastically and also radiate noise. It has been shown that the parallel BVI is the most unfavorable situation for blade loading (Kuo and Hsiesh, 1994; Hardin and Lamkin, 1986).

Our past experiments have shown that Leading Edge Blowing (LEB), a flow control technique whereby a jet of fluid is expelled from the leading edge of an airfoil to act against an unsteady forcing wake, is effective at reducing BVI (Weiland and Vlachos, 2006). The experiments of Weiland and Vlachos utilized a double-arc sharp edge airfoil in the wake of a circular cylinder whose span was parallel to the span of the airfoil. The airfoil was allowed to oscillate only in a direction perpendicular to the freestream. This configuration is shown in Figure 2.1. TRDPIV was performed at 1kHz rate which is fast enough to resolve the spatio-temporal dynamics of the interaction and to obtain global planar quantitative flow field measurements coupled with accelerometer measurements of the airfoil vibration, thus rendering a complete view of the coupled flow field and airfoil dynamics. Although the LEB did decrease the vibrations of the airfoil, the mechanism of the LEB jet and vortex interaction was not immediately apparent.

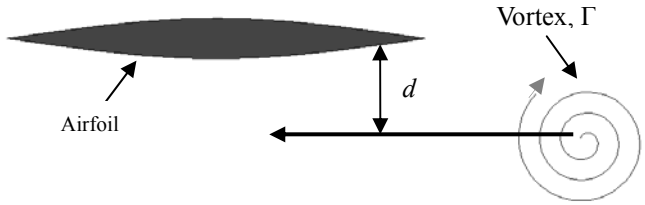

Figure 2.1. The parallel blade-vortex interaction.

The head-on collision of a jet and a vortex has received little attention in previous scientific works. In contrast, other interactions, such as the interaction between an exhaust jet and the wing- tip-vortex wake of an airplane have received considerable study as they are important to predict the motion of the trailing vortices which are present during take-off and landing of a plane. In particular, the turbulent mixing and vortex dynamics associated with this interaction has received considerable attention through numerical (Gago et al, 2002; Paoli et al, 2003) or experimental (Wang et al, 2000; Quackenbush, 1996) methods. Results of these investigations show that the jet and vortex wake can have a considerable influence on one another: in the case of the engine exhaust being partially directed into the vortex core it was shown that the vortex becomes unstable resulting in a decrease of angular momentum and diffusion of the vortex core (Paoli et al, 2003). In other cases, such as the near-field wake of a delta wing with the exhaust jet along the centerline of the planform, the persistent counter-rotating vortex pair substantially increases the jet spreading (Wang et al, 2000). Wang et al also note that the vortices induced by the exhaust jet only slightly influence the motion of the wing vortices by drawing them closer to the exhaust jet, and thus both the wing vortices and exhaust jet exert some measure of influence upon one another, depending

on their relative strengths and the distances between the two.

The jet-vortex interaction has also been studied from an atmospheric and oceanic sciences point of view as, for example, the interaction between a hurricane or cyclone and a zonal jet. This interaction can have implications on the trajectory of the vortex. Jets and these coherent structures can contribute greatly to the movement of heat and momentum and thus play a large role in mesoscale ocean dynamics (Vandermeirsch et al (Part I), 2003 and Vandermeirsch et al (Part II), 2003). In Vandermeirsch et al, the emphasis is placed on understanding how a vortex will cross the zonal jet and the nature of the vortex after the interaction has taken place. Although these numerical studies do provide analytic models for understanding when a vortex will cross the path of the jet, they do not consider jets strong enough to break up the coherency of the vortex, which is the primarily of this paper.

This study focuses on two conditions for the LEB: in the far wake of a small circular cylinder where the vortex street has had ample time to form, and the condition where the airfoil is in the mean closure point of a large circular cylinder. In the latter case, the LEB jet impacts the circular cylinder on its lee side. This condition has been studied in the past for plane (Hsiao et al, 1999; Hsiao et al, 2004; Chou et al, 2002) and round (Popiel and Trass, 1991; Cornaro et al, 1999; Fleischer et al 2001) jets; however these studies have been limited to jets impinging on a circular cylinder or convex/concave surfaces in quiescent flow. These studies have revealed feedback mechanisms between the jet and circular cylinder wake instabilities (Hsiao et al, 1999) through the upstream amplification of perturbations that act on the jet due to impingement. In the case of a round jet impinging on a flat plate (i.e. without curvature effects), it was found that the toroidal vortex structures formed from the jet shear layer impact the flat plate, where they are effectively stretched before they are absorbed and destroyed in the turbulent radial wall jet (Popiel and Trass, 1991). In all of the above cases there was no cross flow, and thus the effect of the circular cylinder boundary layer and that of the vortices shed from the cylinder and their interaction with the jet shear layer are not considered.

The simple turbulent planar jet as used in this study for the LEB has been studied in the past primarily focusing on the coherent structures developing and their organized motions (Gordeyev and Thomas, Part 1, 2000 and Gordeyev and Thomas, Part 2, 2002). These studies have shown the existence of a vortex street which closely resembles that of the von-Karman type, and strong interactions between these structures. However, the interaction of these structures with a circular cylinder boundary layer and its wake has never before been investigated.

In the present study cross flow acts upon the circular cylinder in addition to the LEB jet (from opposite directions), and thus the boundary layer developed on the circular cylinder by the cross flow and the boundary layer developed by the LEB jet impinging on the circular cylinder will interact (Figure 2.2). The contribution that this interaction has on the circular cylinder shedding frequency or the structure of the circular cylinder wake has not been studied.

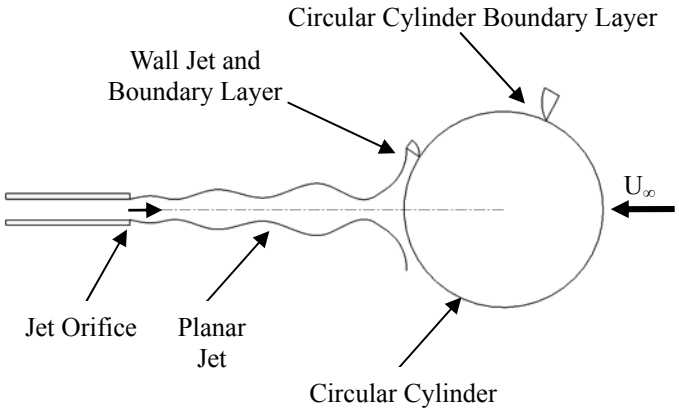

Figure 2.2. Plane jet impingement on a circular cylinder in the presence of cross flow.

2.2 THE PROPER ORTHOGONAL DECOMPOSITION

In order to analyze the complex spatio-temporal dynamics of this flow we employ Proper Orthogonal Decomposition (POD) on the TRDPIV results for

two of the cases that were reported in the previous work of Weiland and Vlachos. The two cases correspond to a large wake generator and a small wake generator. The POD technique was chosen specifically for its ability to reduce a complicated flow field into its fundamental modes with a description of the energy contained in each mode, thereby simplifying the dynamics of a flow-field system for analysis. POD does not require *a priori* knowledge of a suitable basis function for the flow field; the data is reduced into fundamental modes by mathematically choosing the energetically optimum basis function. The method has been used in the study of jets (Bi et al, 2003 and Shineeb et al, 2006), turbulence (Glegg and Devenport, 2001 and Smith et al, 2005), and a variety of other problems utilizing PIV.

Given a velocity ensemble *u*, the POD method seeks an optimal basis function φ such as to maximize the relationship

$$\max \frac{\left\langle (\mathbf{u},\varphi)^2 \right\rangle}{(\varphi,\varphi)} \qquad \mathbf{2}$$

Here $(\cdot,\cdot)$ denotes the inner product and $\langle\cdot\rangle$ the ensemble average. By aligning our problem as such, it is apparent that we seek the optimal basis function φ such that the average projection of the velocity field onto this basis function will be maximized, and thus the maximum average kinetic energy fraction will be obtained by the resulting eigenmodes φ. The solution to this problem is given by the calculus of variations; the maximum value of $\left\langle (u,\varphi)^2 \right\rangle$ is sought subject to the constraint that $(\varphi,\varphi)=1$. The complete problem is not formulated here; details may be found in Holmes et al, 1996.

The optimal basis functions can be obtained by solving the Fredholm equation of the second kind (Smith et al, 2005)

$$\int \mathbf{R}(\mathbf{x},\mathbf{x}')\varphi(\mathbf{x}')d\mathbf{x}' = \lambda\varphi(\mathbf{x}) \qquad \mathbf{3}$$

The kernel of the previous equation is given by the autocorrelation tensor averaged over the sampled data

$$\mathbf{R}(\mathbf{x},\mathbf{x}') = \left\langle \mathbf{u}(\mathbf{x}) \otimes \mathbf{u}*(\mathbf{x}') \right\rangle \qquad \mathbf{4}$$

Here $\otimes$ is the tensor product and $*$ denotes the complex conjugate. Note that here $\mathbf{x}=(x,y,z)$. Thus, the solution results in a series of uncorrelated orthogonal functions, given by the solution of Equation 2. The result of solving this equation yields a series of eigenmodes and eigenfunctions which can be used to reconstruct the original velocity field by linearly superimposing the individual modes as in Equation 4, where $a_i(t)$ are time dependent projection coefficients; details on their calculation can be found in Smith et al.

$$\mathbf{u}(\mathbf{x},t) = \sum_{i=1}^{N} a_i(t)\varphi_i(\mathbf{x}) \qquad \mathbf{5}$$

Eigenfunctions corresponding to high energy modes are the primary flow components, and thus POD is appealing as a method for the identification of coherent structures. As the total flow energy is the summation of all modes' contributions, the ones with the largest eigenmodes will dominate the flow field. The contribution of an individual eigenmode to the overall energy of the flow may be described as

$$Energy\ Fraction = \frac{\lambda_i}{\sum_{j=1}^{\infty}\lambda_j} \qquad \mathbf{6}$$

Since φ is dimensionless and by Equation 3 $\mathbf{R}(\mathbf{x},\mathbf{x}')$ must have dimensions of m^2/s^2, and thus λ also has dimensions of specific energy (i.e. mass normalized). Thus the dominant structures of the flow may be categorized by the specific energy of the individual mode with the larger eigenvalues corresponding to more energetic modes contained in the flow.

There are several methods by which the ensemble average of the kernel **R** is calculated, and as such different orthogonal decompositions will result (Braud et al, 2004). The classical method, given by Equation 3, utilizes the assumption of ergodicity in a statistically stationary flow. The ensemble average is given as a temporal average, where *R* is a two-point space correlation tensor. **R** may also be calculated using a spatial average (the method of snapshots). **R** is then a two point time correlation tensor (Braud et al, 2004). However, for the same discrete set of finite data, both approaches

are equivalent (Sirovich, 1987), and thus the choice of which method to use becomes a matter of practicality, i.e. which method will result in the least number of calculations. In most situations, the method of snapshots is more computationally efficient, as the number of spatially sampled grid points is much greater than the number of points sampled in time. The POD method used in the reduction of the data presented herein utilized the method of snapshots, as is typical for spatially data rich fields such as given by computational fluid dynamics or DPIV studies. It should be noted that originally there were 18369 vectors in the flow field, but for computational reasons every other vector was sampled in the POD analysis. Additionally, the temporal resolution was decreased from 800 to 400 Hz. Since the maximum vortex shedding frequency is on the order of 6 Hz, the decreased temporal resolution is not problematic. Some spatial resolution is lost in sampling every other vector in the POD analysis, but there are still an adequate number of flow vectors to represent the field.

2.3 NOMENCLATURE

Γ – Vortex circulation
a – Projection coefficient
d – Vortex stand-off distance
h_{slot} – Blowing slot height
U_j – Jet velocity
w – Airfoil thickness
U_∞ - Freestream Velocity
u - velocity ensemble
φ – POD optimal basis function
λ – POD mode eigenvalues
R – cross correlation tensor
C_μ – Momentum coefficient $C_\mu = 2\frac{U_j^2 h_{slot}}{U_\infty^2 w}$

2.4 EXPERIMENTAL

The experimental setup used to collect and analyze the DPIV and accelerometer data is reported in the authors' previous work (Weiland and Vlachos, 2006). A brief summary of the experimental setup is presented here, and readers are referred to the previous authors' work for a more in-depth look. The experiments simulate the interaction of an unsteady forcing wake and an airfoil. In addition to DPIV flow field measurements, the airfoil vibrations were also measured at simultaneous points in time.

The experiments were conducted in a water tunnel in the Engineering Sciences and Mechanics fluid mechanics laboratory at Virginia Tech. The water tunnel is able to produce a freestream of up to 1 m/s with 3% turbulence within a test section of 2'x2'x5'. The experimental apparatus is shown in Figure 2.3. A double arc (sharp leading and trailing edge) airfoil with a chord of 3.4" and span of 8" was placed downstream and parallel to a circular cylinder at zero degrees angle of attack along the centerline of the circular cylinder. The airfoil is symmetric with a maximum thickness of 0.58". A slot, used for the injection of a water jet, runs almost the entire span of the airfoil and is located on the bottom side of the leading edge only. The airfoil is allowed to translate in response to the wake of the cylinder, and linear springs act to restore the airfoil to its rest position. The airfoil is free to oscilate only in a direction perpendicular to the flow direction, constrained by two rods on very low friction linear bearings. Two accelerometers are attached to a strut rigidly mounted to the airfoil. Plexiglas side walls are used to mitigate end-effects of the airfoil and the circular cylinder and to permit optical access. The system was rigidly mounted in the test section and its natural frequency was experimentally determined to be 12 Hz.

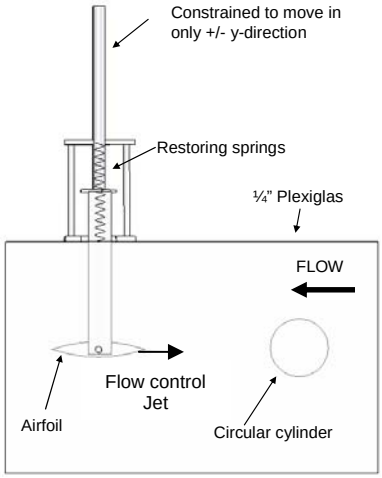

Figure 2.3. Experimental apparatus to study the LEB effect on a parallel BVI.

2.5 RESULTS AND DISCUSSION

The POD was used to decompose the DPIV flow fields into their fundamental modes. By the POD method, larger eigenvalues indicate that the corresponding eigenmodes contain more of the flow field energy. For the results presented herein, the mean flow field velocity was subtracted before the analysis was performed. The representative flow fields without the mean flow field velocity can be found in the Appendices.

Here we present results for only two of the four conditions reported in Weiland and Vlachos (2006) and Weiland, (2006), that of a small cylinder (0.75" diameter) and a large cylinder (2" diameter). These conditions were selected because they correspond to dramatically different results with respect to the effectiveness of the flow control method and how it is affecting the transfer of energy from the flow field to the airfoil. For the smaller cylinder, the LEB decreases the airfoil vibrations up to 40% (Weiland and Vlachos, 2006). In contrast, for the larger cylinder, the LEB significantly increases the airfoil vibrations. This disparity between the two cases is the motivation to understand how the LEB flow control and its interaction with the incident wake modifies the FSI on the downstream blade.

2.5.1 Analysis of Small Wake Generator/Airfoil Interaction

For the case of the small cylinder the energy contained in the POD modes is shown in Figure 5 and Figure 6. Except for C_μ=0.14, there is a clear trend of descending energy contained in the first mode. This trend is also seen in the second mode, which together compromise 40-50% of the total flow energy, depending on the degree of LEB. In the case of high degrees of LEB, more eigenmodes are required to capture a large degree of the flow energy. For example, for C_μ=0, it takes 127 modes to capture 90% of the total flow energy. For C_μ=0.14 it takes 136 modes to capture the same amount of flow energy. For C_μ=0.22 it takes 163 modes to capture 90% of the total flow energy. The fact that more eigenmodes are needed to capture the same amount of flow energy for the blowing compared to the no-blowing cases indicates that in the first case the flow is less organized. In the case of a highly organized flow field, such as that given by a von Karman vortex street, the fundamental modes of the flow field are very distinct (an array of vortices). As the flow becomes less organized, more modes are required to describe the flow field. Therefore, we can conclude that LEB jet colliding with the incident flow structures (cylinder wake vortices) results in breaking up their coherency.

For the C_μ=0.05 case, the previously described trend does not hold. At 4 modes, eigenmodes become much more energetic than all others (Figure 1.56). There is no indicator in the data that accounts for this divergence.

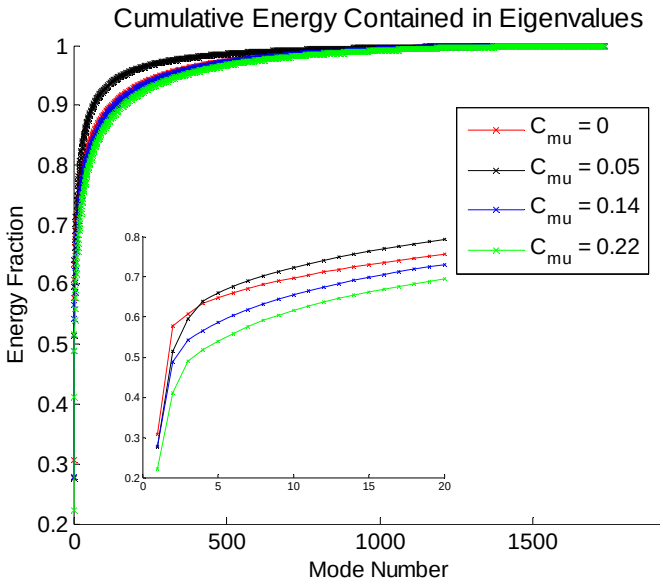

Figure 2.4. Cumulative energy distribution from the POD modes.

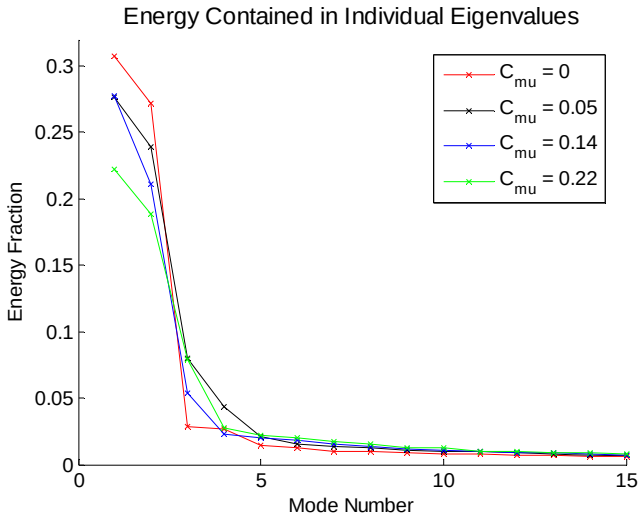

Figure 2.5. Energy distribution of individual modes.

Since the POD modes represent the flow structures organized by their energy contribution to the total flow, we can compare the most energetic modes for the blowing and no-blowing cases to reveal the interaction mechanism responsible for the reduction in BVI. A comparison between the first six modes for the no-blowing (about 65% total energy) and maximum blowing (about 55% total energy) cases are shown below. Comparing the first mode of the no-blowing and maximum blowing cases yields an interesting flow structure change at the tip of the airfoil leading edge. For the no-blowing case a well defined vortex exists just below the airfoil (y/c~-0.1, x/c~0) leading edge, whereas in the maximum blowing case a skewed vortex exists below the airfoil leading edge but it is displaced further away. The second mode for the LEB case shows vortices directly under the airfoil surface as displaced further away than when compared to the no-blowing case. The third mode is a convection mode. Note that the direction of the flow vectors in the mode shapes is arbitrary; this fact will become apparent when viewing the projection coefficient (PC) evolution in time.

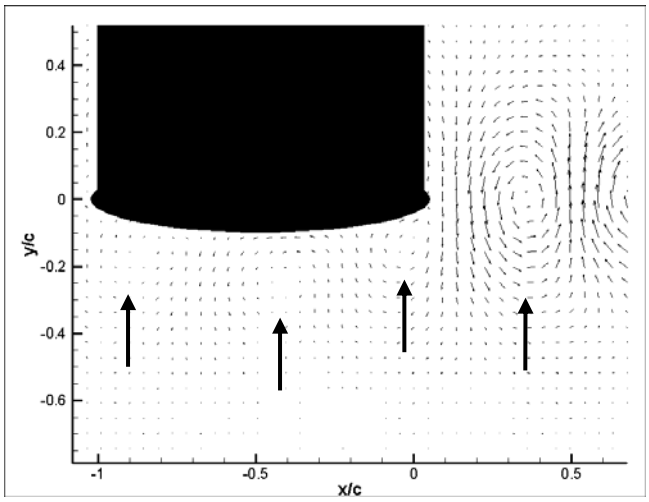

Figure 2.6. No-blowing case, mode 1.

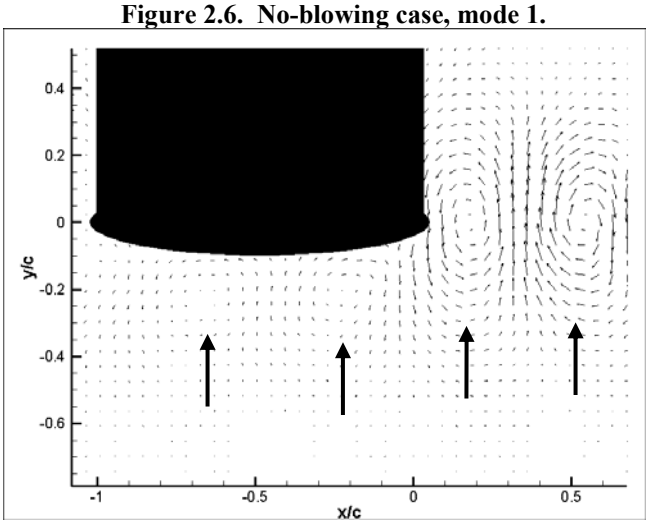

Figure 2.7. No-blowing case, mode 2.

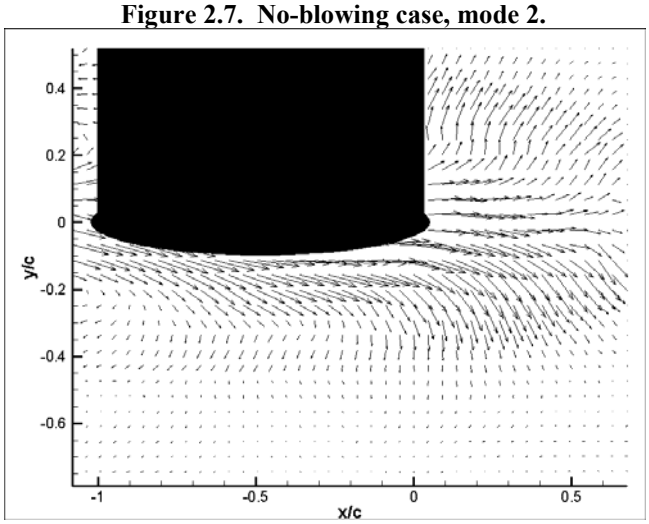

Figure 2.8. No-blowing case, mode 3.

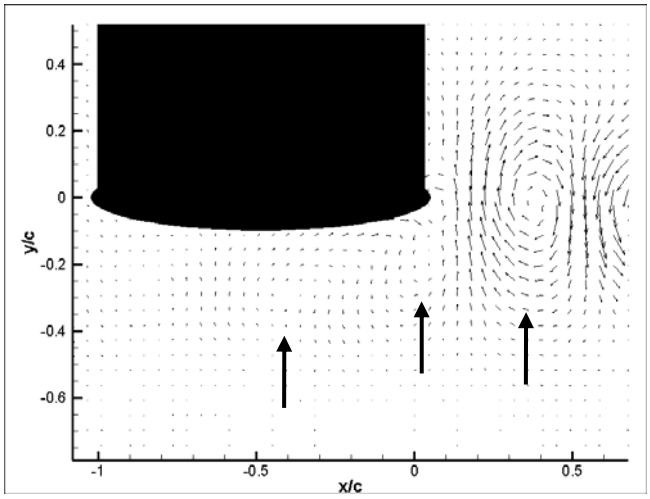

Figure 2.9. Max-blowing case, mode 1.

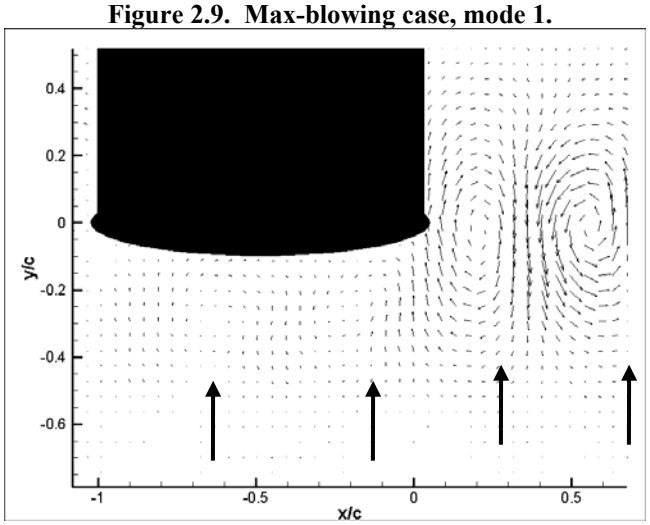

Figure 2.10. Max-blowing case, mode 2.

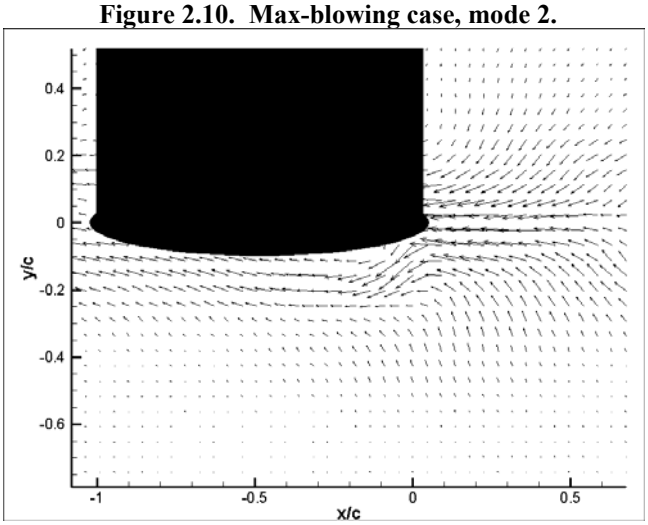

Figure 2.11. Max-blowing case, mode 3.

The projection coefficients (PC) for the first six modes were analyzed to ascertain what each mode physically corresponds to; the first three PC are reported here. These are shown in Figure 2.12-Figure 2.17. The five largest spectra components are noted on the Figures. Note that the magnitude of the PC fluctuates in intensity and sign; the linear superposition of each mode shape with their time-varying PC computes a proper reconstruction of the original flow field. Thus, the direction of the flow field vectors in the static mode shapes is arbitrary. For each mode, both the PC and its Power Spectral Density (PSD) are shown. For both the no-blowing and maximum blowing cases, the first and second modes correspond to the shedding frequency of the circular cylinder (about 5.9 Hz). The third mode is very low frequency in both cases (less than 0.7 Hz), which indicates an almost steady-state mode shape. This agrees with the qualitative assessment of the third mode shape as a vortex convection mode. Note that the POD results show that the vortex shedding is still taking place at the regular shedding frequency, which implies that the LEB jet is not having an effect on the circular cylinder shedding mechanisms.

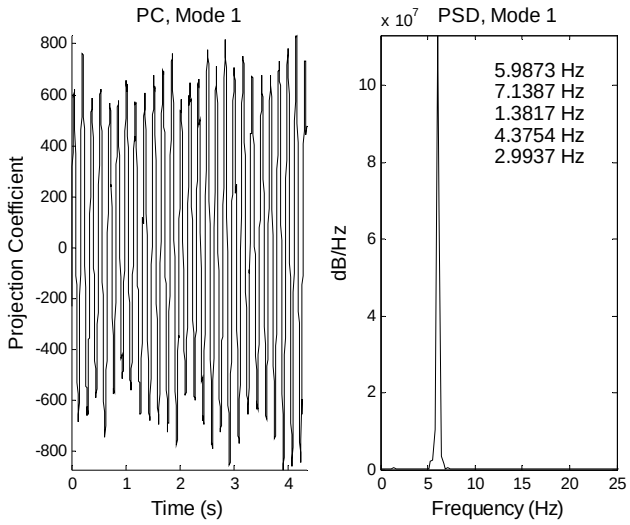

Figure 2.12. No-blowing case, mode 1 projection coefficient.

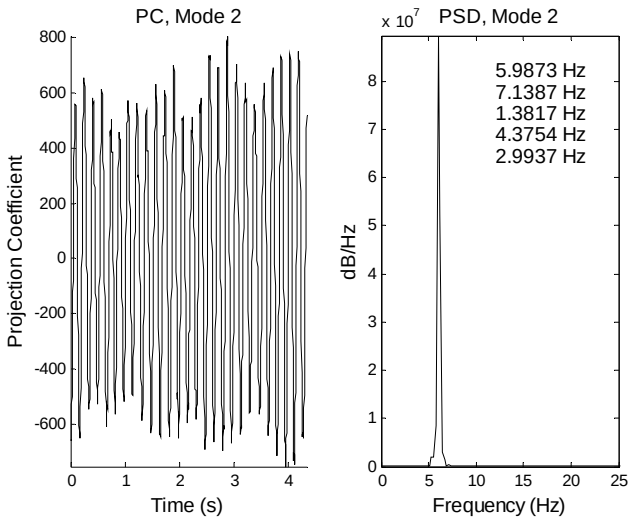

Figure 2.13. No-blowing case, mode 2 projection coefficient.

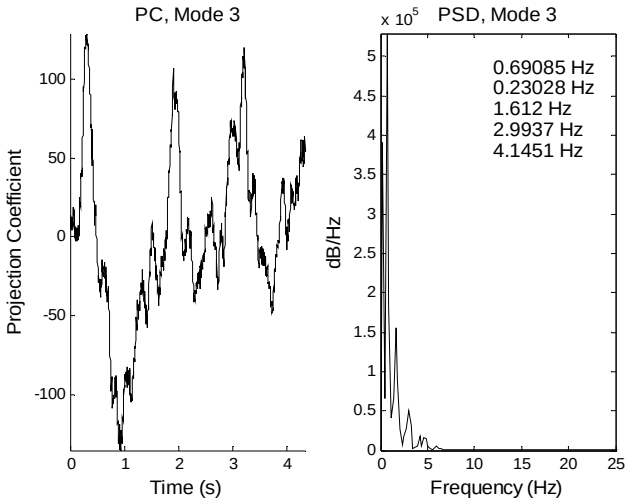

Figure 2.14. No-blowing case, mode 3 projection coefficient.

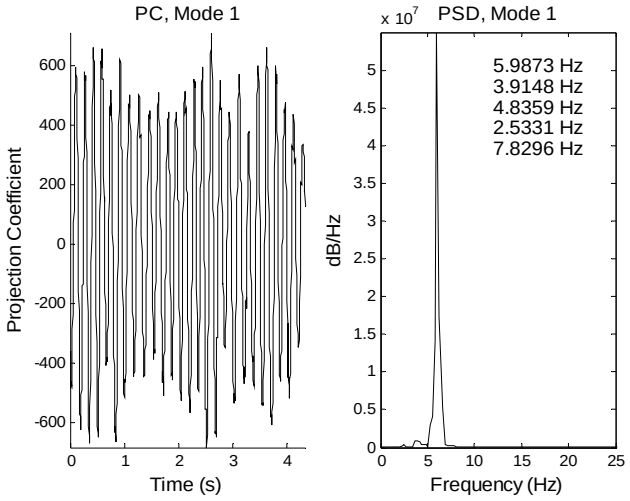

Figure 2.15. Max-blowing case, mode 1 projection coefficient.

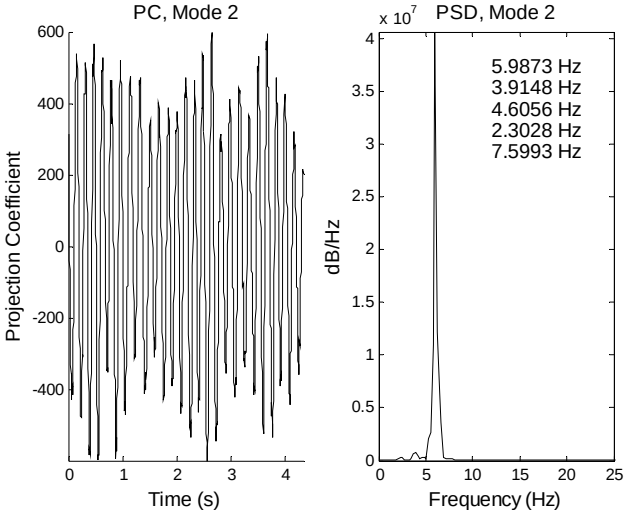

Figure 2.16. Max-blowing case, mode 2 projection coefficient.

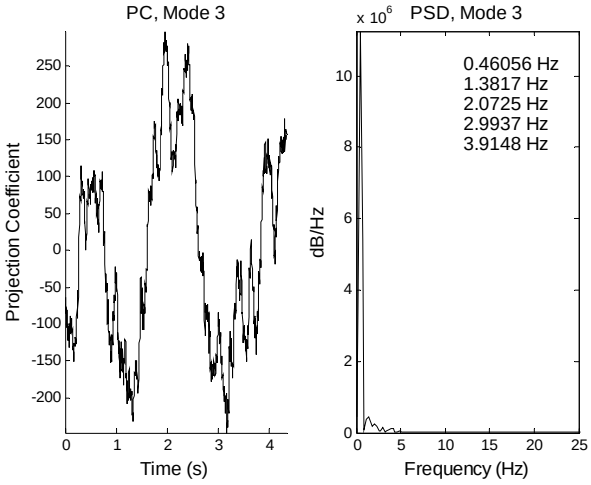

Figure 2.17. Max-blowing case, mode 3 projection coefficient.

2.5.2 Analysis of Large Wake Generator/Airfoil Interaction

For the case of the large circular cylinder wake, the use of LEB had a detrimental effect on the BVI. The airfoil is in close proximity to the edge of the circular cylinder (about 2 circular cylinder diameters). Thus, the vortex street has not had ample distance to form.

Analysis of the qualitative flow visualization is insightful. A comparison of Figure 19 and Figure 20, which are typical of the images captures for the C_μ=0 and C_μ=0.21 cases, respectively, show an interesting phenomenon. Because the airfoil is so close to the large cylinder, it impedes the

development of the vortex street, acting as a splitter plate. Instead of a vortex street, a highly turbulent and undeveloped wake propagates from the circular cylinder with a strong recirculation zone directly in the wake of the cylinder, which acts to draw fluid from the airfoil leading edge upstream. For C_μ=0.21, the jet penetrates into this dead-water region and appears to "spin up" the vortices along the region of high shear between the dead-water region directly in the wake of the circular cylinder and the undisturbed flow, outside of the zone of influence of the circular cylinder wake. Five clear vortices are seen and marked with red arrows when the LEB is on. The vortices are symmetric on the trailing edge of the circular cylinder, and become skewed (with respect to the top and bottom vortices on either side of the airfoil surface). This could, perhaps be caused by the asymmetric LEB slot, which acts to inject fluid with greater velocity (energy) on the bottom side of the airfoil.

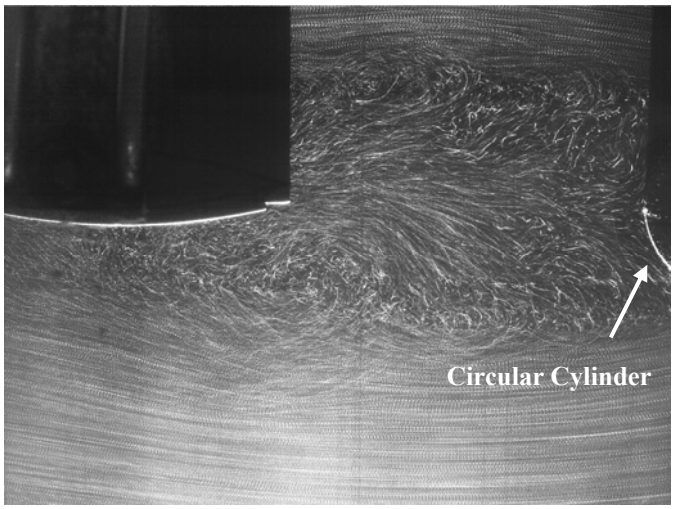

Figure 2.18. Flow visualization for Case 5, no blowing.

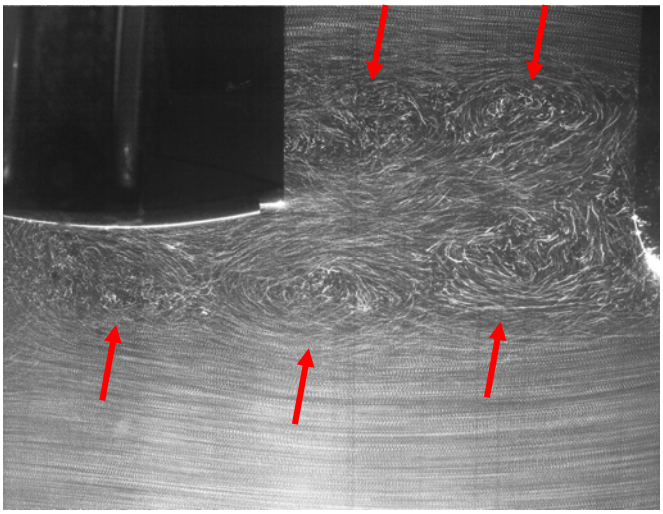

Figure 2.19. Flow visualization for Case 5, max blowing.

The energetics of the POD modes are shown in Figure 21 and Figure 22. Note that in the first mode alone, the non-blowing case contains 10% of the total energy, while for C_μ=0.21 the first mode contains about 16% of the total energy. For both cases only about 1% of the flow energy is contained in each of the modes past 20. It takes 331 eigenmodes to reconstruct 90% of the flow energy for the no blowing case while it takes 189 to reconstruct the same energy in the blowing case. As opposed to the previous situation, in which blowing acted to disrupt the flow field making it less organized, for the large cylinder the blowing increases the organization of the circular cylinder wake.

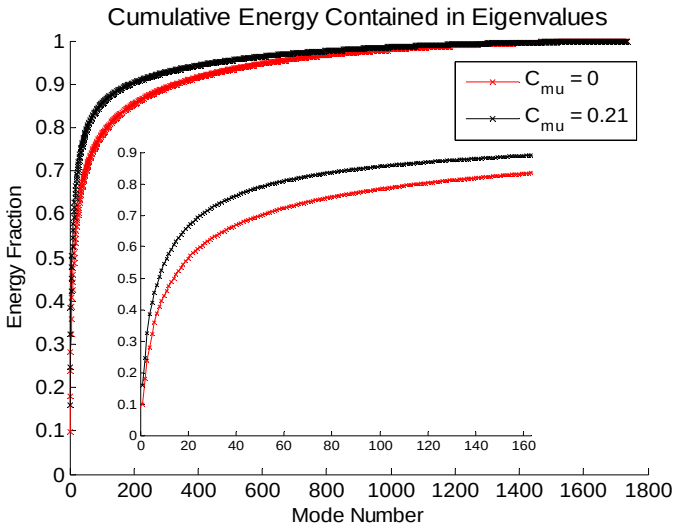

Figure 2.20. Cumulative energy contained in eigenmodes.

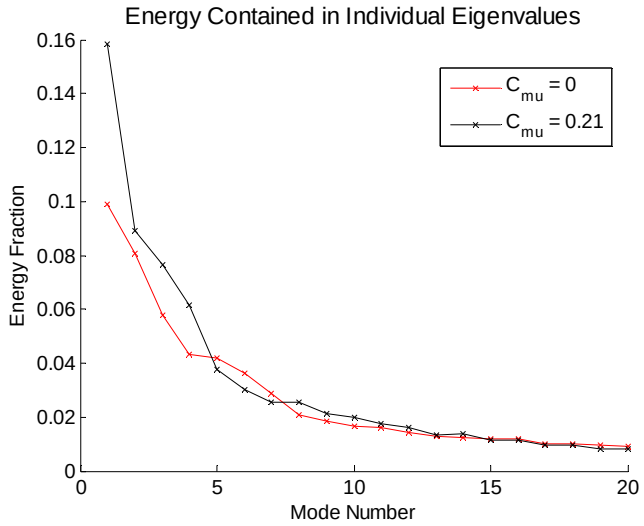

Figure 2.21. Energy contained in individual eigenmodes.

The individual modes for the no-blowing case are shown in Figure 23-Figure 28. A comparison of the first modes for both blowing cases is interesting as it is readily apparent the "dead-water region" directly behind the circular cylinder is much more active with LEB. In addition, strong velocity vectors which track the closure point of the circular cylinder wake are displaced further downstream with LEB (marked with arrow). For the no-blowing case, modes three and four clearly show an evolution of vortices along the circular cylinder wake shear layer (marked with arrows). The PC and their spectra are shown in Figure 29-Figure 34. For the no-blowing case, modes three and four show strong spectral components at about 2-2.5 Hz, which is the predicted shedding frequency of the circular cylinder. Additionally, mode 1 for the no-blowing case and mode 2 for the maximum blowing case qualitatively resemble one another in shape, but a comparison of the spectra indicate differences. For the no-blowing case, the largest spectral component is very low frequency, while in the maximum blowing case; the largest spectral component for the maximum blowing case is seen at about 2 Hz. This is very close to the large power increase seen in Figure 1.53 at about 2 Hz at the maximum blowing rate. The LEB jet affects the flow field in such a way to re-arrange the distribution of energy in the flow field by creating a new first mode.

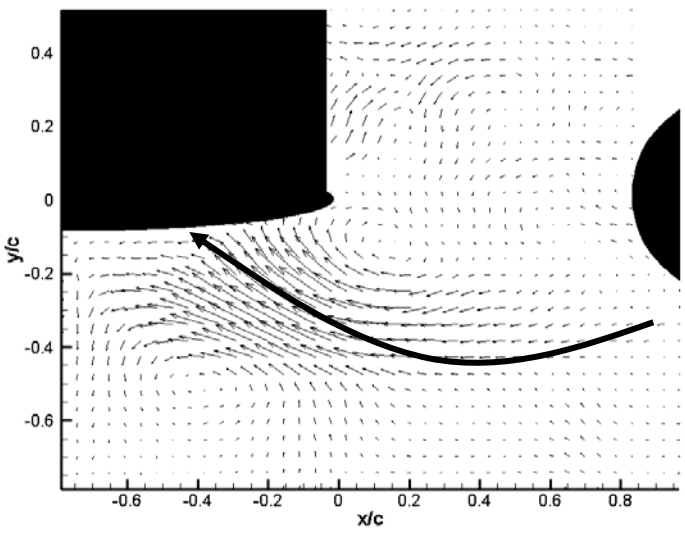

Figure 2.22. No-blowing case, mode 1.

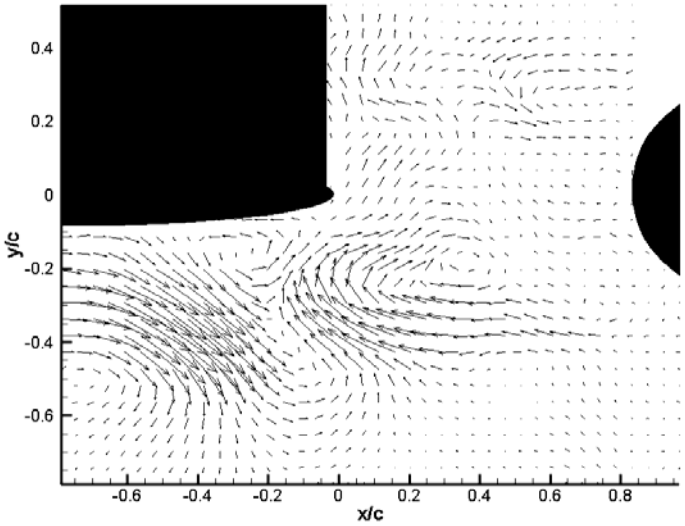

Figure 2.23. No-blowing case, mode 2.

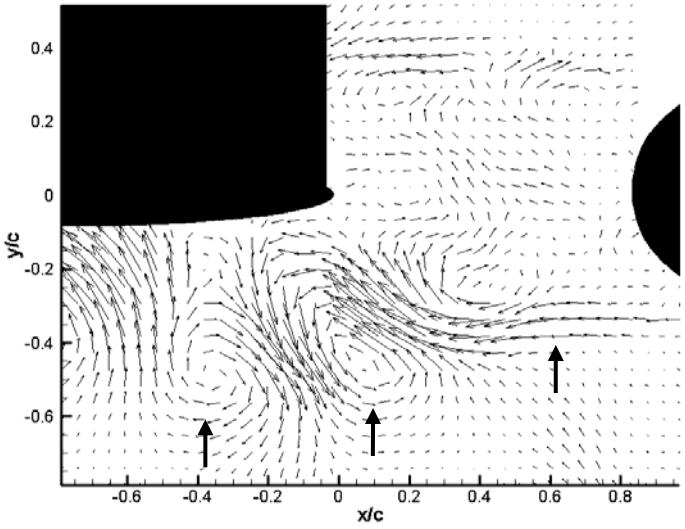

Figure 2.24. No-blowing case, mode 3.

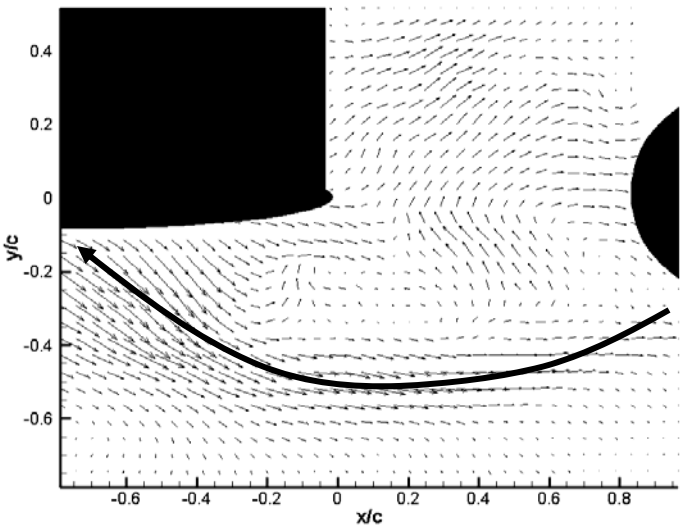

Figure 2.25. Max-blowing case, mode 1.

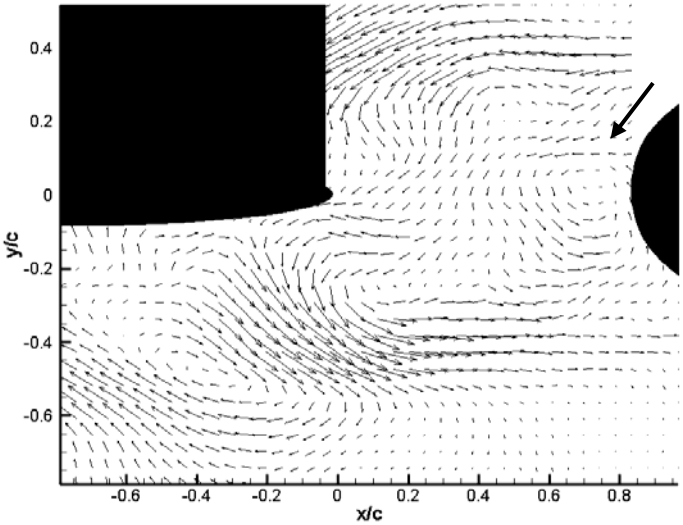

Figure 2.26. Max-blowing case, mode 2.

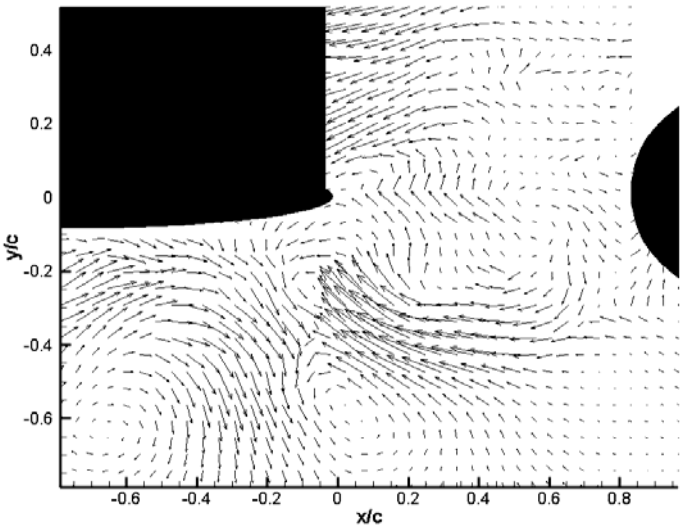

Figure 2.27. Max-blowing case, mode 3.

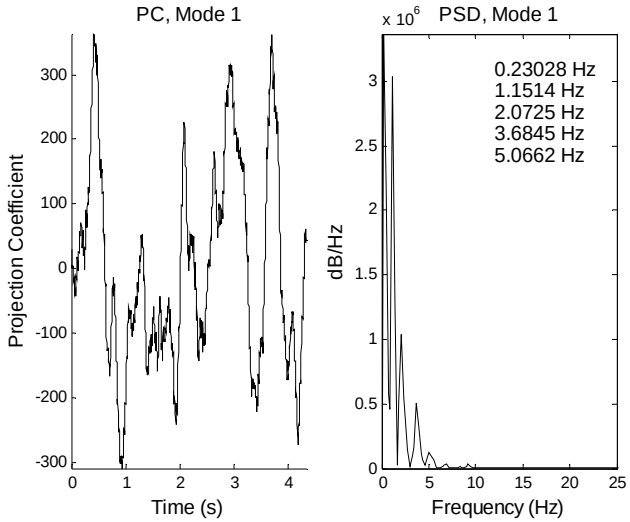

Figure 2.28. No-blowing case, mode 1 projection coefficient.

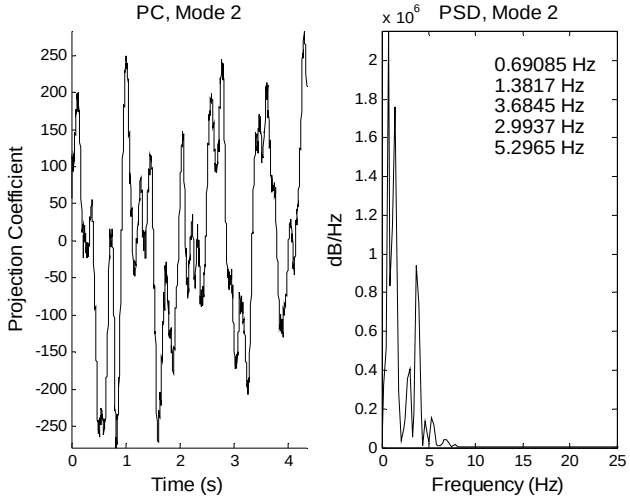

Figure 2.29. No-blowing case, mode 2 projection.

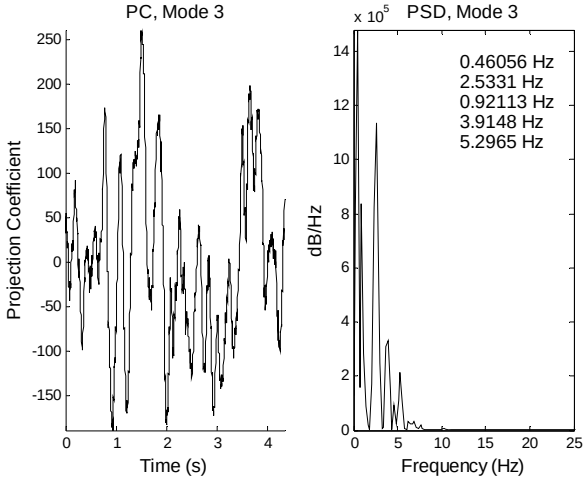

Figure 2.30. No-blowing case, mode 3 projection coefficient.

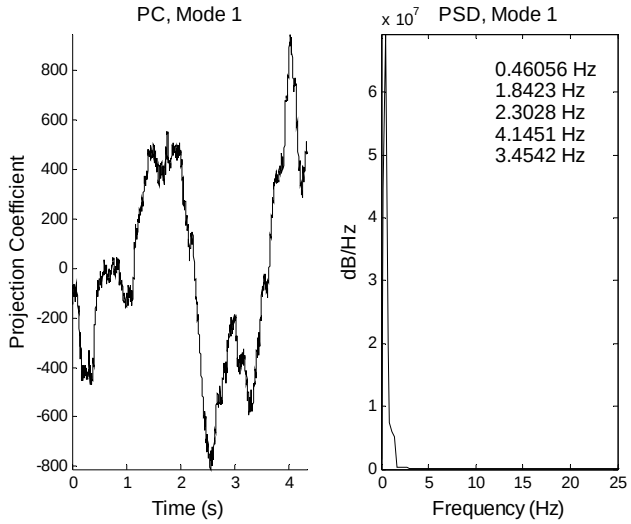

Figure 2.31. Max-blowing case, mode 1 projection coefficient.

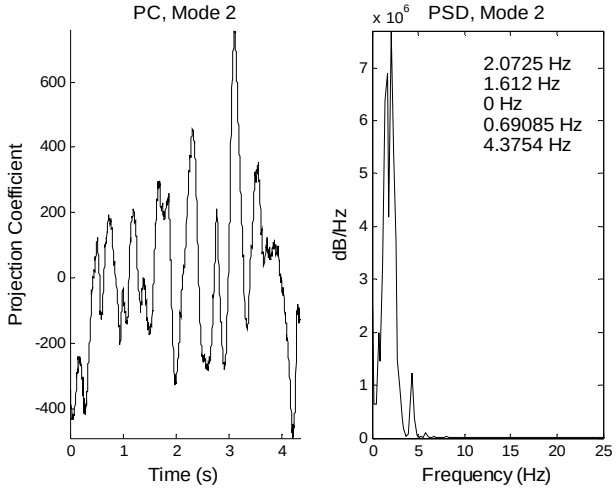

Figure 2.32. Max-blowing case, mode 2 projection coefficient.

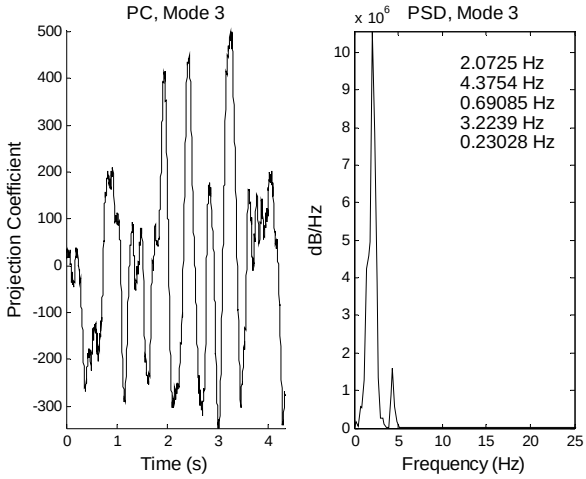

Figure 2.33. Max-blowing case, mode 3 projection coefficient.

2.6 CONCLUSIONS

Use of the Proper Orthogonal Decomposition (POD) has allowed the analysis of the fundamental flow structures of the Leading Edge Blowing (LEB) flow control modified parallel blade-vortex interaction. The interaction of the LEB jet with the circular cylinder wake was shown to be effective for reducing parallel blade-vortex interactions (BVI) when the airfoil is outside of the mean closure point of the circular cylinder. Large decreases in the airfoil vibration levels were recorded for this condition. The interaction can also be detrimental, as in the case when the blade is within the mean closure point of the circular cylinder. In this case, large increases in the airfoil vibration were recorded.

For the case of a favorable LEB/circular cylinder wake interaction, the POD results show that the LEB jet decreases the coherency of the circular cylinder wake with LEB; this was demonstrated by showing that more eigenmodes were required to achieve similar flow field energy than when compared to the no-blowing case. Additionally, the POD modes indicate a change in the structure of the flow field near the airfoil with LEB, indicating that the jet does not have an effect on the vortices from the circular cylinder upstream, but rather affects the flow field near the jet to produce a reduction in BVI.

For the case of a detrimental LEB/circular cylinder wake interaction, the POD results indicated several changes with the LEB jet. One of the POD modes also picked up the circular cylinder shear layer growth for the no-blowing case, which is not seen in the maximum blowing case. In contrast to the smaller cylinder case, the LEB acted to increase the level of coherency in the circular cylinder wake when compared to the no-blowing case. This was reflected in the energy contained in the individual eigenmodes, as well as the structure of the modes.

2.7 ACKNOWLEDGEMENTS

This research was sponsored by Techsburg, Inc through ONR contract number N00014-03-M-0277. The authors also wish to acknowledge the help of Patrick Leung in taking the initial DPIV data, and John Charonko for the use of his POD code.

2.8 REFERENCES

Braud, C., Heitz, D., Braud, P., Arroyo, G., and Delville, J. "Analysis of the wake-mixing-layer interaction using multiple plane PIV and classical POD." Experiments in Fluids, Vol. 37, 2004, pp. 95-104.

Bi, W., Sugii, Y., Okamoto, K., and Madarame, H. "Time-resolved proper orthogonal decomposition of the near-field flow of a round jet measured by dynamic particle image velocimetry." Measurement Science and Technology, Vol. 14, 2003, L1-L5.

Chou, Y., Hsiao, F., Hsu, C., Huang, J. "Vortex dynamics and energy transport of a plane jet impinging upon a small cylinder," Experimental Thermal and Fluid Science, Vol. 26, pp 445-454, 2002.

Cornaro, C., Fleischer, A., and Goldstein, A. "Flow visualization of a round jet impinging on cylindrical surfaces," Experimental Thermal and Fluid Science, Vol. 20, pp 66-78, 1999.

Fleischer, A., Kramer, K., and Goldstein, R. "Dynamics of the vortex structure of a jet impinging on a convex surface," Experimental Thermal and Fluid Science, Vol. 24, pp 169-175, 2001.

Glegg, S. and Devenport, W. "Proper Orthogonal Decomposition of Turbulent Flows for Aeroacoustic and Hydroacoustic Applications," Journal of Sound and Vibration, Vol. 239, No. 4, 2001, pp 767-784.

Gago, C., Brunet, S., and Garnier, F. "Numerical Investigation of Turbulent Mixing in a Jet/Wake Vortex Interaction," AIAA Journal, Vol. 40, No. 2, 2002.

Gordeyev, S. and Thomas, F. "Coherent structure in the turbulent planar jet. Part 1. Extraction of proper orthogonal decomposition eigenmodes and their self-similarity," Journal of Fluid Mechanics, Vol. 460, pp. 349-380, 2002.

Gordeyev, S. and Thomas, F. "Coherent structure in the turbulent planar jet. Part 2. Structural topology via POD eigenmode projection," Journal of Fluid Mechanics, Vol. 460, pp. 349-380, 2002.

Hardin, J., and Lamkin, S. "Concepts for Reduction of Blade-Vortex Interaction Noise," Journal of Aircraft, Vol. 24, No. 5, 1986, pp. 120-125.

Holmes, P., Lumley, J., and Berkooz, G. *Turbulence*, *Coherent Structures*, *Dynamical Systems and Symmetry*, Cambridge University Press, Cambridge, UK, 1996.

Hsiao, F., Chou, Y., and Huang, J. "The study of self-sustained oscillating plane jet flow impinging upon a small cylinder," Experiments in Fluids, Vol 27, pp 392-399, 1999.

Hsiao, F., Hsu, I., Huang, J. "Evolution of coherent structures and feedback mechanism of the plane jet impinging on a small cylinder," Journal of Sound and Vibration, Vol. 278, pp 1163-1179, 2004.

Jadic, I., So, R., and Mignolet, M. "Analysis of Fluid-Structure Interactions Using a Time-Marching Technique." Journal of Fluids and Structures, Vol. 12, 1998, pp 631-654.

Kuo, C., and Hsiesh, J. "Parallel Interaction of Incident Vortex Array with Oscillating Airfoil," Journal of Aircraft, Vol. 35, No. 5, Sept-Oct 1998.

Paoli, R., Laporte, F., Cuenot, B. "Dynamics and mixing in jet/vortex interactions," Physics of Fluids, Vol. 15, No. 7, 2003.

Popiel, C. and Trass, O. "Visualization of a Free and Impinging Round Jet," Experimental Thermal and Fluid Science, Vol. 4, pp 253-264, 1991.

Rockwell, D. "Vortex-Body Interactions," Ann. Rev. Fluid Mech., Vol. 30, 1998, pp 199-229.

Shineeb, A., Balachandar, R., and Bugg, J. "Quantitative Investigation of Coherent Structures in a Free Jet using PIV and POD," Presented at the 2006 ASME Joint U.S.-European Fluids Engineering Summer Meeting, Miami, FL, July 17-20.

Sirovich, L. "Turbulence and the dynamics of coherent structures. 1: Coherent structures." Q Appl Math, Vol. 45, 1987, pp 561-571.

Smith, T., Moehlis, J., and Holmes, P. "Low-Dimensional Modelling of Turbulence Using the Proper Orthogonal Decomposition: A Tutorial," Nonlinear Dynamics, Vol. 41, 2005, pp 273-307.

Vandermeirsch, F., Carton, X., and Morel, Y. "Interaction between an eddy and a zonal jet Part I. One-and-a-half-layer model," Dynamics of Atmospheres and Oceans, Vol. 36, pp 247-270, 2003.

Vandermeirsch, F., Carton, X., and Morel, Y. "Interaction between an eddy and a zonal jet Part II. Two-and-a-half-layer model," Dynamics of Atmospheres and Oceans, Vol. 36, pp 271-296, 2003.

Wang, F., Proot, M., and Charbonnier, J. "Near-Field Interaction of a Jet with Leading-Edge Vortices," Journal of Aircraft, Vol. 37, No. 5, 2000.

Weiland, C., and Vlachos, P. "Modification of Blade Vortex Interactions Using Leading Edge Blowing," Presented at the 2006 ASME Joint U.S.-European Fluids Engineering Summer Meeting, Miami, FL, July 17-20.

Quackenbush, T., Teske, M., and Bilanin, A., "Dynamics of Exhaust Plume Entrainment in Aircraft Vortex Wakes," AIAA paper 96-0747, Jan. 1996.

3 Appendix I – Characterization of Test Apparatus

The LEB test apparatus was characterized in a simple manner to ascertain the natural frequency of the system. Characterization of the test apparatus was accomplished by placing the apparatus in the test section of the water tunnel fully secured to the water tunnel. Lateral motions were suppressed by employing rods (4 on each side, see Figure 3.1), perpendicular to the direction of water travel, that were tightly fit against the water tunnel walls. The cross flow velocity was zero, and no jet blowing was attempted. The natural frequency of the airfoil was determined by striking the top of the linear bearing rods with a metallic blunt instrument for both in-plane and out-of-plane motion (see Figure 3.1). The natural frequency was determined to be 12 Hz for in-plane motion (see Figure 3.2) and 15 hz for out-of-plane motion (see Figure 3.3), although for a given excitation of the airfoil, the in-plane motion dominates the vibration response. In other words, it is quite hard to excite the out-of-plane motion.

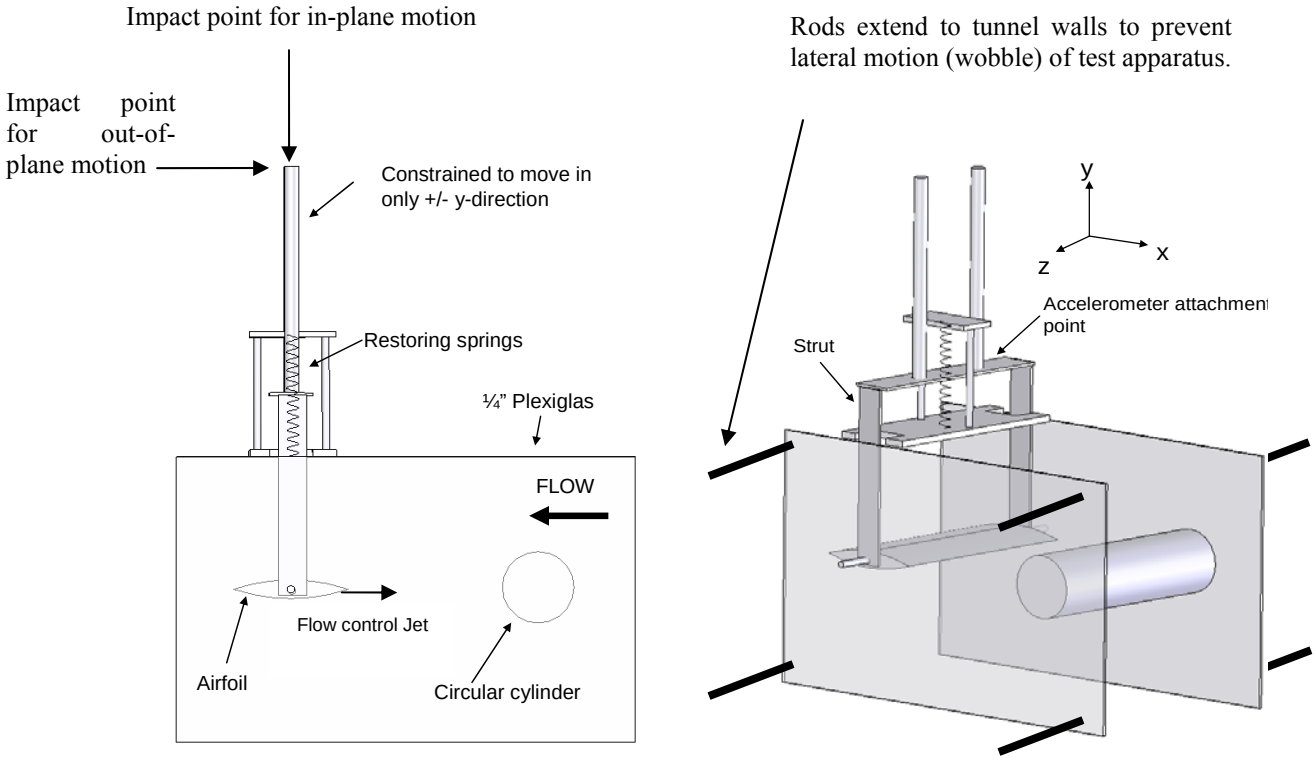

Figure 3.1. Test apparatus setup.

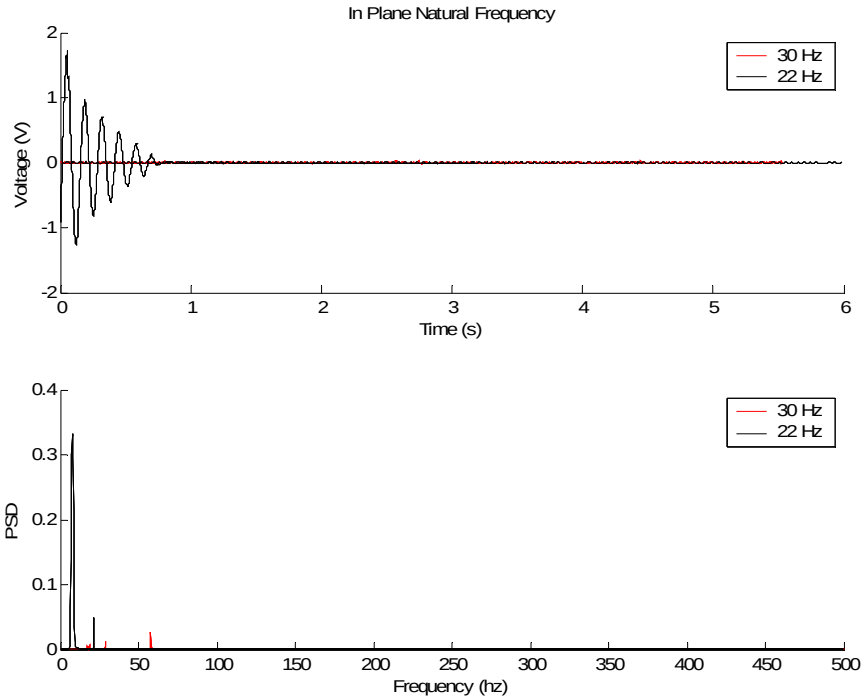

Figure 3.2. In-plane natural frequency.

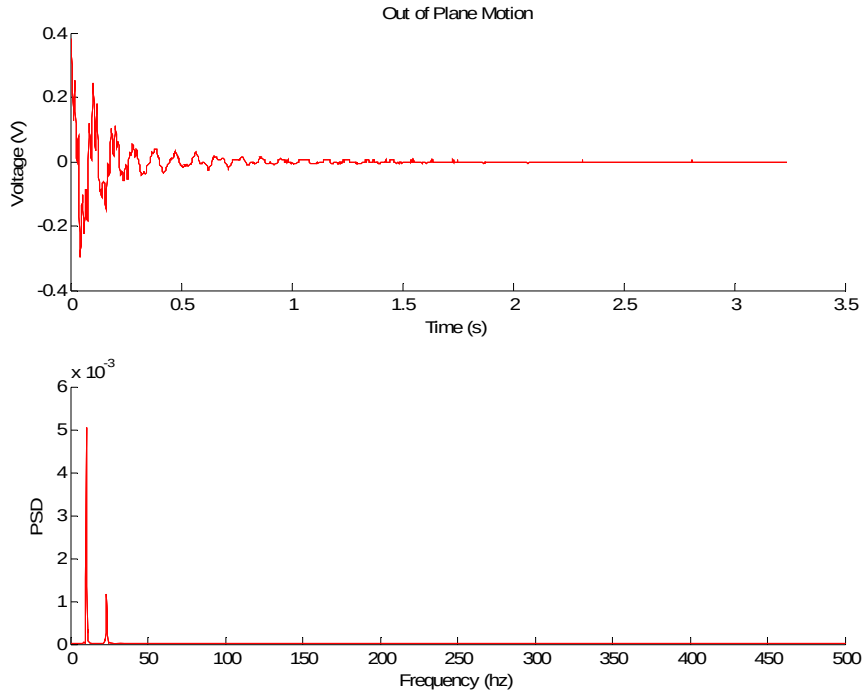

Figure 3.3. Out-of-plane natural frequency.

In order to ensure that the airfoil was not being heavily excited by any naturally occurring mechanism (i.e. shedding from the bluff body of the test apparatus or the state of the incident flow onto the airfoil) while the water tunnel was running, the vibration of the airfoil with no circular cylinder upstream was also recorded. Figure 3.4 shows the output from the power spectral density analysis of both accelerometers. The largest frequency excited is 34 Hz, which corresponds to the rotational frequency of the impeller which drives the

water tunnel flow. The next highest frequency excited is 14 Hz, near the natural frequency of the system. Both of these excitations are far less than those caused by the circular cylinder.

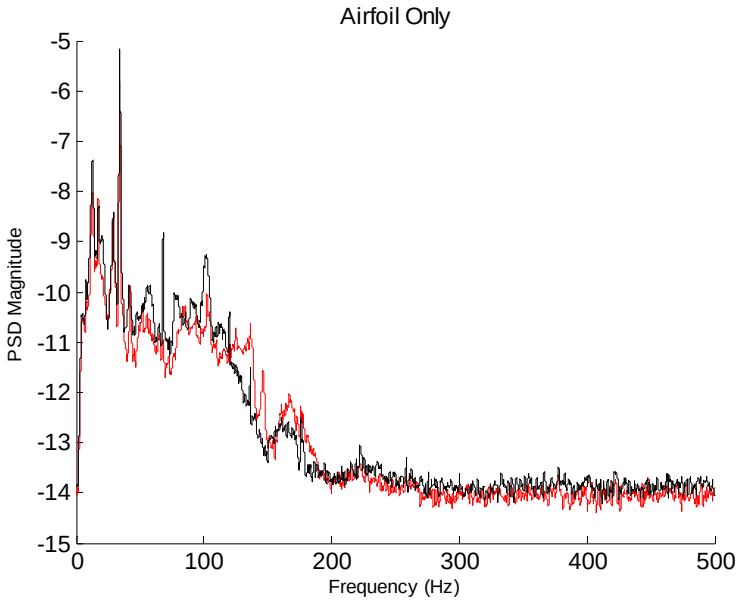

Figure 3.4. Airfoil only vibration response.

4 Appendix II - The Proper Orthogonal Decomposition

The Proper Orthogonal Decomposition (POD) is a method for decomposing a flow field into its fundamental components. POD is useful in that it does not require knowledge of a suitable basis function for the flow field reduction *a priori*; the data is reduced into fundamental modes by mathematically choosing the most efficient basis function for the data reduction. Thus, more flow energy may be captured with fewer modes. The method has been used in the study of jets (Bi et al, 2003 and Shineeb et al, 2006), turbulence (Glegg and Devenport, 2001 and Smith et al, 2005), and a variety of other problems.

Given a velocity ensemble *u*, the POD method seeks an optimal basis function φ such as to maximize the relationship

$$\max \frac{\left\langle (\mathbf{u},\varphi)^2 \right\rangle}{(\varphi,\varphi)} \tag{4.1}$$

Here $(\cdot,\cdot)$ denotes the inner product and $\langle\cdot\rangle$ the ensemble average. By aligning our problem as such, it is apparent that we seek the optimal basis function φ such that the average projection of the velocity field onto this basis function will be maximized, and thus the maximum average kinetic energy fraction will be obtained by the resulting eigenmodes φ. The solution to this problem is given by the calculus of variations; the maximum value of $\left\langle (u,\varphi)^2 \right\rangle$ is sought subject to the constraint that $(\varphi,\varphi)=1$. The complete problem is not formulated here; details may be found in Holmes et al, 1996.

The optimal basis functions can be obtained by solving the Fredholm equation of the second kind (Smith et al, 2005)

$$\int \mathbf{R}(\mathbf{x},\mathbf{x}')\varphi(\mathbf{x}')d\mathbf{x}' = \lambda\varphi(\mathbf{x}) \tag{4.2}$$

Where the kernel of the previous equation is given by the autocorrelation tensor averaged over the sampled data

$$\mathbf{R}(\mathbf{x},\mathbf{x}') = \left\langle \mathbf{u}(\mathbf{x}) \otimes \mathbf{u}*(\mathbf{x}') \right\rangle \tag{4.3}$$

Here $\otimes$ is the tensor product and $*$ denotes the complex conjugate. Note that here $\mathbf{x}=(x,y,z)$. Thus, the solution results in a series of uncorrelated orthogonal functions, given by the solution of Equation 2.2. Note that there are several methods by which the ensemble average of the kernel **R** is calculated, and as such different orthogonal decompositions will result (Braud et al, 2004). The classical method, given by Equation 2.3, utilizes the assumption of ergodicity in a statistically stationary flow. The ensemble average is given as a temporal average, where *R* is a two-point space correlation tensor. **R** may also be calculated using a spatial average (the method of snapshots). **R** is then a two point time correlation tensor (Braud et al, 2004). However, for the same discrete set of finite data, both approaches are equivalent (Sirovich, 1987), and thus the choice of which method to use becomes a matter of practicality, i.e. which method will result in the least number of calculations. In most situations, the method of snapshots is more computationally efficient, as the number of spatially sampled grid points is much greater than the number of points sampled in time. The POD method used in the reduction of the data presented herein utilized the method of snapshots, as is typical for spatially data rich fields such as given by computational fluid dynamics or DPIV studies.

Discretization and solution of Equation 2.2 is given in Smith et al, 2005 and is summarized here for completeness. If we allow

$$c_i = \int_\Omega u^*_{(j)}(x')\varphi(x')dx' \tag{4.4}$$

where Ω is the domain, then we can write Equation 2.2 as

$$\frac{1}{n_t}\sum_{j=1}^{n_t} c_j u_{(j)}(x) = \lambda\varphi(x) \tag{4.5}$$

where Equation 2.5 describes the eigenfunctions as linear combinations of each data snapshot in time. Multiplying Equation 2.5 by $u^*_{(i)}$ and integrating yields

$$\frac{1}{n_t}\sum_{j=1}^{n_t} c_j \int_\Omega u^*_{(i)}(x)u_{(j)}(x)dx = \lambda\int_\Omega u^*_{(i)}(x)\varphi(x)dx \tag{4.6}$$

Substitution of Equation 2.4 into 2.6 yields, in matrix form

$$\begin{bmatrix} a_{11} & \dots & a_{1n_t} \\ \vdots & \ddots & \vdots \\ a_{n_t 1} & \dots & a_{n_t n_t} \end{bmatrix}\begin{bmatrix} c_1 \\ \vdots \\ c_{n_t} \end{bmatrix} = \lambda\begin{bmatrix} c_1 \\ \vdots \\ c_{n_t} \end{bmatrix} \tag{4.7}$$

Where

$$a_{ij} = \int_\Omega u^*_{(i)}(x)u_{(j)}(x)dx \tag{4.8}$$

As was shown in Equation 2.5, the linear contributions of the eigenvectors $\mathbf{c}^n = \begin{bmatrix} c_1^n & \cdots & c_{n_t}^n \end{bmatrix}^T$ and eigenvalues λ^n given by Equation 2.7 can be used to solve for the eigenfunctions of the original problem, φ, as given in Equation 2.9.

$$\varphi^n(x) = \frac{1}{\lambda^{(n)} n_t}\sum_{j=1}^{n_t} c_j^n u_{(j)}(x) = \frac{1}{\lambda^{(n)} n_t}\begin{bmatrix} c_1^n & \cdots & c_{n_t}^n \end{bmatrix}\begin{bmatrix} u_{(1)}(x) \\ \vdots \\ u_{(n_t)}(x) \end{bmatrix} \tag{4.9}$$

The matrix formulation of Equation 2.9 is given as

$$\begin{bmatrix} \varphi_{n_x}^{(1)} & \cdots & \varphi_{n_x}^{(1)} \\ \vdots & \ddots & \vdots \\ \varphi_1^{(n_t)} & \cdots & \varphi_{n_x}^{(n_t)} \end{bmatrix} = \frac{1}{n_t}\begin{bmatrix} \frac{c_1^1}{\lambda^{(1)}} & \cdots & \frac{c_{n_t}^1}{\lambda^{(1)}} \\ \vdots & \ddots & \vdots \\ \frac{c_1^{n_t}}{\lambda^{(n_t)}} & \cdots & \frac{c_{n_t}^{n_t}}{\lambda^{(n_t)}} \end{bmatrix}\begin{bmatrix} u_{(1)}^1 & \cdots & u_{(1)}^{n_x} \\ \vdots & \ddots & \vdots \\ u_{(n_t)}^1 & \cdots & u_{(n_t)}^{n_x} \end{bmatrix} \tag{4.10}$$

Note that the problem has reduced to a $(n_t \; x \; n_t)$ problem, as opposed to a $(n_x \; x \; n_x)$ problem. In the current DPIV problem, 18369 flow vectors were measured in each flow field, as opposed to 3474 time steps. Thus the method of snapshots is indeed more computationally efficient. Note that the numerical integrations require multiplication by an appropriate weight function depending on which quadrature method is used, such as the trapezoidal rule or Simpson's rule.

The eigenvalue problem yields a series of eigenmodes and eigenfunctions which can be used to reconstruct the original velocity field by linearly superimposing the individual modes as in Equation 2.11

$$\mathbf{u}(\mathbf{x},t) = \sum_{i=1}^{N} a_i(t)\varphi_i(\mathbf{x}) \tag{4.11}$$

Eigenfunctions corresponding to large eigenmodes are the primary flow modes, and thus POD is appealing as a method for the identification of coherent structures. That is, as the total flow energy is the summation of all modes' contributions, those modes with the large eigenmodes will dominate the flow field. The contribution of an individual eigenmode to the overall energy of the flow may be described as

$$Energy\ Fraction = \frac{\lambda_i}{\sum_{j=1}^{\infty} \lambda_j} \quad \textbf{4.12}$$

Since φ is dimensionless and by Equation 2.3 $\mathbf{R}(\mathbf{x}, \mathbf{x}')$ must have dimensions of meters^2 per second^2, and thus λ also has dimensions of specific energy (i.e. mass normalized). Thus the dominant structures of the flow may be categorized by the specific energy of the individual mode, the larger eigenvalues corresponding to more energetic modes contained in the flow.

Bi, W., Sugii, Y., Okamoto, K., and Madarame, H. "Time-resolved proper orthogonal decomposition of the near-field flow of a round jet measured by dynamic particle image velocimetry." Measurement Science and Technology, Vol. 14, 2003, L1-L5.

Glegg, S. and Devenport, W. "Proper Orthogonal Decomposition of Turbulent Flows for Aeroacoustic and Hydroacoustic Applications," Journal of Sound and Vibration, Vol. 239, No. 4, 2001, pp 767-784.

Holmes, P., Lumley, J., and Berkooz, G. *Turbulence*, *Coherent Structures*, *Dynamical Systems and Symmetry*, Cambridge University Press, Cambridge, UK, 1996.

Shineeb, A., Balachandar, R., and Bugg, J. "Quantitative Investigation of Coherent Structures in a Free Jet using PIV and POD," Presented at the 2006 ASME Joint U.S.-European Fluids Engineering Summer Meeting, Miami, FL, July 17-20.

Sirovich, L. "Turbulence and the dynamics of coherent structures. 1: Coherent structures." Q Appl Math, Vol. 45, 1987, pp 561-571.

Smith, T., Moehlis, J., and Holmes, P. "Low-Dimensional Modelling of Turbulence Using the Proper Orthogonal Decomposition: A Tutorial," Nonlinear Dynamics, Vol. 41, 2005, pp 273-307.

5 Appendix III – Additional Proper Orthogonal Decomposition Results

At the time of the defense, the Proper Orthogonal Decomposition (POD) had just been utilized to decompose and analyze the dynamics of the Leading Edge Blowing (LEB) jet and the circular cylinder wake. The plots and discussion contained herein supplements that shown in the previous chapters. The data presented here is the result of the POD analysis of the same data shown previously.

5.1 ADDITIONAL MODE SHAPES AND PROJECTION COEFFICIENT ANALYSIS FOR CASE 2 – MEAN FLOW FIELD SUBTRACTED

POD was used to characterize this change in the flow field by analyzing how the fundamental (most energetic) mode shapes changed with the addition of LEB. The energy contained in the POD modes is shown in Figure 5.1 **Error! Reference source not found.**and Figure 5.2. Except for C_μ=0.14, there is a clear trend of descending energy contained in the first mode. This trend is also seen in the second mode, which together compromise 40-50% of the total flow energy, depending on the degree of LEB. What should be noticed is that in the case of high degrees of LEB, more eigenmodes are required to capture a large degree of the flow energy. For example, for C_μ=0, it takes 127 modes to capture 90% of the total flow energy. For C_μ=0.14 it takes 136 modes to capture the same amount of flow energy. For C_μ=0.21 it takes 163 modes to capture 90% of the total flow energy. One of the interesting points of this analysis is theorizing why it takes more eigenmodes to capture the same amount of flow energy and why the two fundamental eigenmodes for C_μ=0 contain much more energy than when compared to the LEB cases. The answer is that POD is extremely effective at determining coherent structures in a flow field. In the case of a highly organized flow field, such as that given by a von Karman vortex street, the fundamental modes of the flow field are quite clear (an array of vortices). As the flow becomes less organized, more modes are required to describe the flow field. Thus, we may surmise that the trend of less energetic modes for the LEB cases is due to the LEB jet colliding with and breaking up the coherency of the flow structures (the vortices).

For the C_μ=0.05 case, the previously described trend does not hold. At 4 modes, eigenmodes become much more energetic than all others. The reason for this divergence is not clear; although it appears that the jet may help to organize the flow in such a manner as to promote oscillations at the natural frequency of the airfoil, which are markedly increased for this test case when compared to the others.

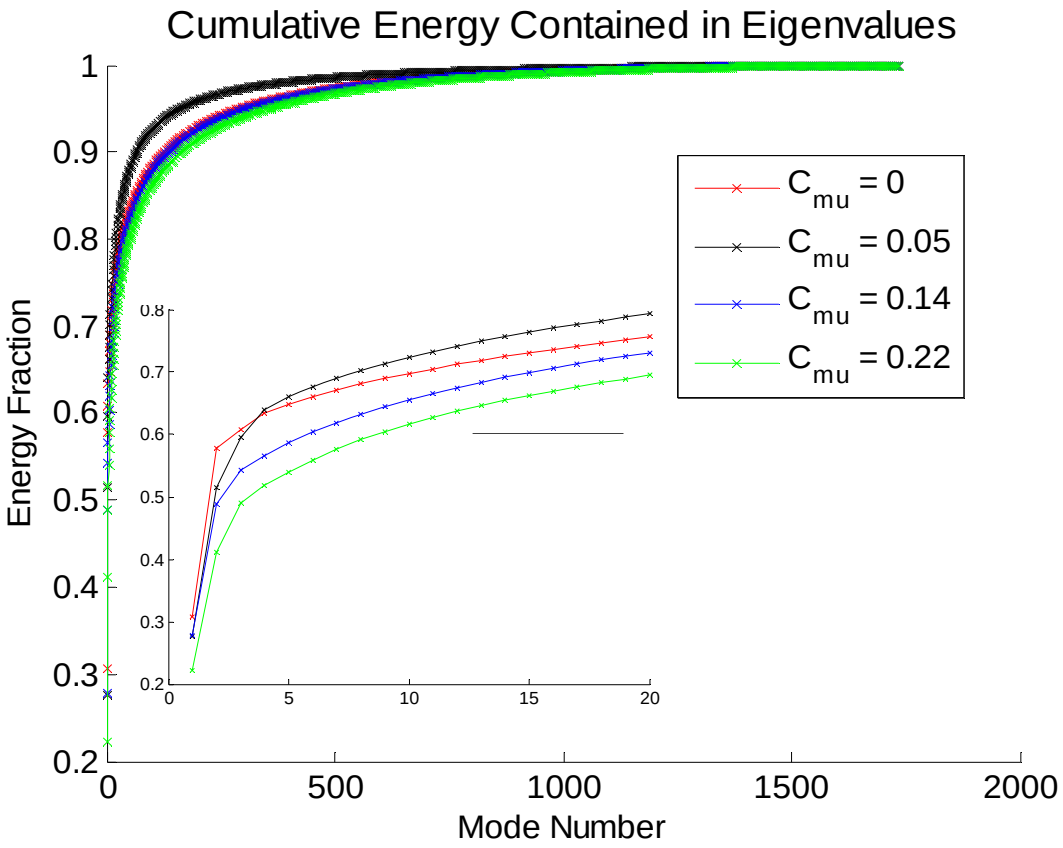

Figure 5.1 Cumulative energy distribution from the POD modes.

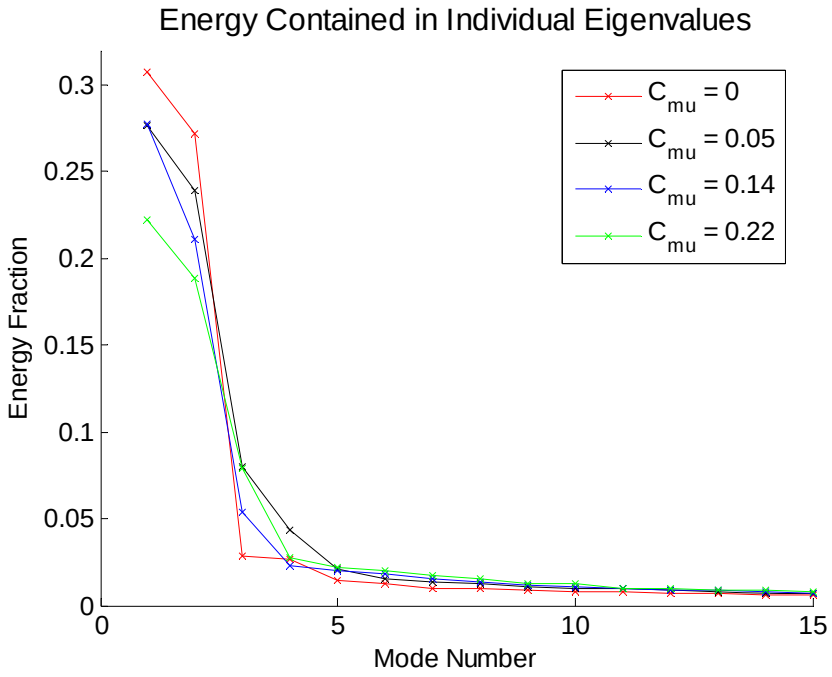

Figure 5.2. Energy distribution of individual modes.

Using the POD method, we can reconstruct any given number of modes into a representative flow field. If many modes are used, for example if enough modes are used to capture 90% of the total flow energy, the resulting solution will approximate the original flow field. In fact, we may use the POD method to remove significantly bad vectors from the DPIV data, since the flow field modes corresponding to these vectors will be of very low energy. In this manner, the POD can operate as a spatio-temporal filter to the DPIV data. Care must be taken in using this approach however, as turbulent flow contributing a small percentage to the overall flow energy could be misinterpreted and thus filtered. As most of the interesting dynamics for this experiment occur for the large vortical structures which dominate the flow field, this concern is less applicable here.

Since the POD modes represent the flow structures organized by their energy contribution to the total flow, it is logical to compare the most energetic modes for the blowing and no-blowing cases for clues as to the interaction mechanism responsible for the reduction in BVI. A comparison between the first six modes for the no-blowing (about 65% total energy) and maximum blowing (about 55% total energy) cases are shown below. Comparing the first mode of the no-blowing and maximum blowing cases yields an interesting flow structure change at the tip of the airfoil leading edge. For the no-blowing case a well defined vortex exists just below of the airfoil leading edge, whereas in the maximum blowing case a skewed vortex exists below the airfoil leading edge but it is displaced further away. The second mode for the LEB case shows vortices directly under the airfoil surface as displaced further away than when compared to the no-blowing case. The third mode is a convection mode; this mode is responsible for giving motion to the vortices (whose structure is given in the first two modes). Note that the direction of the flow vectors in the mode shapes is arbitrary; this fact will become apparent when viewing the projection coefficient (PC) evolution in time. Thus, the fourth mode for the maximum blowing case shows the influence of the LEB jet in creating a "buffer zone" around the airfoil.

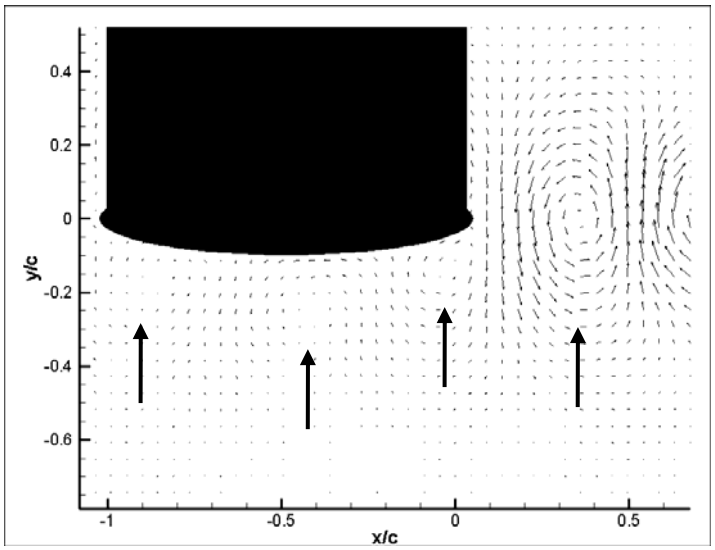

Figure 5.3. No-blowing case, mode 1.

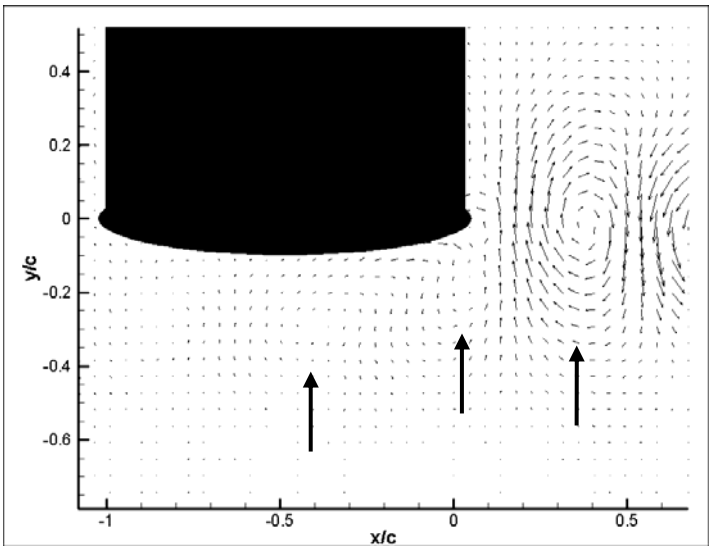

Figure 5.4. Max-blowing case, mode 1.

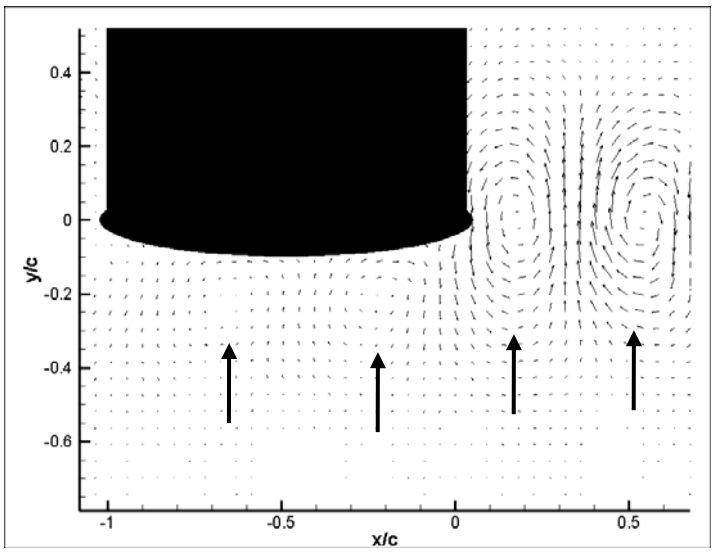

Figure 5.5. No-blowing case, mode 2.

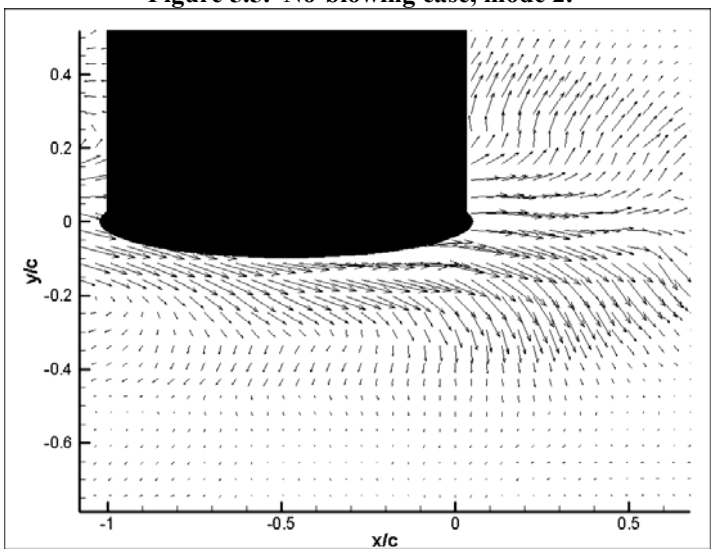

Figure 5.6. No-blowing case, mode 3.

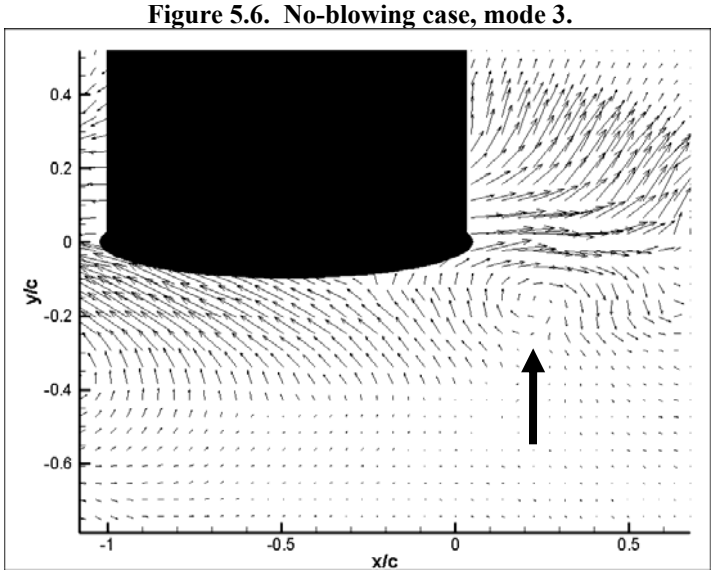

Figure 5.7. No-blowing case, mode 4.

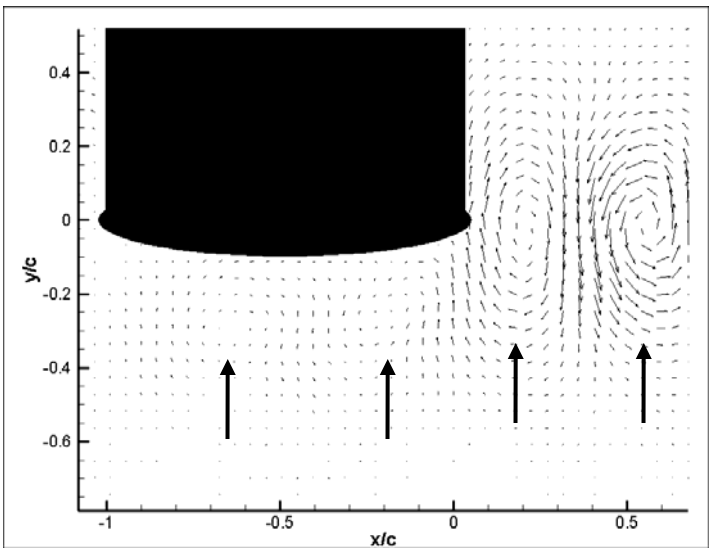

Figure 5.8. Max-blowing case, mode 2.

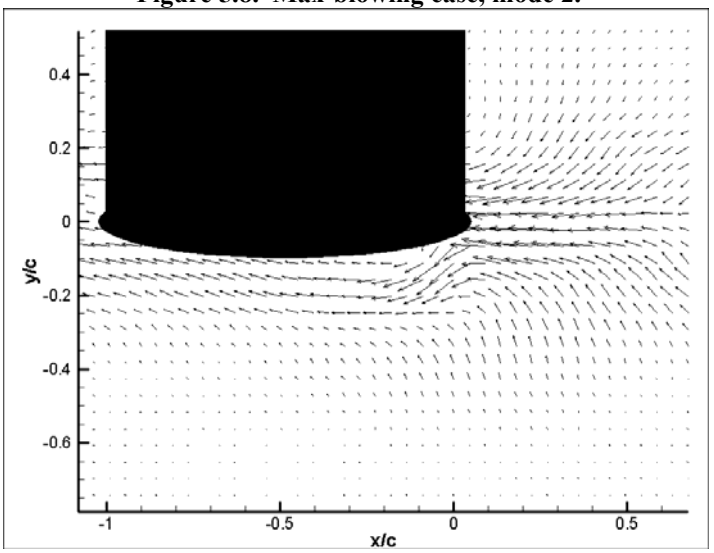

Figure 5.9. Max-blowing case, mode 3.

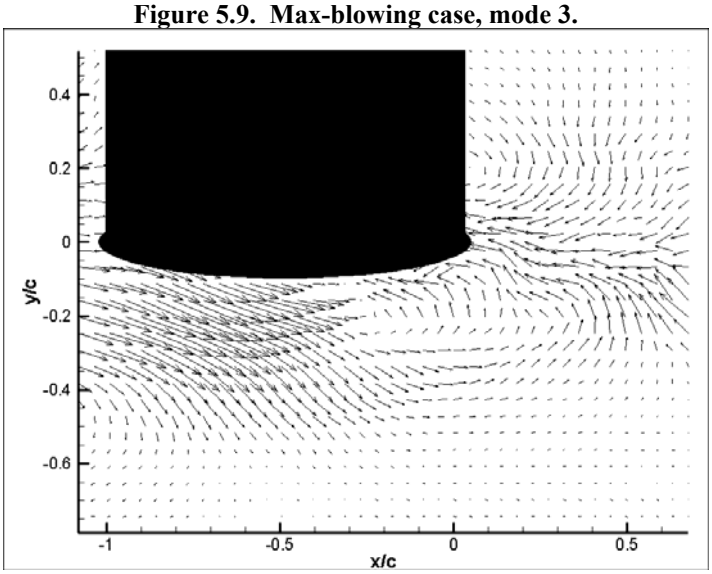

Figure 5.10. Max-blowing case, mode 4.

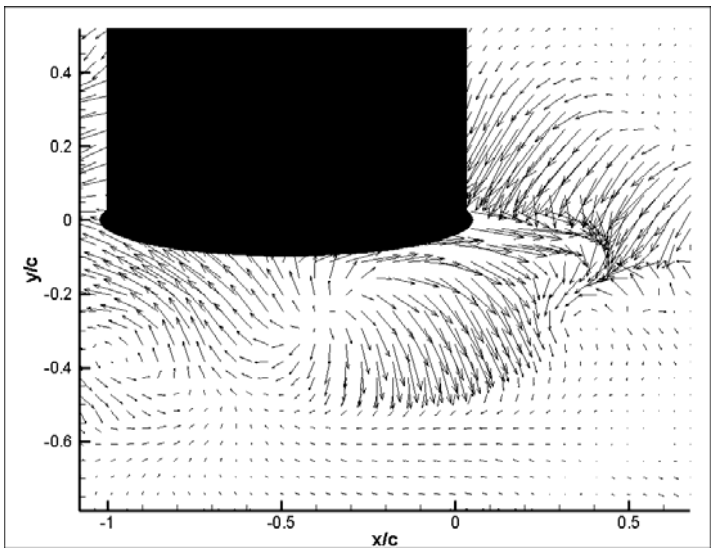

Figure 5.11. No-blowing case, mode 5.

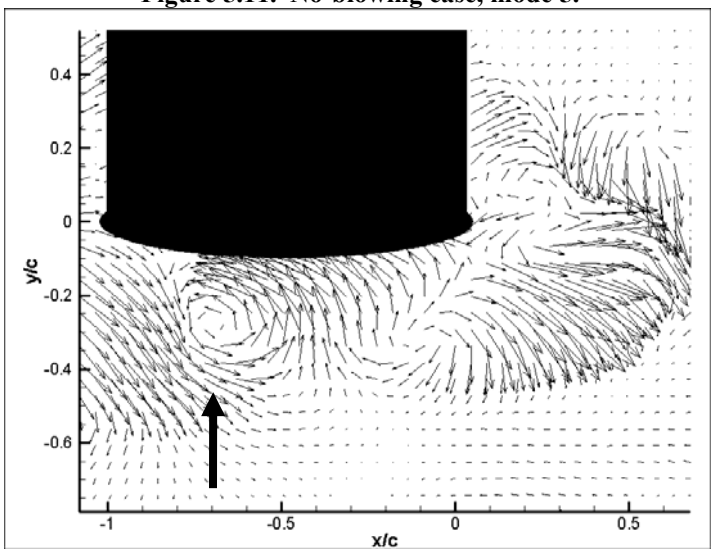

Figure 5.12. No-blowing case, mode 6.

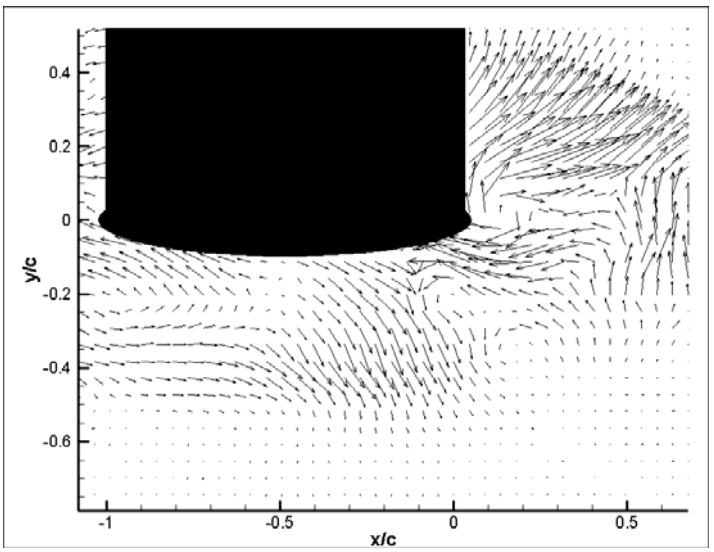

Figure 5.13. Max-blowing case, mode 5.

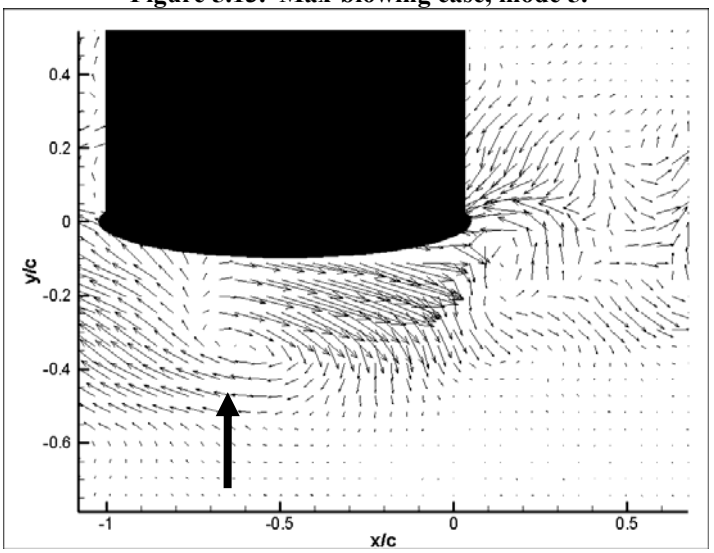

Figure 5.14. Max-blowing case, mode 6.

The projection coefficients (PC) for the first six modes were analyzed to ascertain what each mode physically corresponds to. These are shown in Figure 5.15 – Figure 5.26. The five largest spectra components are noted on the Figures. Note that the magnitude of the PC fluctuates in intensity and sign; the linear superposition of each mode shape with their time-varying PC ensures a proper reconstruction of the original flow field. Thus, the direction of the flow field vectors in the static mode shapes is arbitrary. For each mode, both the PC and the Power Spectral Density (PSD) is shown. For both the no-blowing and maximum blowing cases, the first and second modes correspond to the shedding frequency of the circular cylinder (about 5.9 Hz). This is apparent from the PSD of the PC. The third mode is very low frequency in both cases (less than 0.7 Hz), which indicates an almost steady-state mode shape. This agrees with the qualitative assessment of the third mode shape as a vortex convection mode. While a comparison between the blowing cases of the first three modes agreed relatively well, a divergence is seen for the fourth through the sixth modes. A comparison of the changes in the power of the airfoil vibration for the maximum blowing case shows a sharp increase around approximately 2-3 Hz for the maximum blowing case; this spectral characteristic is also shown in a comparison of the fourth, fifth, and sixth modes, which reflect changes in the flow field dynamics. It is interesting to note

the major spectral difference in the fifth mode for the two blowing cases. For this mode with LEB, the major flow field characteristic is occurring at almost exactly one-half that seen in the case of no-blowing. Note that the POD results show that the vortex shedding is still taking place at the regular shedding frequency, which implies that the LEB jet is not having an effect on the circular cylinder shedding mechanisms.

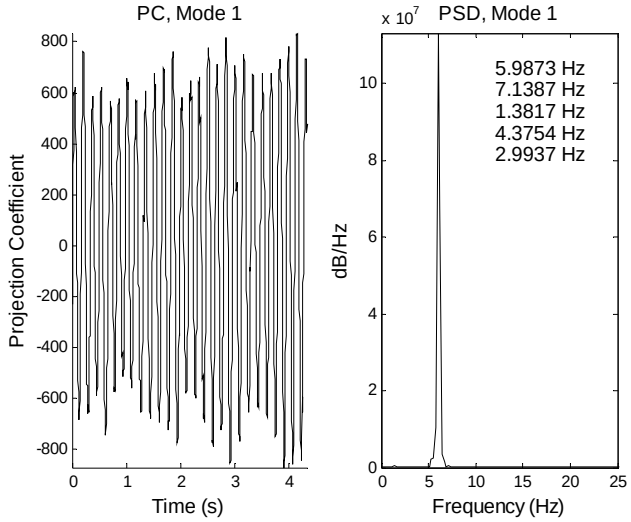

Figure 5.15. No-blowing case, mode 1 projection coefficient.

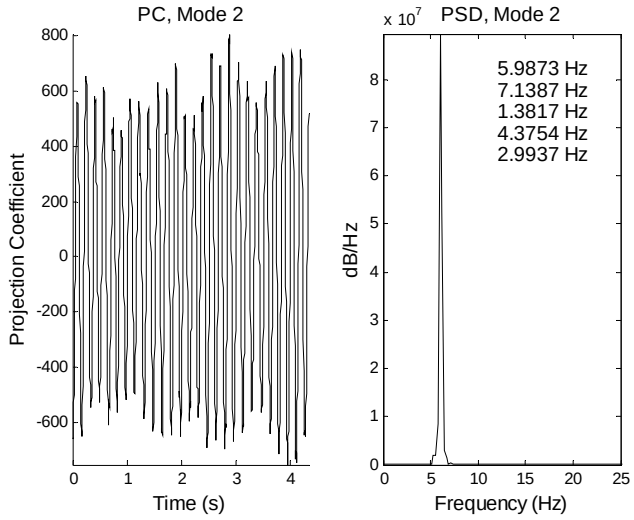

Figure 5.16. No-blowing case, mode 2 projection coefficient.

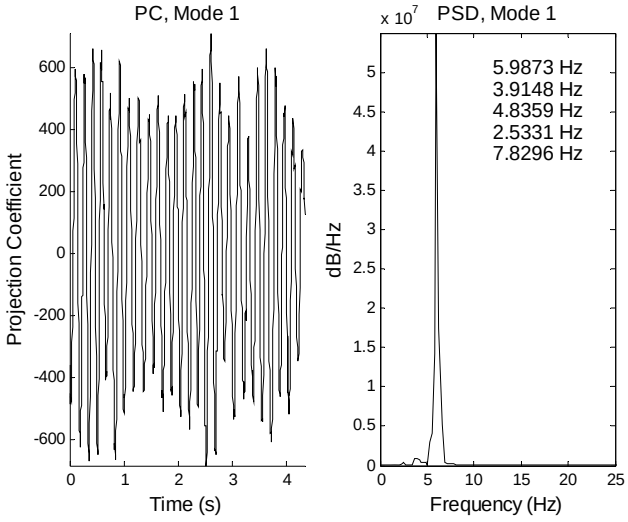

Figure 5.17. Max-blowing case, mode 1 projection coefficient.

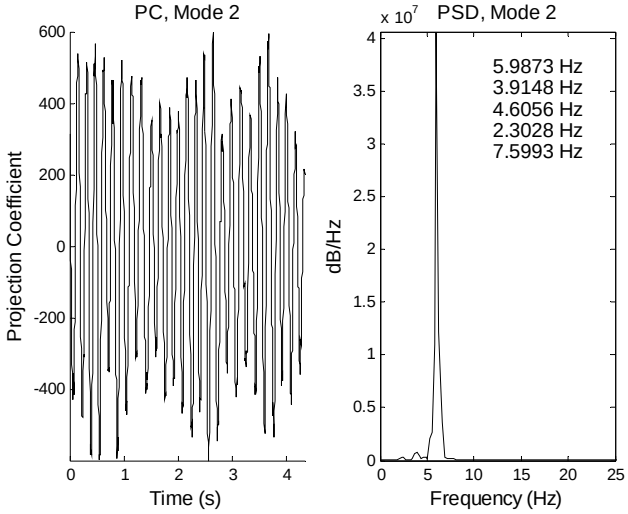

Figure 5.18. Max-blowing case, mode 2 projection coefficient.

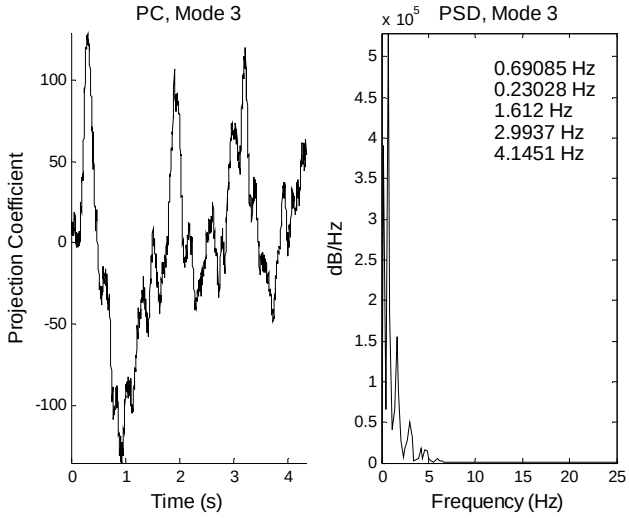

Figure 5.19. No-blowing case, mode 3 projection coefficient.

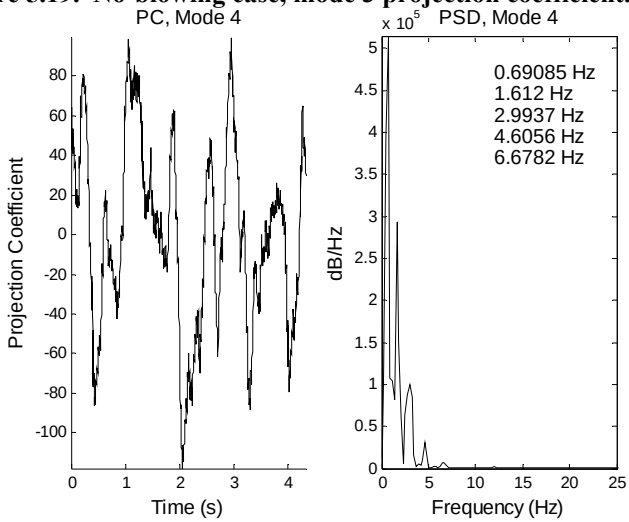

Figure 5.20. No-blowing case, mode 4 projection coefficient.

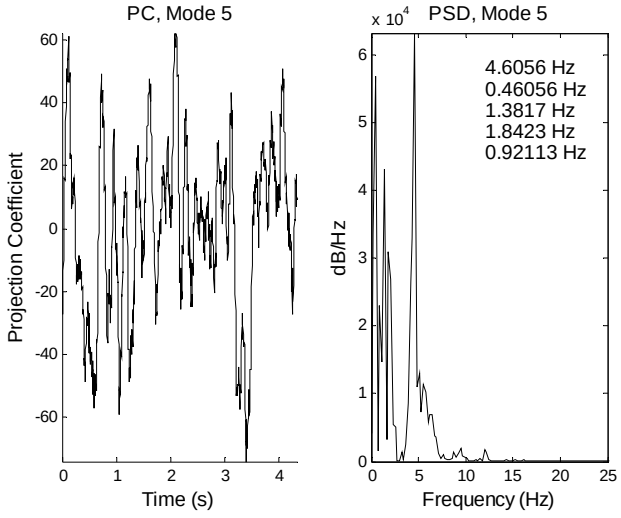

Figure 5.21. No-blowing case, mode 5 projection coefficient.

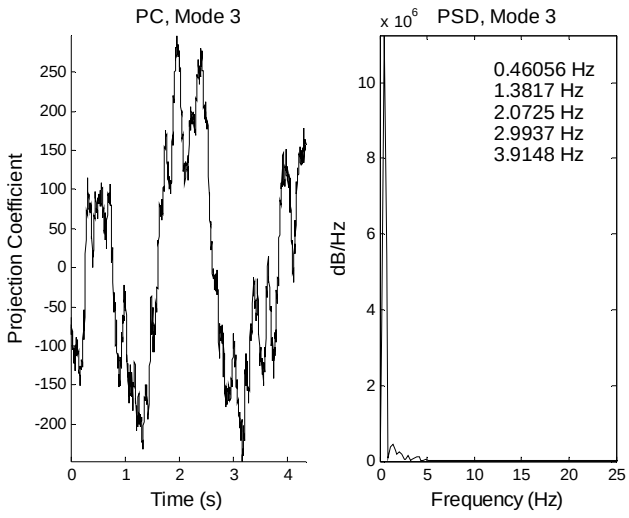

Figure 5.22. Max-blowing case, mode 3 projection coefficient.

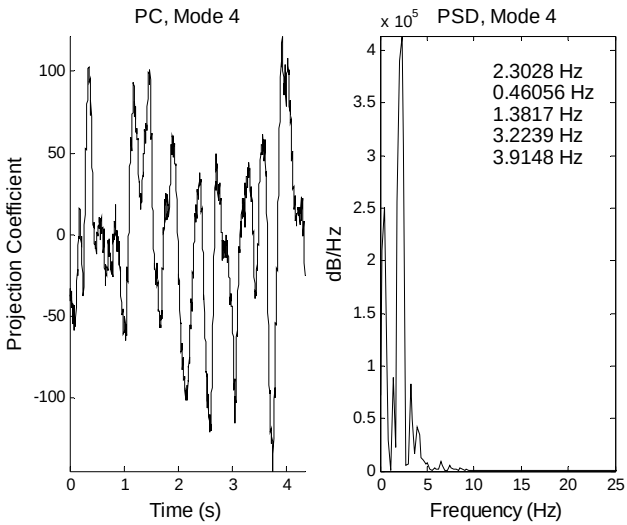

Figure 5.23. Max-blowing case, mode 4 projection coefficient.

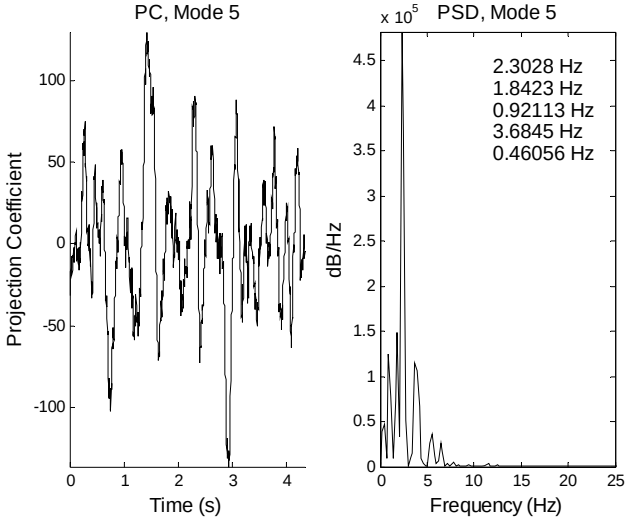

Figure 5.24. Max-blowing case, mode 5 projection coefficient.

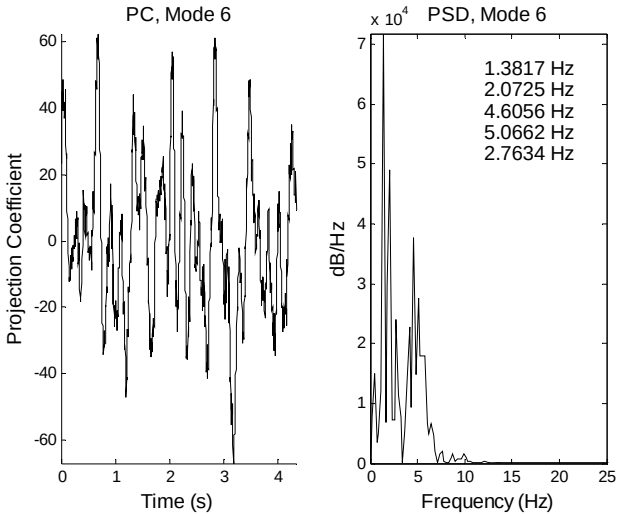

Figure 5.25. No-blowing case, mode 6 projection coefficient.

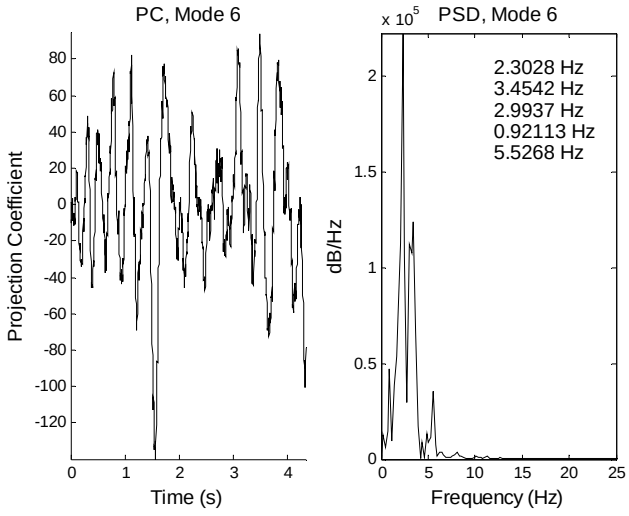

Figure 5.26. Max-blowing case, mode 6 projection coefficient.

A dynamic plot of the flow field for the experimental data compared to the reconstructed POD data field is shown in Figure 5.27 – Figure 5.32. The POD reconstruction uses 160 modes to capture 90% of the total flow energy. Both of the image sets agree quite well. It should also be noticed that some bad vectors are removed in the POD reconstructed solution without sacrificing the integrity of the original data set.

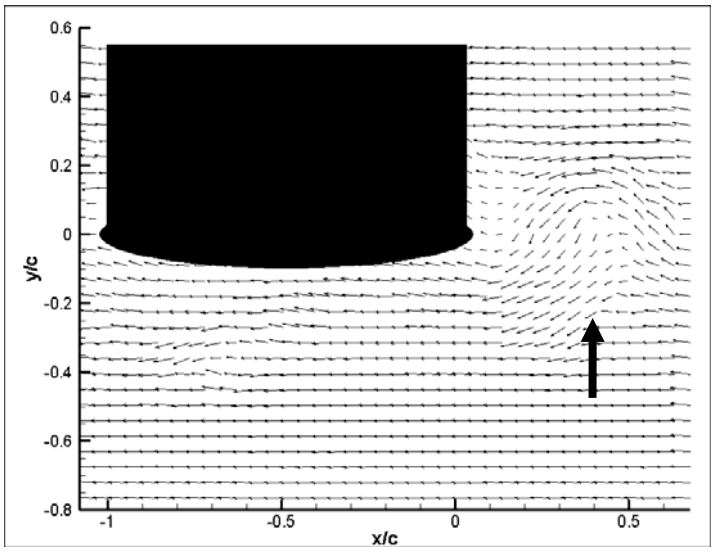

Figure 5.27. Experimental flow vectors, t=0s.

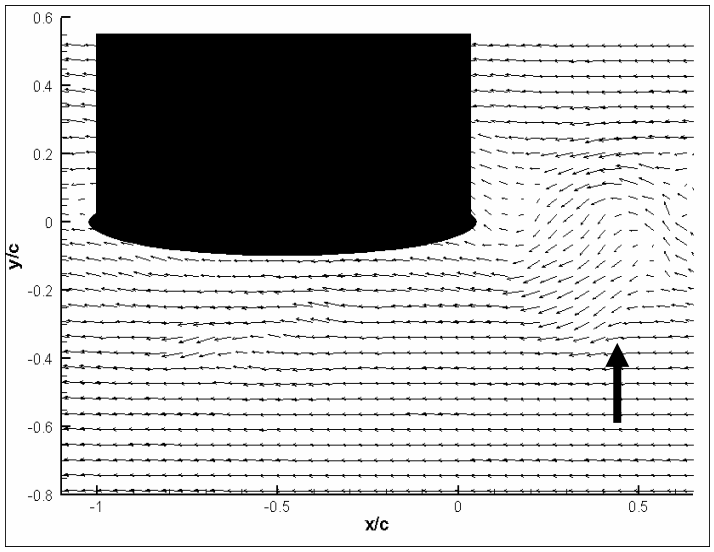

Figure 5.28. POD reconstructed flow vectors, t=0s.

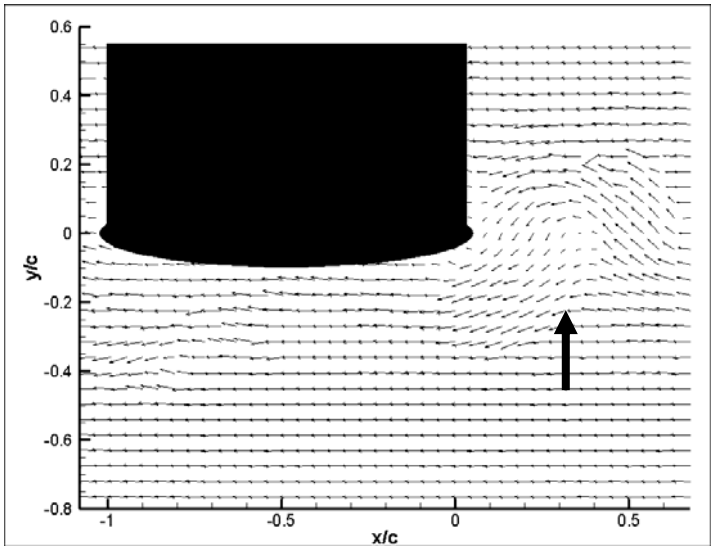

Figure 5.29. Experimental flow vectors, t=0.30s.

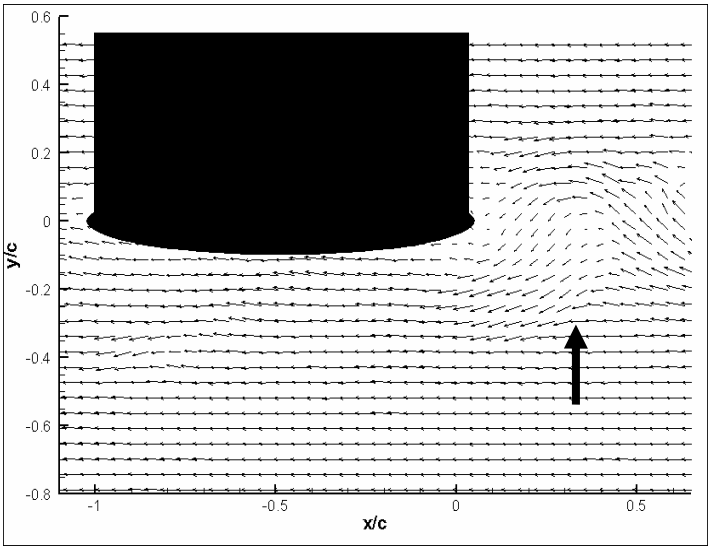

Figure 5.31. POD reconstructed flow vectors, t=0.3s.

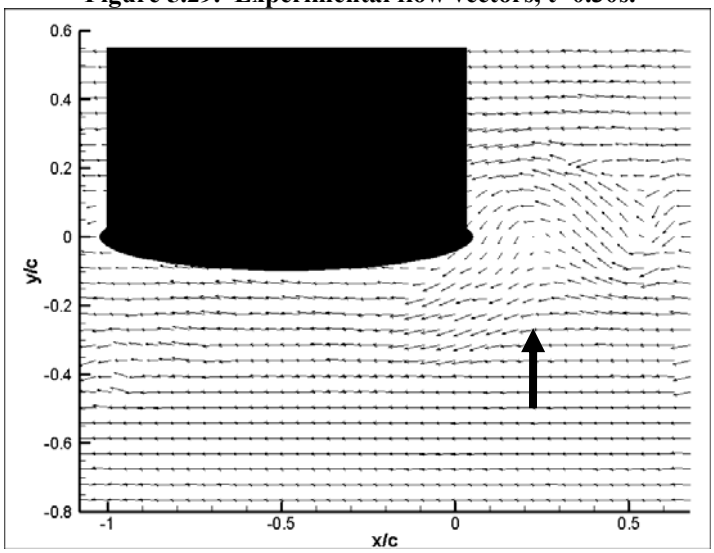

Figure 5.30. Experimental flow vectors, t=0.60s.

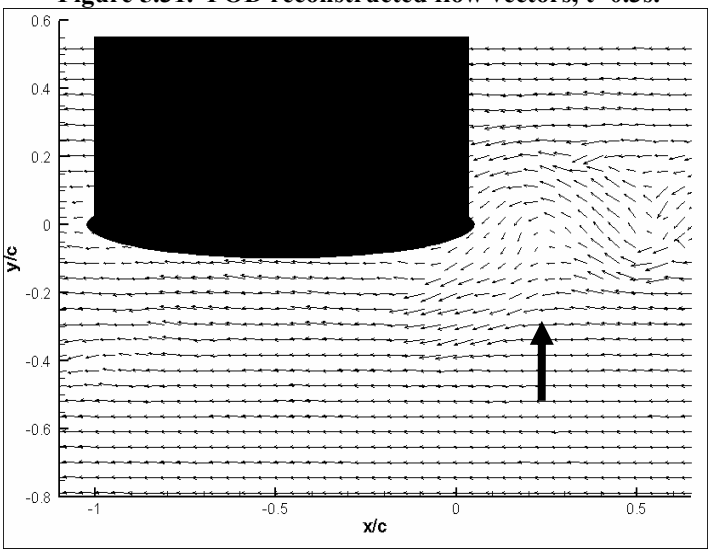

Figure 5.32. POD reconstructed flow vectors, t=0.60s.

If only 10 modes are used to reconstruct the velocity field and compare the no-blowing and maximum blowing cases, which comprises 68% and 58% of the total flow energy respectively, the mechanism by which the LEB interacts with the vortex street becomes readily apparent. The LEB jet can affect the vortices in one of two manners: the stand-off distance of the vortex is increased or the vortices are drawn into the centerline of the airfoil and split. Both of these methods reduce the unsteady pressure projection from the vortices onto the airfoil surface in separate ways. Increasing the stand-off distance puts more distance between the vortex and the airfoil surface, thus decreasing the pressure projected onto the blade surface by the vortex. Splitting the vortices into two allows for each part of the vortex to pass over the top and bottom of the airfoil, thus canceling out the pressure projection of the convecting vortices and negating any forcing of the blade surface. Vortices are drawn into the centerline of the airfoil sharp tip by the low pressure LEB jet which penetrates into the wake. A comparison of the POD reconstructed instantaneous flow fields for no-blowing and maximum blowing are shown in Figure 5.33 – Figure 5.38. Vortex positions are marked with vertical arrows. These Figures demonstrate the second mechanism of LEB/vortex street interaction, in which convecting vortices are drawn into the centerline of the airfoil and split in two. For the no-blowing case, the incident vortex passes close to

the airfoil tip but propagates down the entire length of the airfoil. For the maximum blowing case, the vortex is drawn into the airfoil centerline and is split in two as it encounters the leading edge of the airfoil.

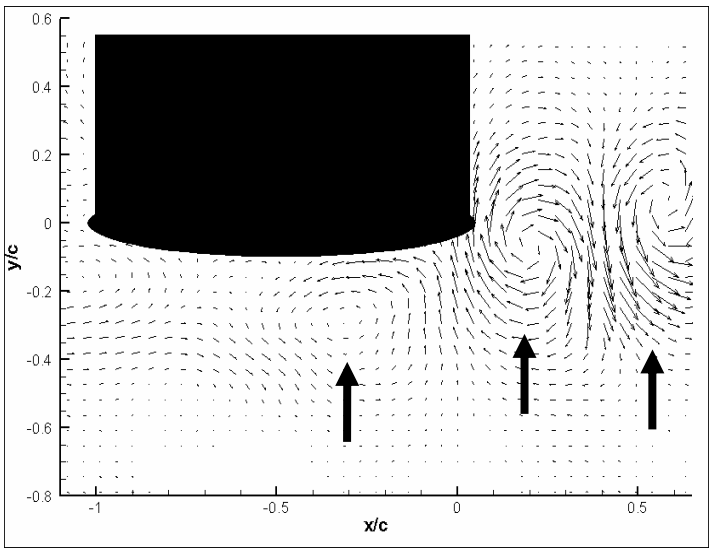

Figure 5.33. POD reconstructed vectors, C_μ=0, t=0s.

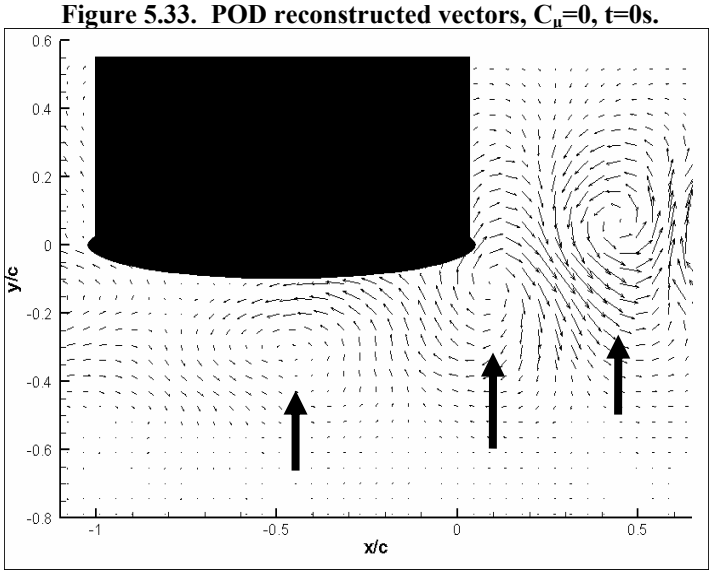

Figure 5.34. POD reconstructed vectors, C_μ=0, t=0.30s.

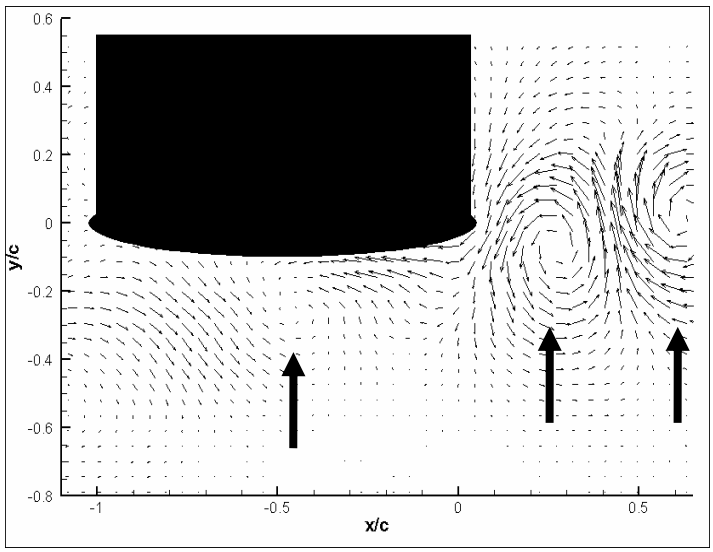

Figure 5.35. POD reconstructed vectors, C_μ=0.21, t=0s.

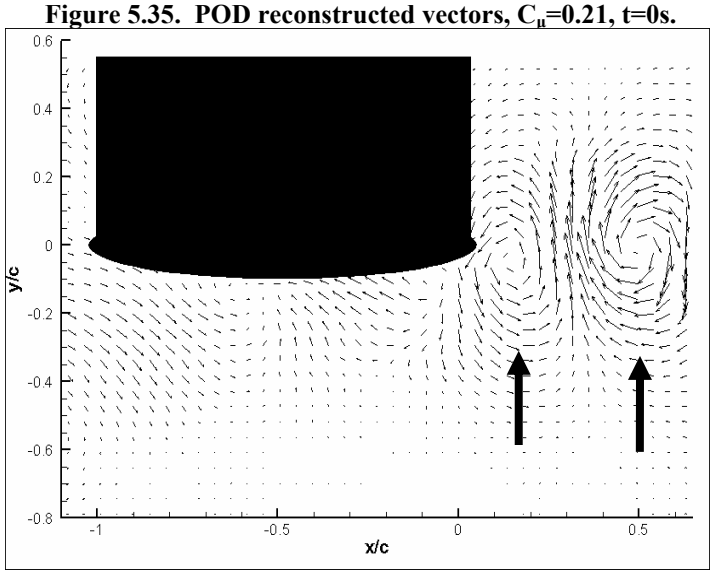

Figure 5.36. POD reconstructed vectors, C_μ=0.21, t=0.30s.

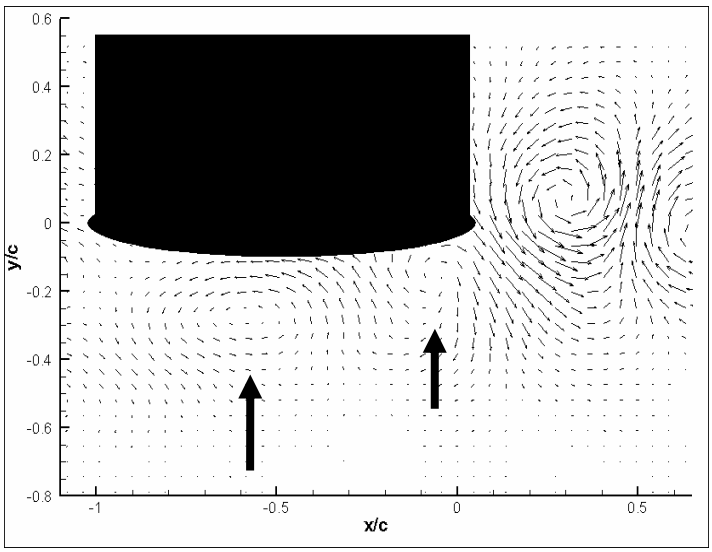

Figure 5.37. POD reconstructed vectors, C_μ=0, t=0.60s.

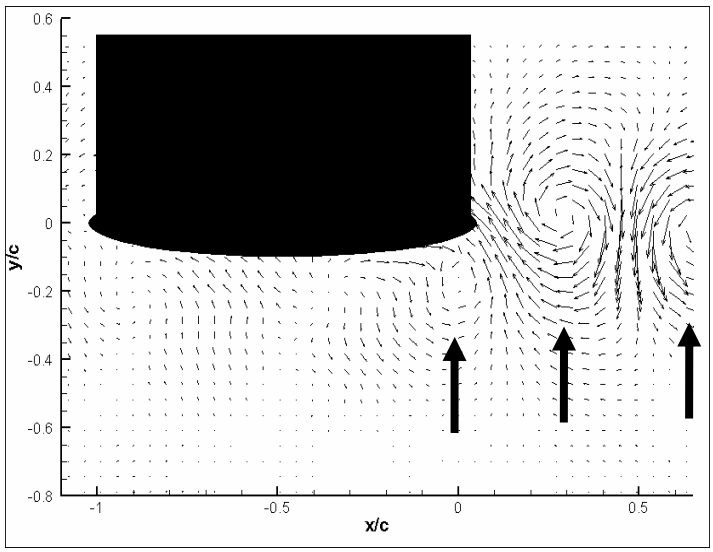

Figure 5.38. POD reconstructed vectors, C_μ=0.21, t=0.60s.

5.2 ADDITIONAL MODE SHAPES AND PROJECTION COEFFICIENT ANALYSIS FOR CASE 2 – MEAN FLOW FIELD INCLUDED

The first six mode shapes for the mean-included POD analysis are shown in Figure 5.40 – Figure 5.51. For both blowing cases, the first mode obviously corresponds to the mean flow field. In the previous POD analysis, this component of the flow-field was subtracted before the decomposition. The mean flow field contributes the bulk of the energy to the flow field; consider Figure 5.39, which shows the cumulative and individual energy distribution for the given modes. For each case, the first mode accounts for at least 95% of the total flow energy. The second and third modes are similar to those from the mean-subtracted POD analysis and show the impinging vortex street. A comparison of the fourth through sixth modes shows significant differences; the influence of the LEB jet on the flow field can be seen in these Figures. An interesting comparison can be made between Figure 5.40 and Figure 5.43, which depicts the mean flow fields. Note that for the maximum blowing case, there is indeed a "buffer zone" created at the leading edge of the airfoil (marked with airfoil).

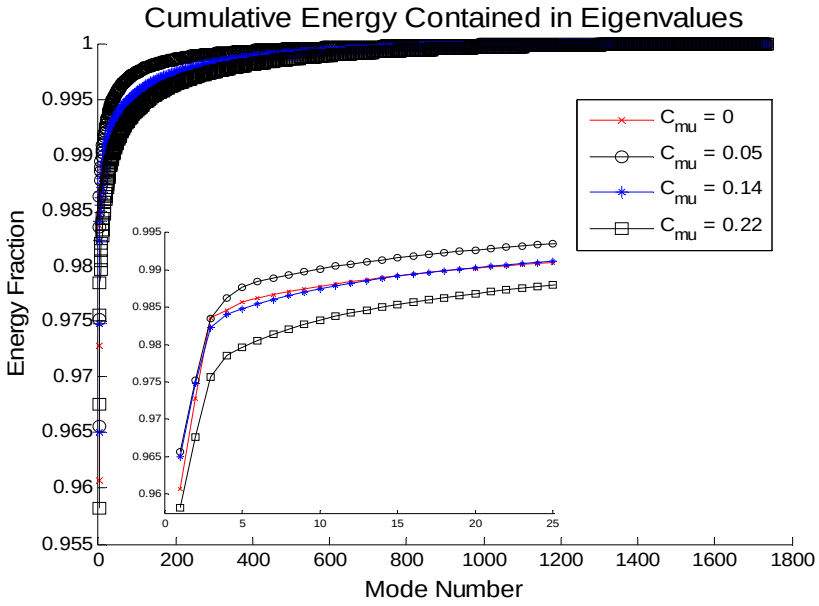

Figure 5.39. Energy contribution of individual modes for case 3, mean flow field included.

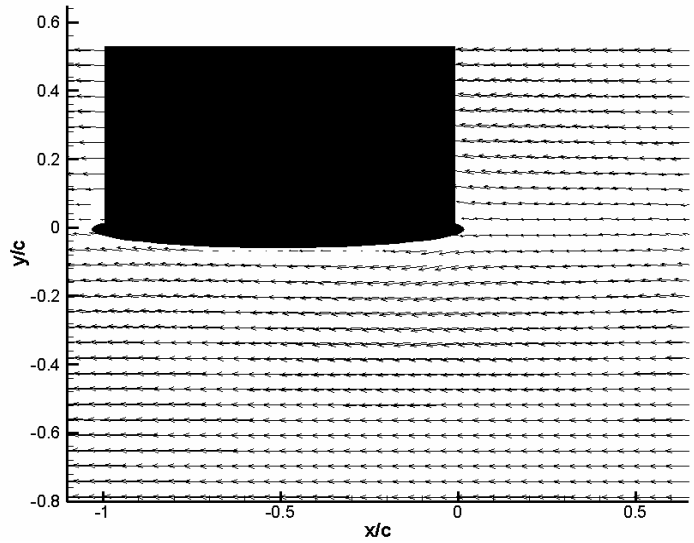

Figure 5.40. No-blowing case, mode 1.

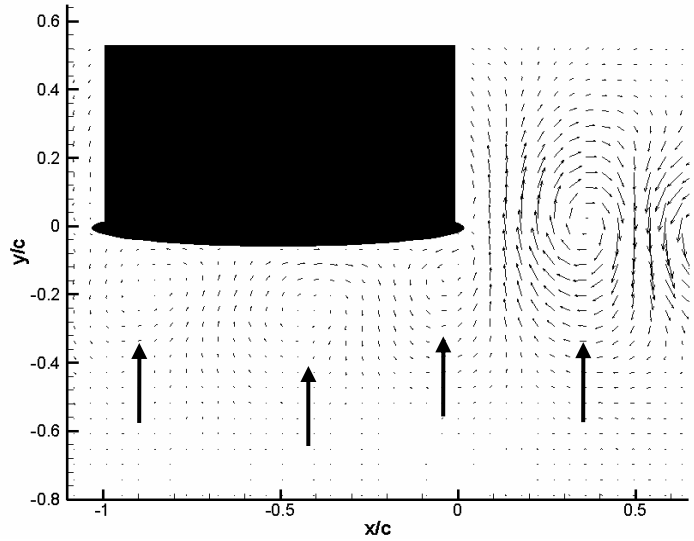

Figure 5.41. No-blowing case, mode 2.

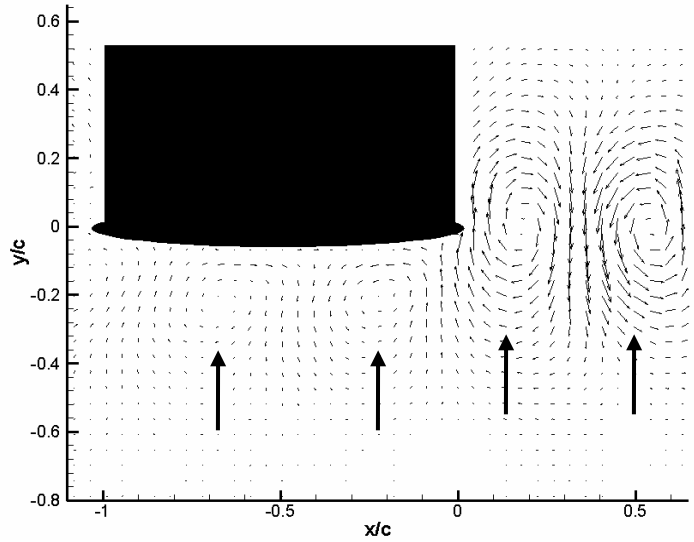

Figure 5.42. No-blowing case, mode 3.

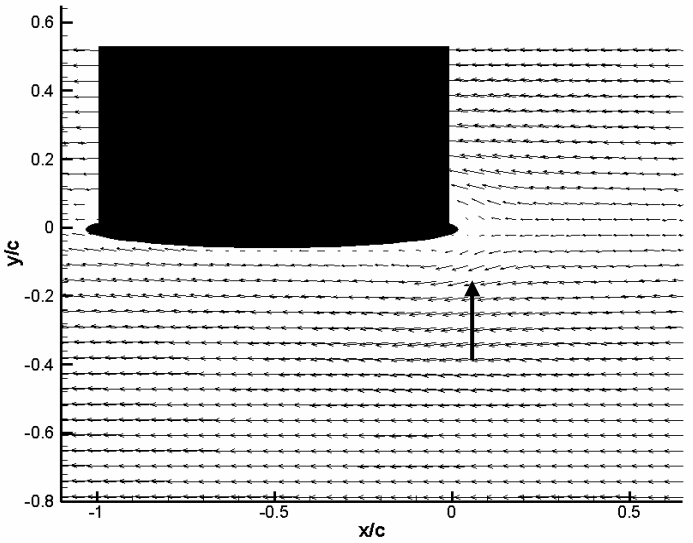

Figure 5.43. Max-blowing case, mode 1.

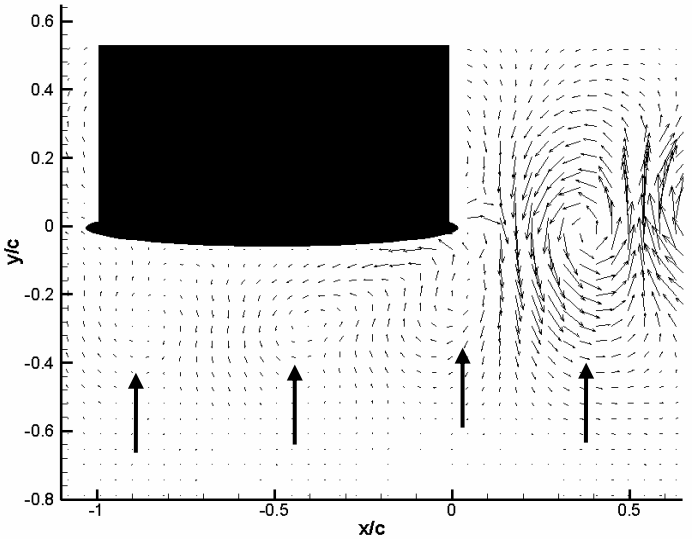

Figure 5.44. Max-blowing case, mode 2.

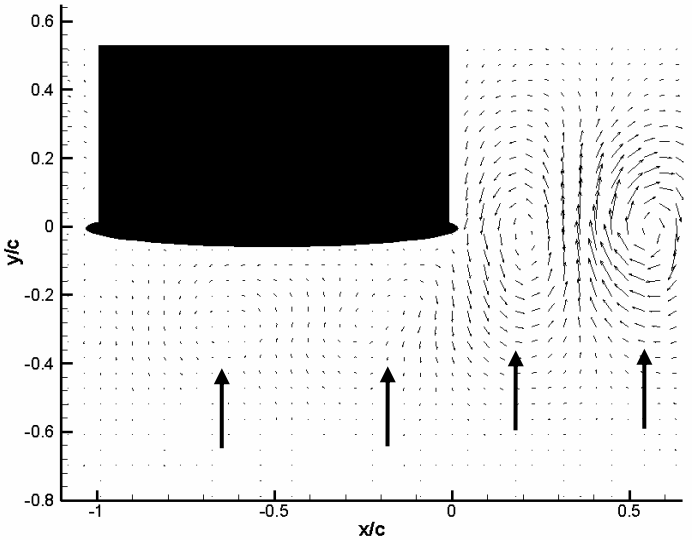

Figure 5.45. Max-blowing case, mode 3.

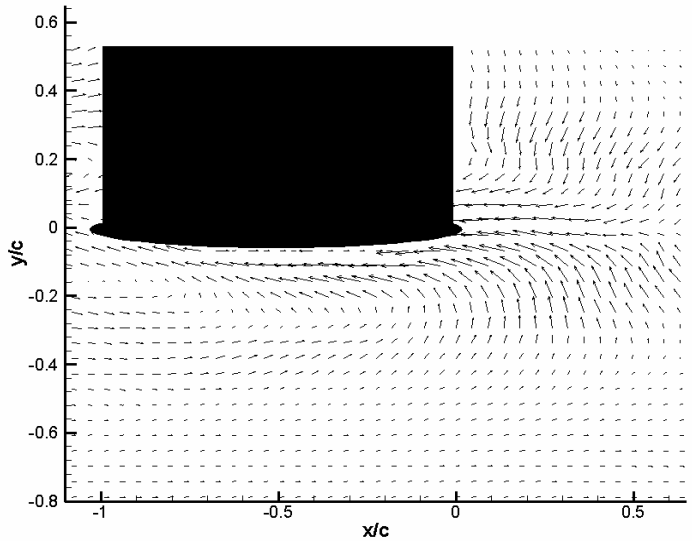

Figure 5.46. No-blowing case, mode 4.

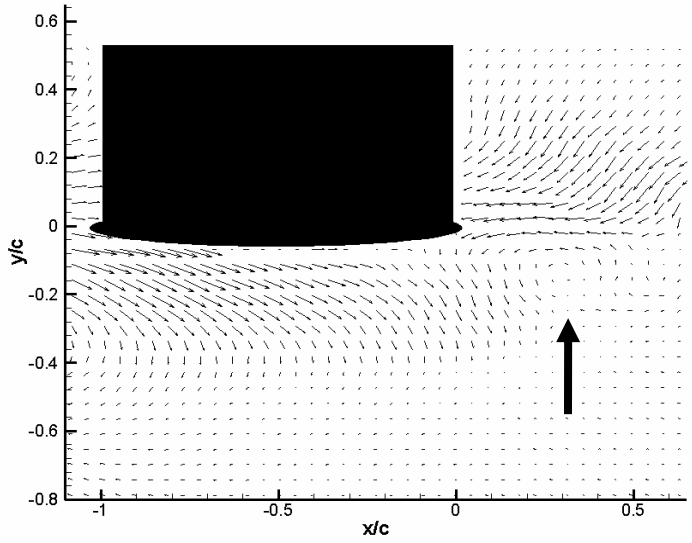

Figure 5.47. No-blowing case, mode 5.

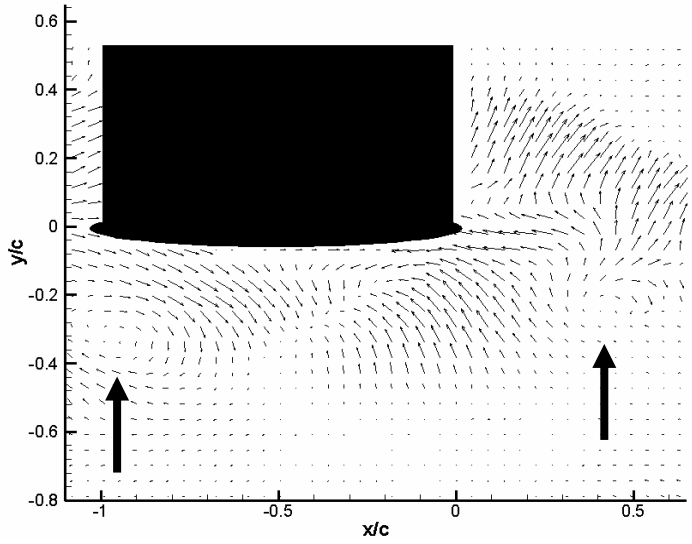

Figure 5.48. No-blowing case, mode 6.

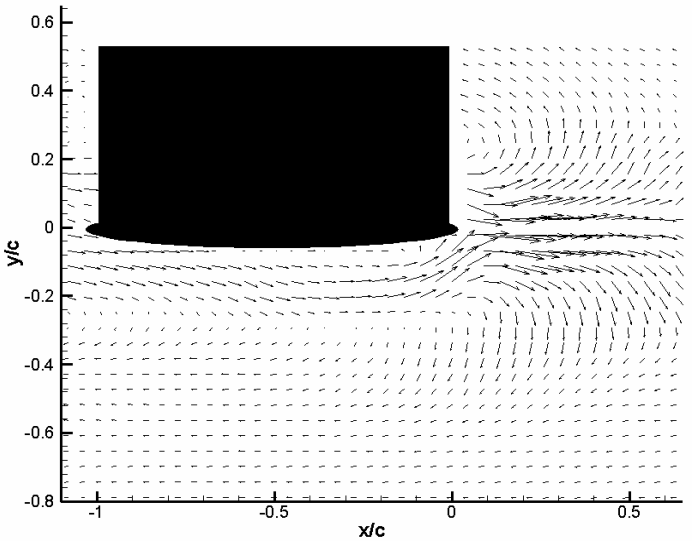

Figure 5.49. Max-blowing case, mode 4.

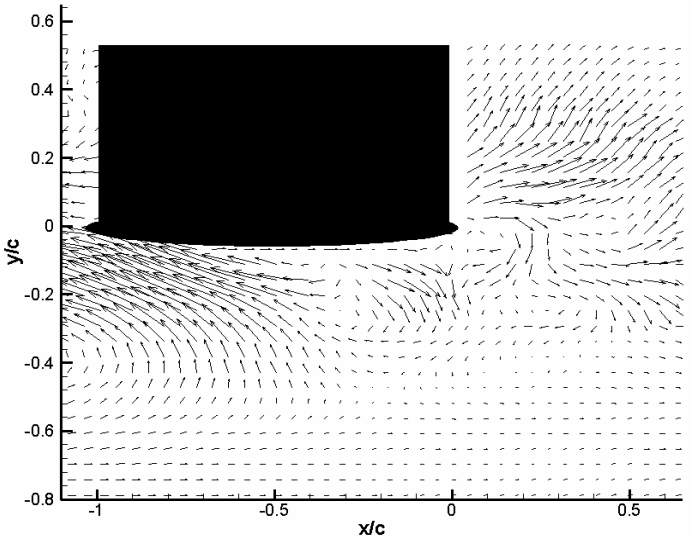

Figure 5.50. Max-blowing case, mode 5.

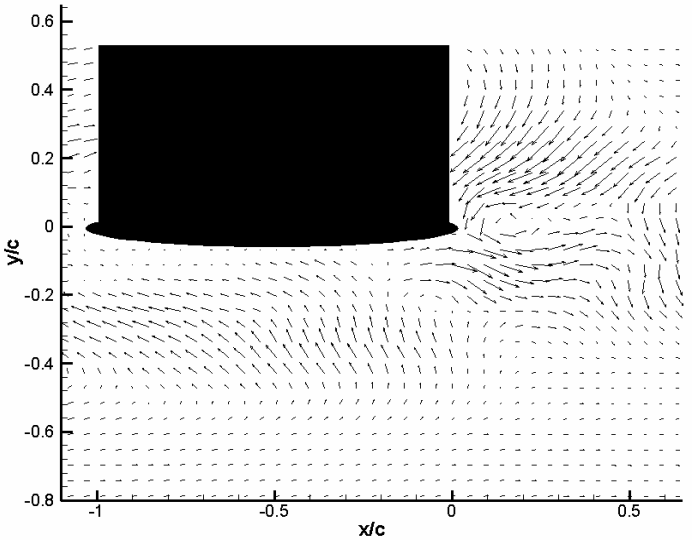

Figure 5.51. Max-blowing case, mode 6.

The projection coefficients for the first six modes were analyzed to ascertain what each mode physically corresponds to. These are shown in Figure 5.52 – Figure 5.63. The spectra for the first mode shape in each blowing condition verify the qualitative assessment previously given; the low frequency spectra indicate a very steady flow-field. Thus the first mode is due to the mean flow field. The second and third modes have large spectral signatures at the shedding frequency of the circular cylinder (5.9 Hz), and thus compromise the large vortical structures. The low frequency of the fourth mode indicates another steady flow field characteristic. For the no-blowing case, this is the standard vortex convection mode. For the maximum blowing case, the flow field is inverted and shows the influence of the LEB jet which penetrates into the wake of the circular cylinder and is subsequently turned and realigned with the mean flow direction.

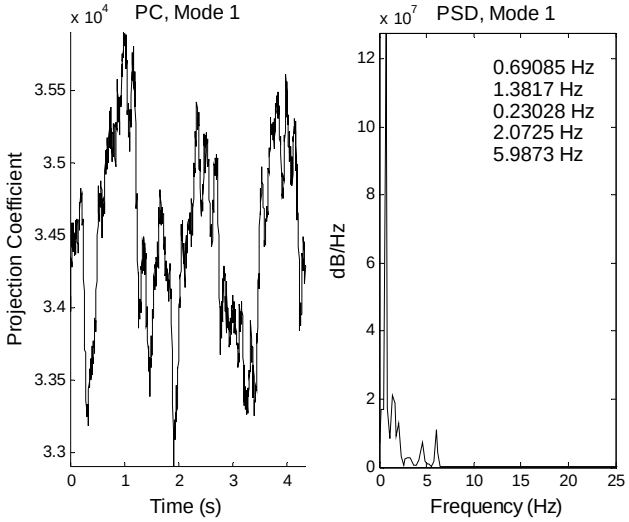

Figure 5.52. No-blowing case, mode 1 projection coefficient.

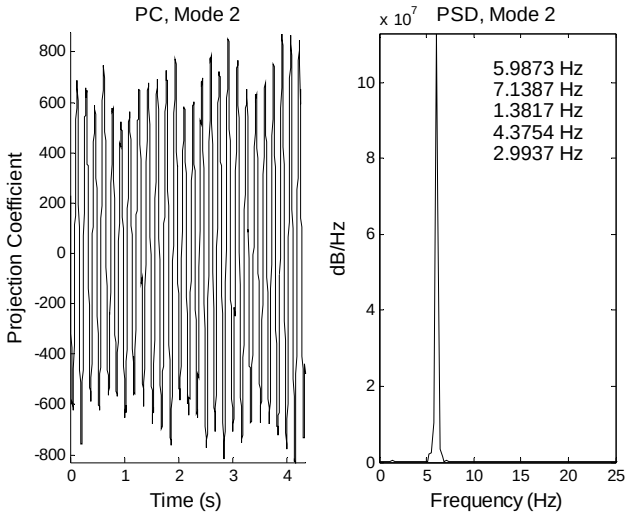

Figure 5.53. No-blowing case, mode 2 projection coefficient.

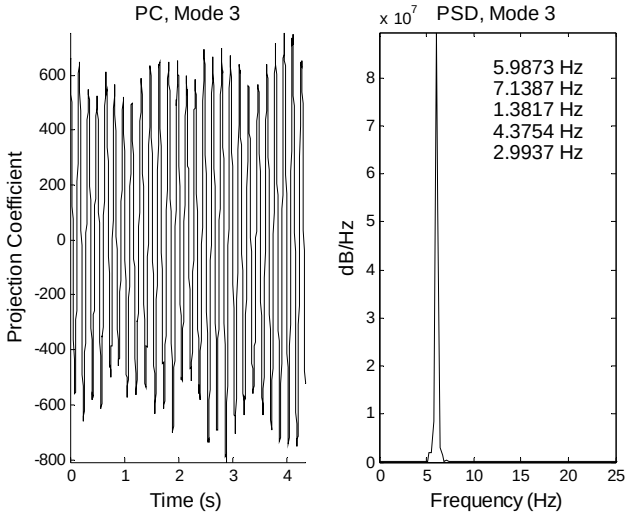

Figure 5.54. No-blowing case, mode 3 projection coefficient.

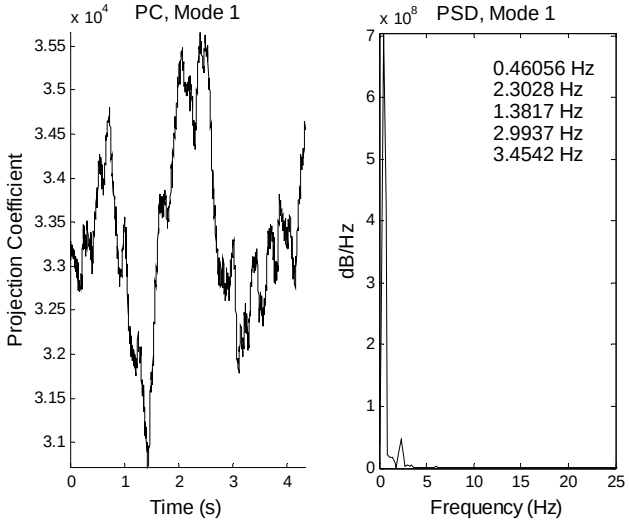

Figure 5.55. Max-blowing case, mode 1 projection coefficient.

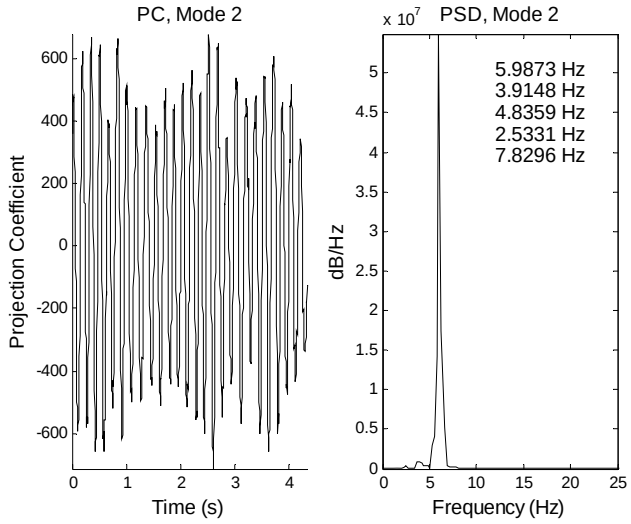

Figure 5.56. Max-blowing case, mode 2 projection coefficient.

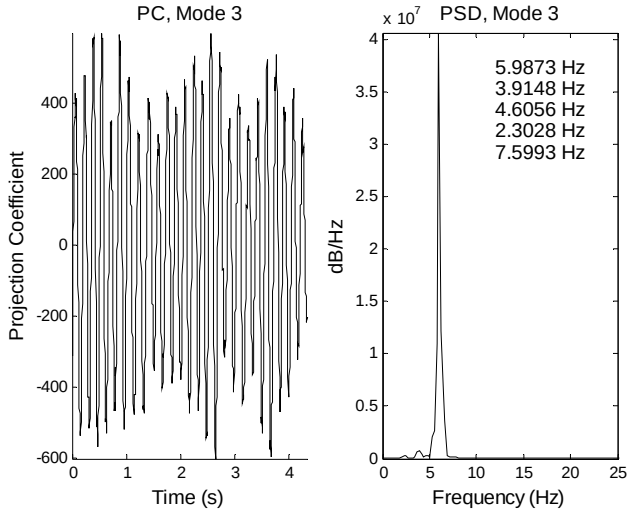

Figure 5.57. Max-blowing case, mode 3 projection coefficient.

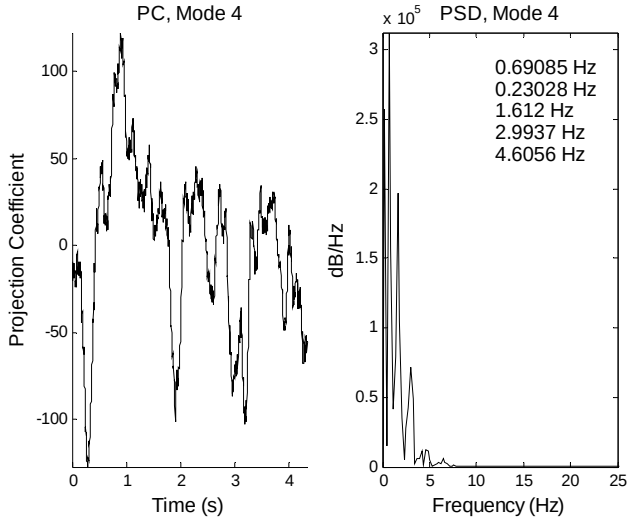

Figure 5.58. No-blowing case, mode 4 projection coefficient.

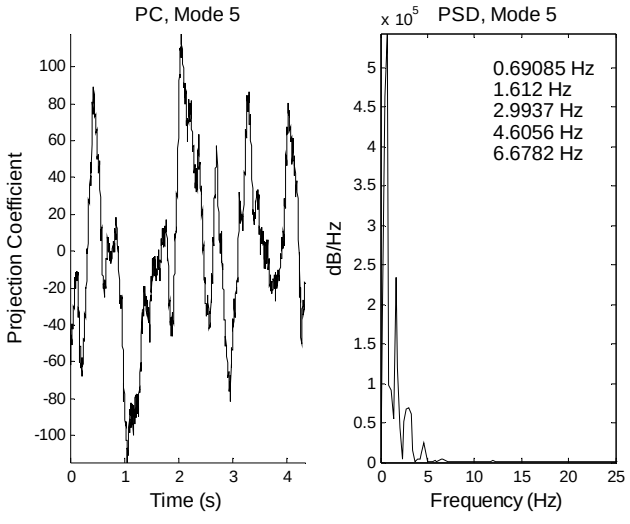

Figure 5.59. No-blowing case, mode 5 projection coefficient.

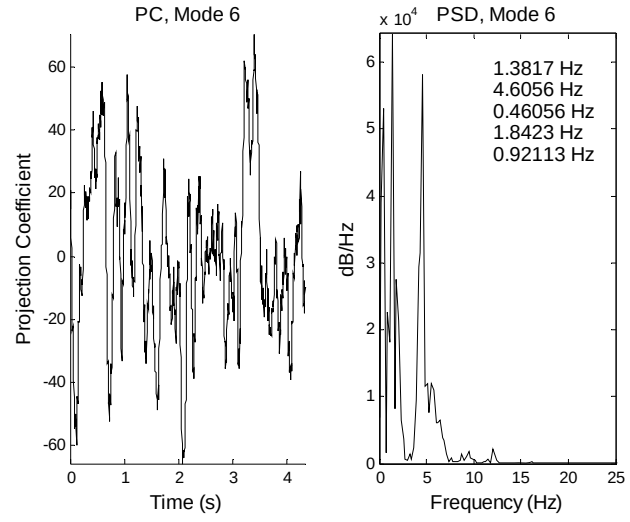

Figure 5.60. No-blowing case, mode 6 projection coefficient.

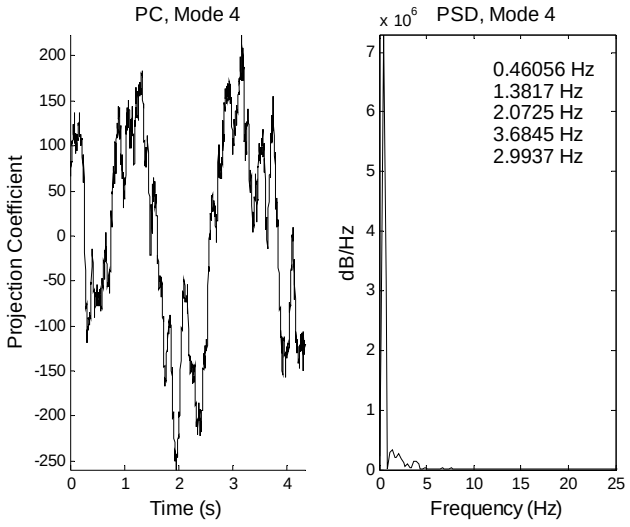

Figure 5.61. Max-blowing case, mode 4 projection coefficient.

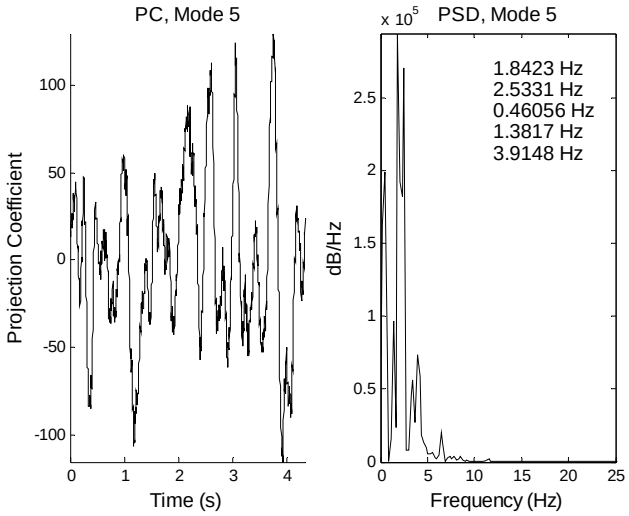

Figure 5.62. Max-blowing case, mode 5 projection coefficient.

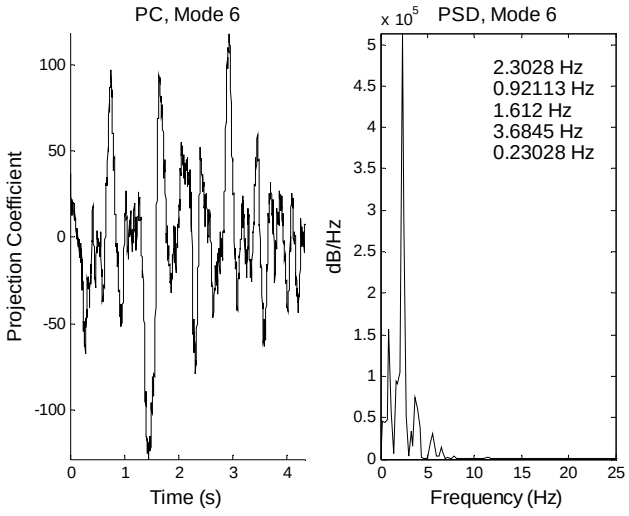

Figure 5.63. Max-blowing case, mode 6 projection coefficient.

5.3 ADDITIONAL MODE SHAPES AND PROJECTION COEFFICIENT ANALYSIS FOR CASE 4 – MEAN FLOW FIELD SUBTRACTED

For this case, the use of LEB had a detrimental effect on the BVI. The energetics of the POD modes are shown in Figure 5.65 and Figure 5.66. Note that in the first mode alone, the non-blowing case contains 10% of the total energy, while for C_μ=0.21 the first mode contains about 16% of the total energy. For both cases only about 1% of the flow energy is contained in each of the modes past 20. It takes 331 eigenmodes to reconstruct 90% of the flow energy for the no blowing case while it takes 189 to reconstruct the same energy in the blowing case. As opposed to the previous situation, in which blowing acted to disrupt the flow field making it less organized, for the large cylinder the blowing actually increases the organization of the circular cylinder wake.

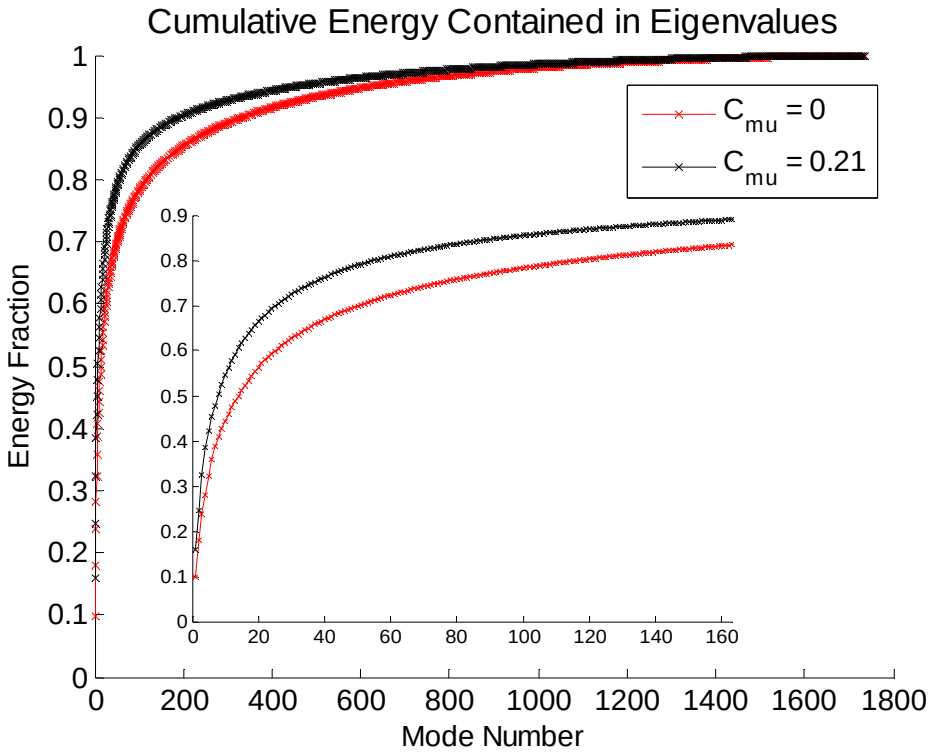

Figure 5.64. Cumulative energy contained in eigenmodes.

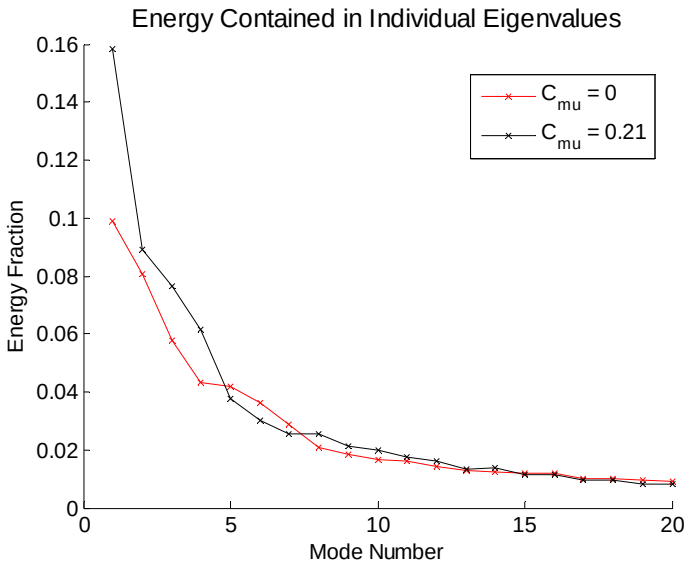

Figure 5.65. Energy contained in individual eigenmodes.

The individual modes for the no-blowing case are shown in Figure 5.66 - Figure 5.77. A comparison of the first modes for both blowing cases is interesting as it is readily apparent the "dead-water region" directly behind the circular cylinder is much more active with LEB. In addition, strong velocity vectors which track the closure point of the circular cylinder wake are displaced further downstream with LEB (marked with arrow). For the no-blowing case, modes three and four clearly show an evolution of vortices along the circular cylinder wake shear layer (marked with arrows). The PC and their spectra are shown in Figure 5.78 - Figure 5.89. For the no-blowing case, modes three and four show strong spectral components at about 2-2.5 Hz, which is the predicted

shedding frequency of the circular cylinder. Additionally, mode 1 for the no-blowing case and mode 2 for the maximum blowing case qualitatively resemble one another in shape, but a comparison of the spectra are fundamentally different. For the no-blowing case, the largest spectral component is very low frequency, while in the maximum blowing case; the largest spectral component for the maximum blowing case is seen at about 2 Hz.

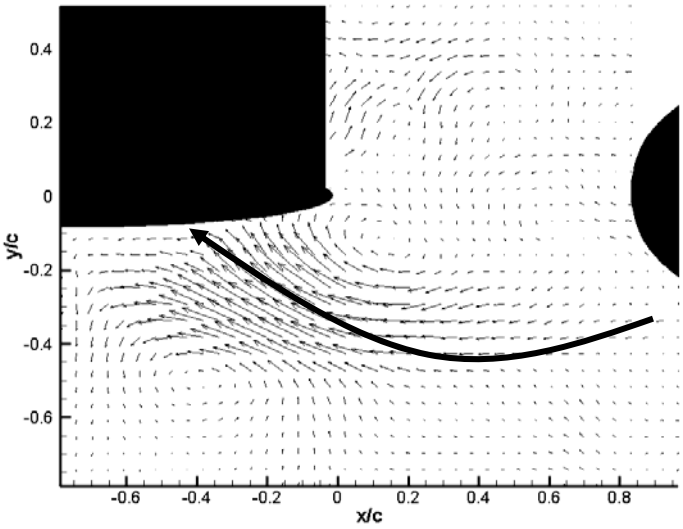

Figure 5.66. No-blowing case, mode 1.

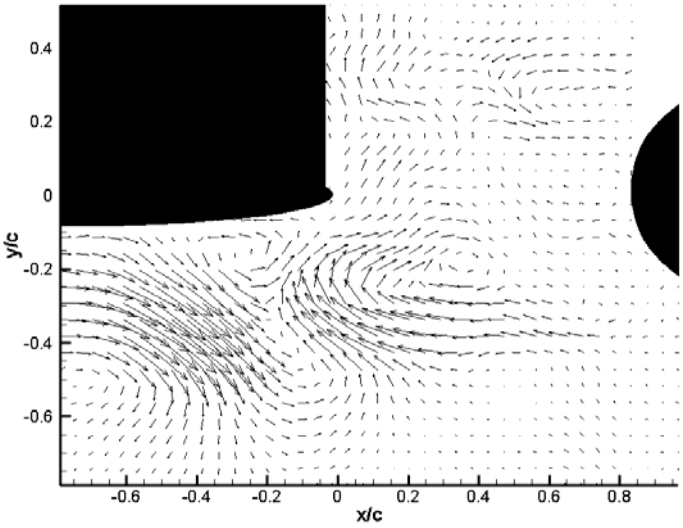

Figure 5.67. No-blowing case, mode 2.

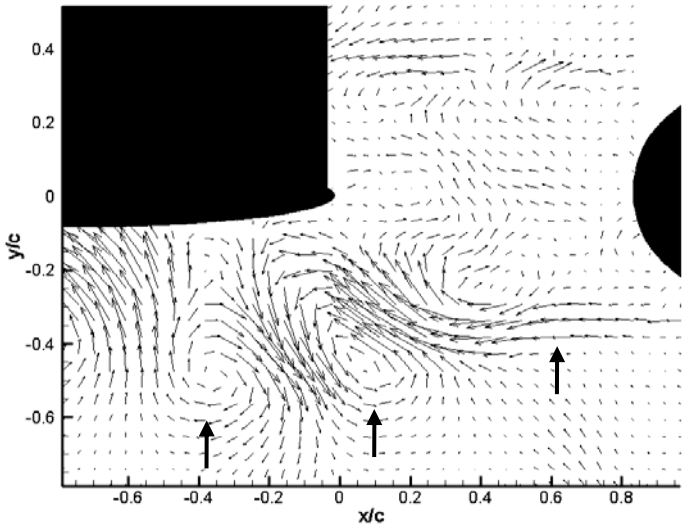

Figure 5.68. No-blowing case, mode 3.

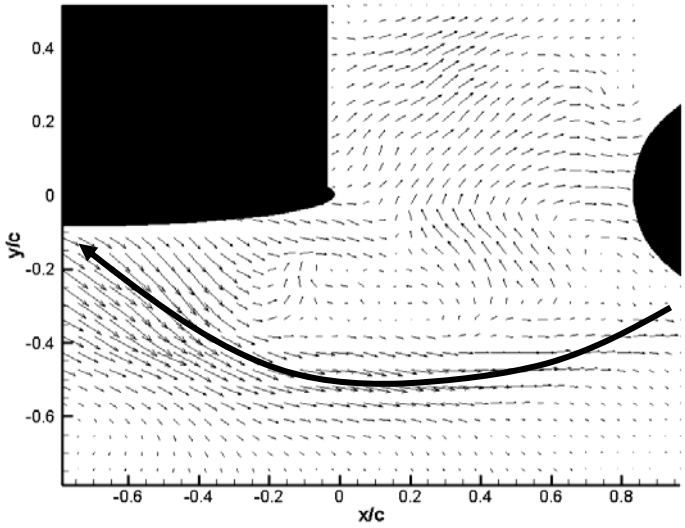

Figure 5.69. Max-blowing case, mode 1.

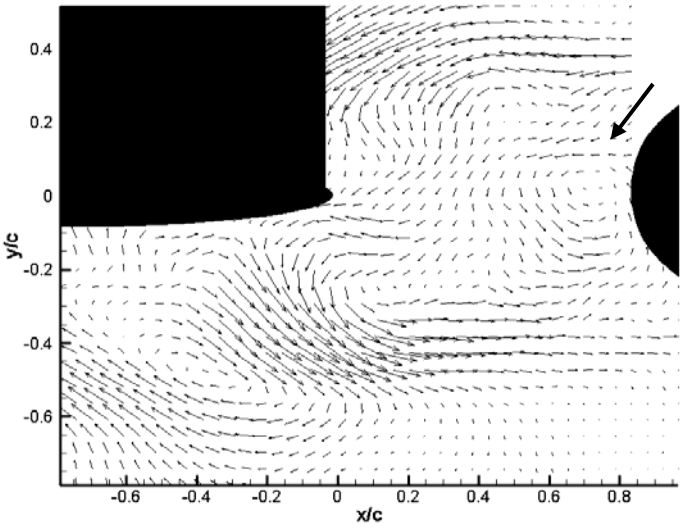

Figure 5.70. Max-blowing case, mode 2.

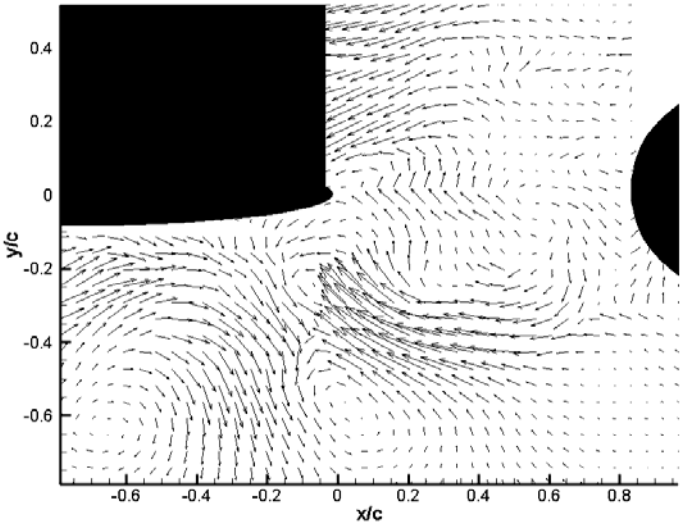

Figure 5.71. Max-blowing case, mode 3.

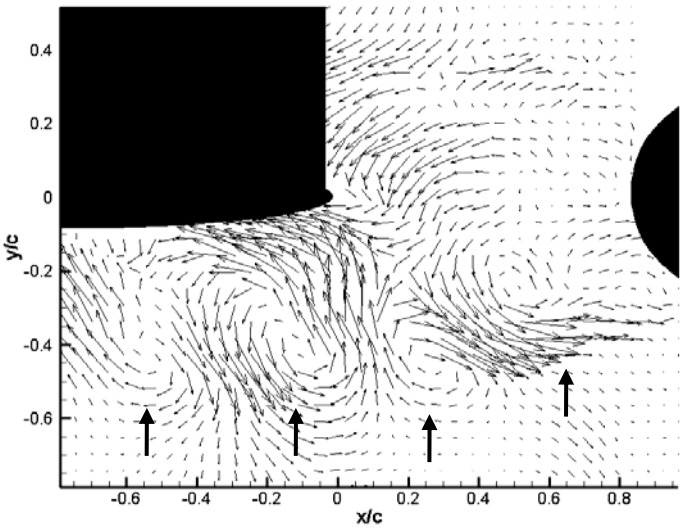

Figure 5.72. No-blowing case, mode 4.

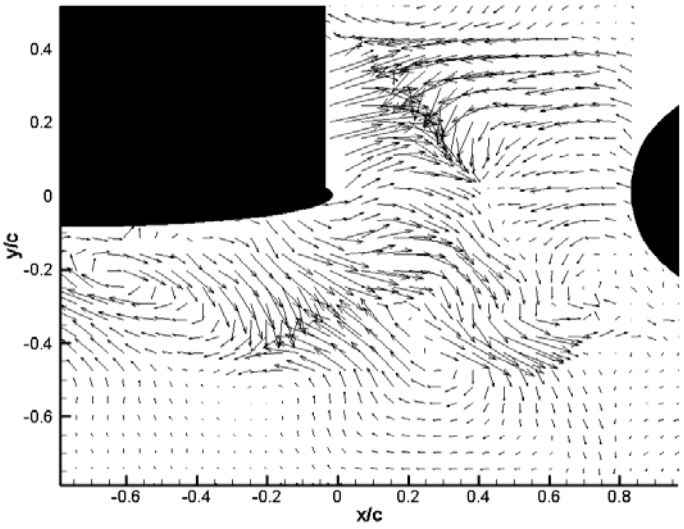

Figure 5.73. No-blowing case, mode 5.

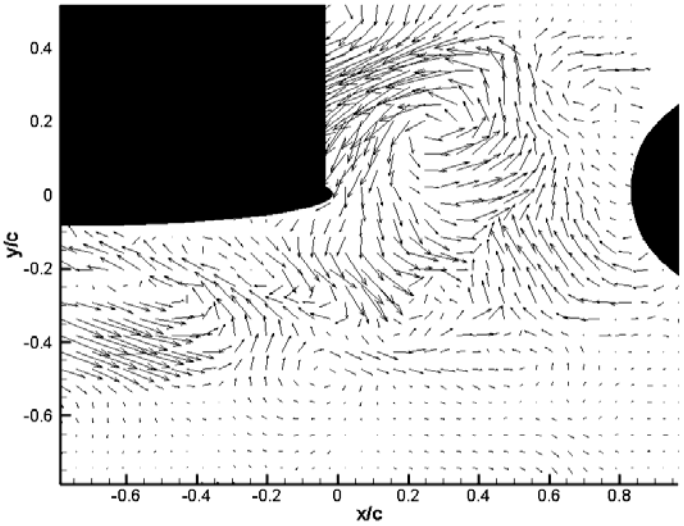

Figure 5.74. No-blowing case, mode 6.

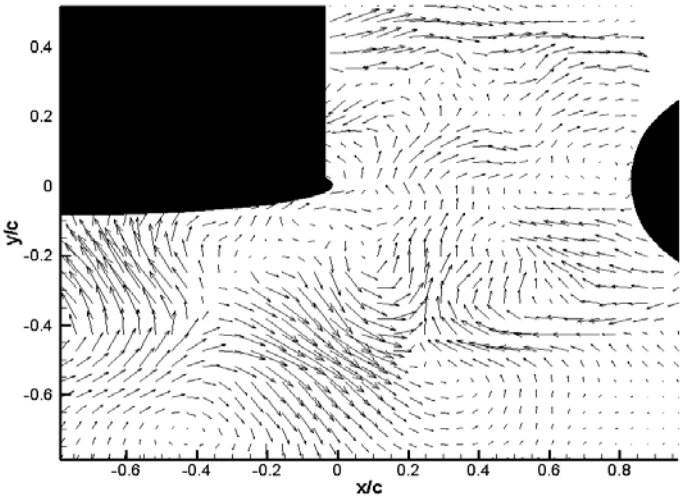

Figure 5.75. Max-blowing case, mode 4.

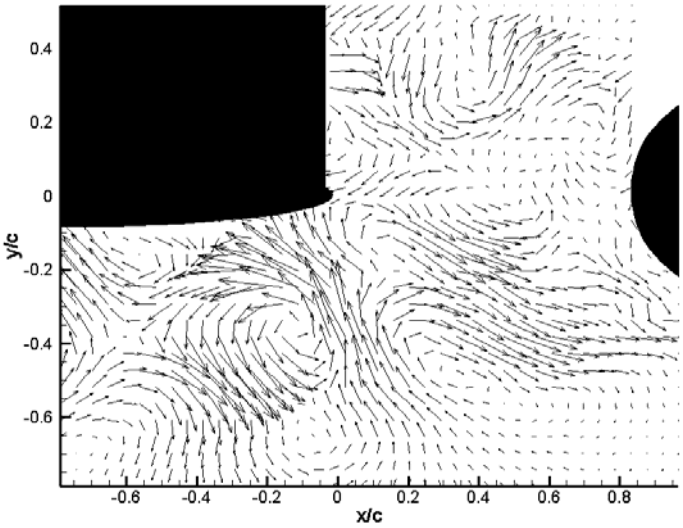

Figure 5.76. Max-blowing case, mode 5.

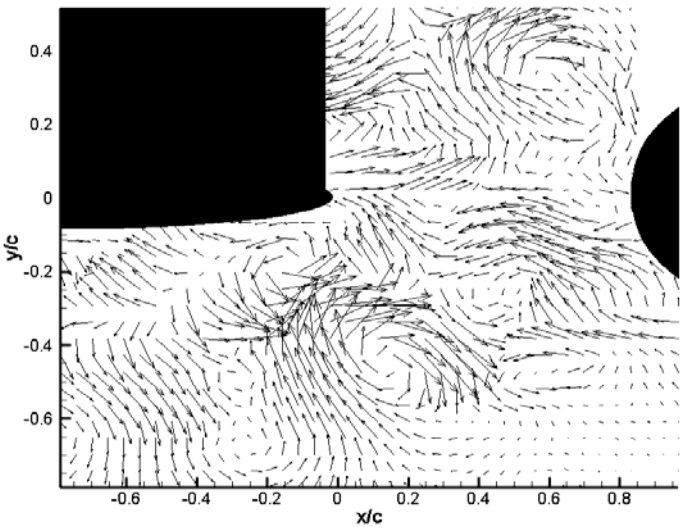

Figure 5.77. Max-blowing case, mode 6.

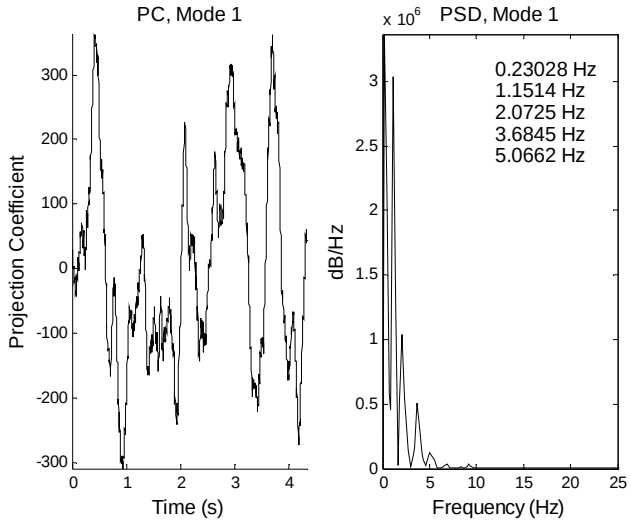

Figure 5.78. No-blowing case, mode 1 projection coefficient.

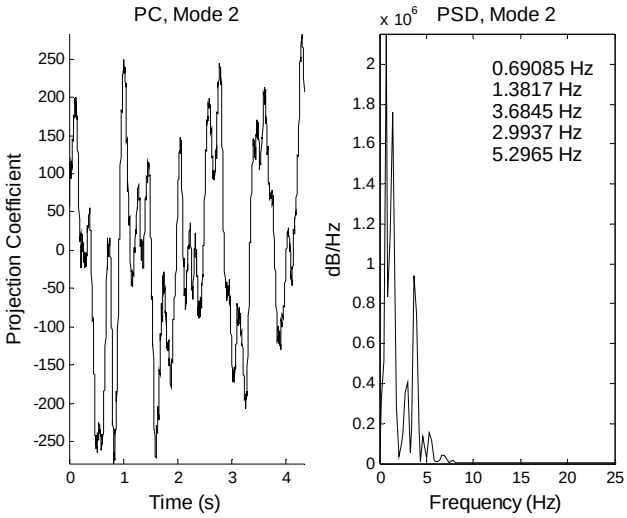

Figure 5.80. No-blowing case, mode 2 projection coefficient.

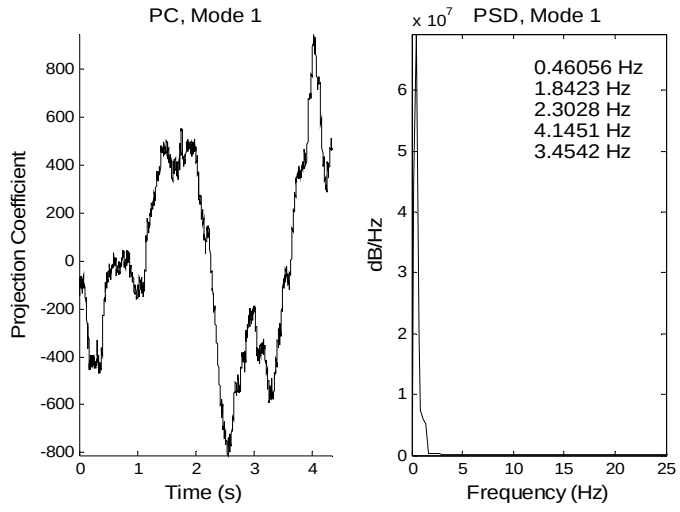

Figure 5.79. Max-blowing case, mode 1 projection coefficient.

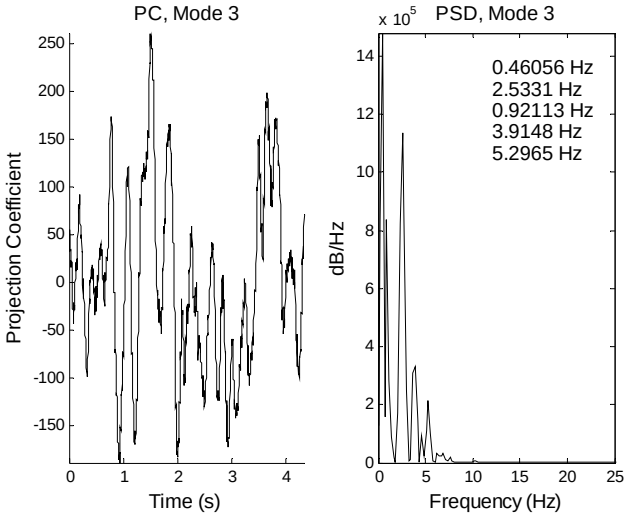

Figure 5.81. No-blowing case, mode 3 projection coefficient.

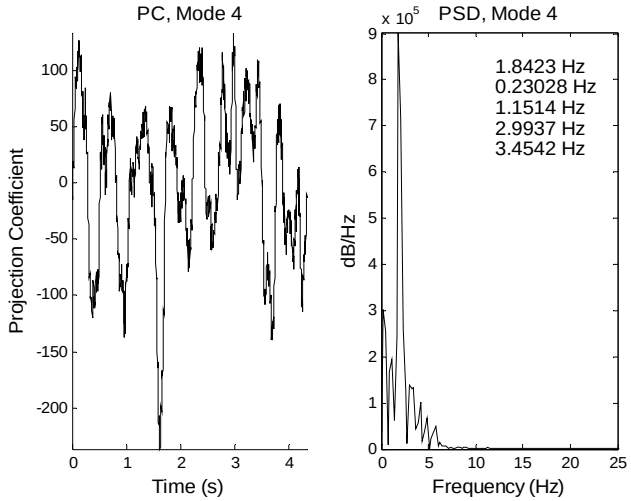

Figure 5.82. No-blowing case, mode 4 projection coefficient.

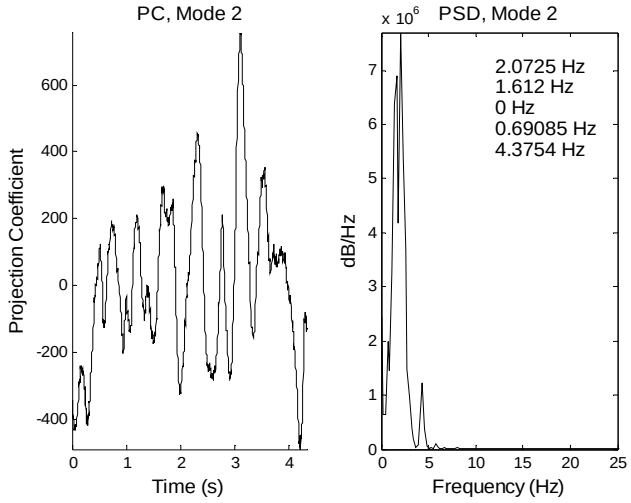

Figure 5.83. Max-blowing case, mode 2 projection coefficient.

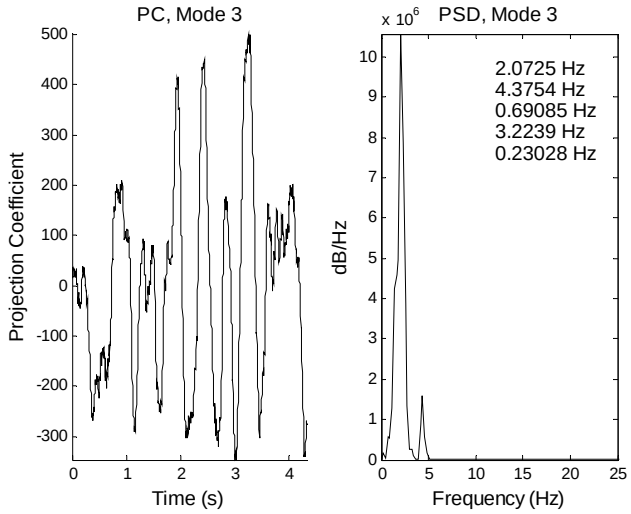

Figure 5.84. Max-blowing case, mode 3 projection coefficient.

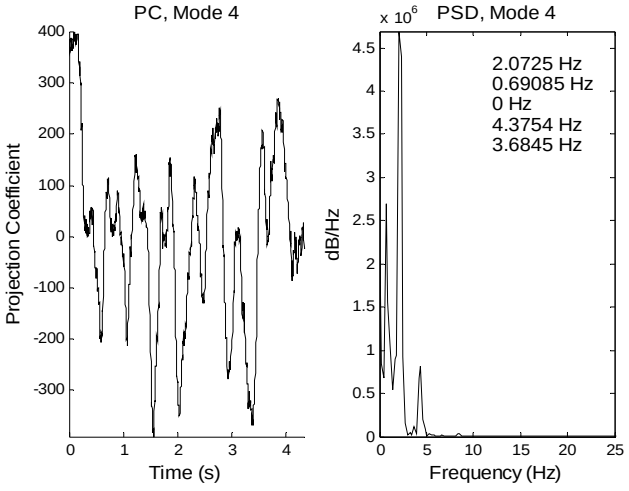

Figure 5.85. Max-blowing case, mode 4 projection coefficient.

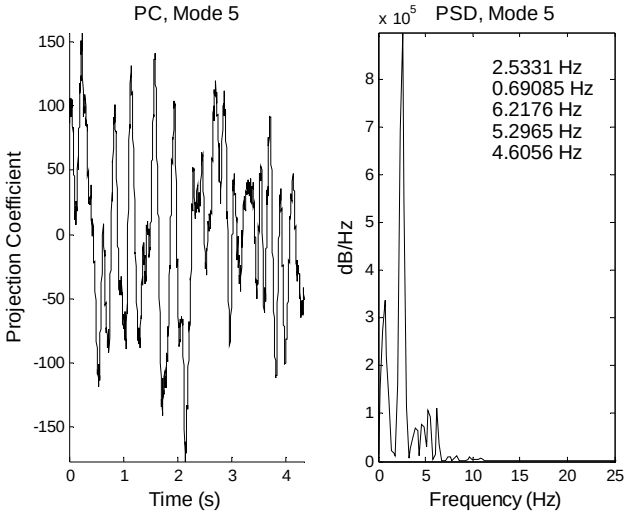

Figure 5.86. No-blowing case, mode 5 projection coefficient.

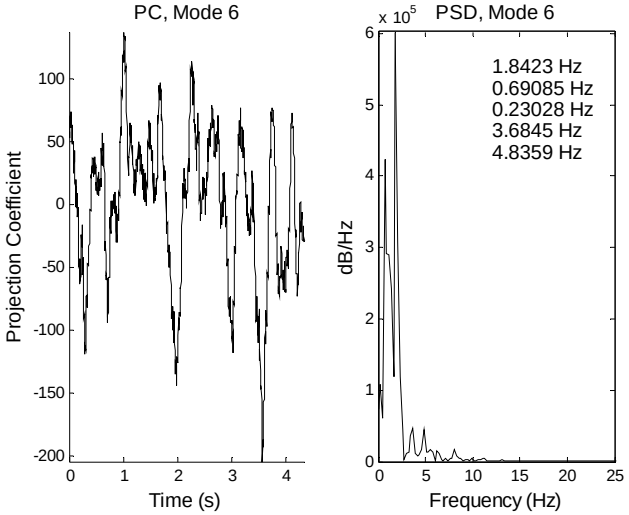

Figure 5.87. No-blowing case, mode 6 projection coefficient.

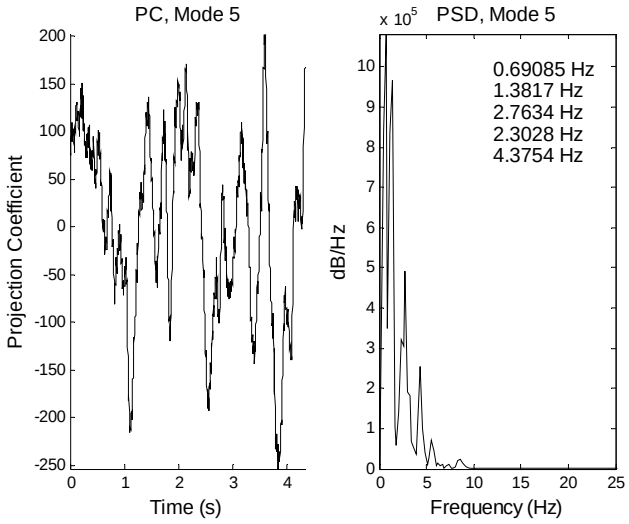

Figure 5.88. Max-blowing case, mode 5 projection coefficient.

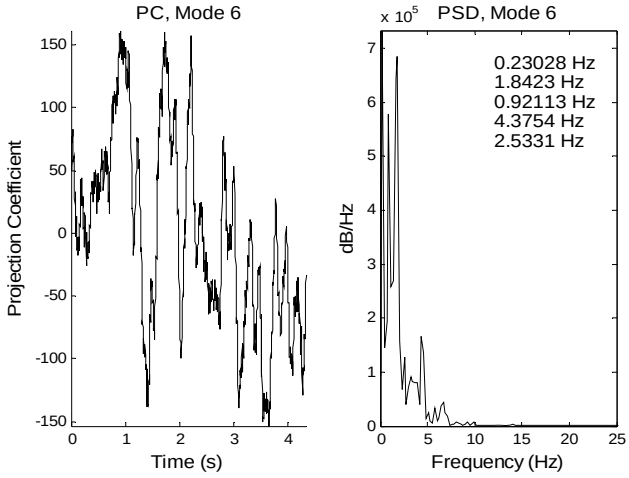

Figure 5.89. Max-blowing case, mode 6 projection coefficient.

5.4 ADDITIONAL MODE SHAPES AND PROJECTION COEFFICIENT ANALYSIS FOR CASE 4 – MEAN FLOW FIELD INCLUDED

The mode energy distribution is shown in Figure 5.90. As in the previous case, the first mode corresponds to the mean flow field and accounts for at least 92% of the total flow energy.

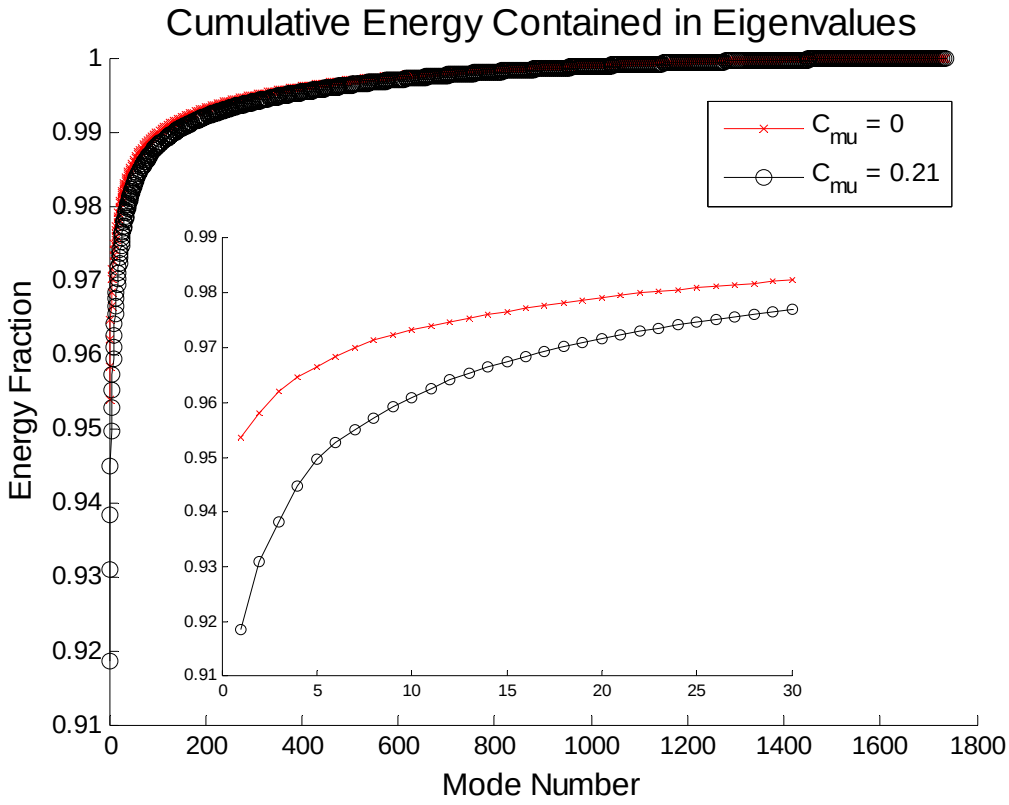

Figure 5.90. Energy contribution from modes for case 5, mean flow field included in the POD analysis.

The first six modes for the no-blowing and maximum blowing cases are shown in Figure 5.91 – Figure 102. As previously mentioned, the first mode corresponds to the mean flow field, which was not subtracted for this analysis. Interpretation of the next several modes becomes more difficult. Figure 5.96 and Figure 5.97 (no-blowing cases, modes 4 and 5 respectively) appear to show the shear layer instability of the circular cylinder wake. An evolution of vortices along the shear layer that separates the wake of the circular cylinder and the outer flow region (i.e. that which is not affected by the circular cylinder) is clearly seen (vortices' locations are marked with arrow), and in fact large velocity vectors (in comparison to the surrounding vectors) are seen leaving the edge of the circular cylinder region at approximately y/c=-0.35 and x/c=0.4-0.8. A comparison between the second and third modes directly in the wake of the circular cylinder shows this "dead-water region" to be much more active for the maximum LEB case. Also, mode 2 for the no-blowing case and mode 3 for the maximum blowing case are very similar in appearance, although for the maximum blowing case, the dead-water region is much more active.

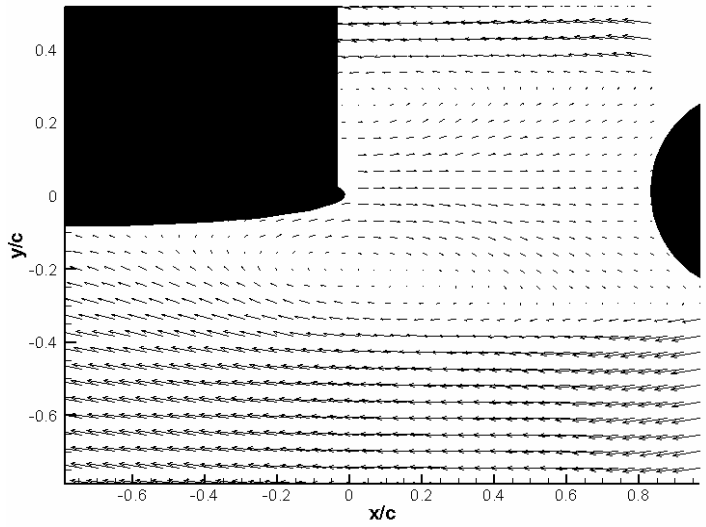

Figure 5.91. No-blowing case, mode 1.

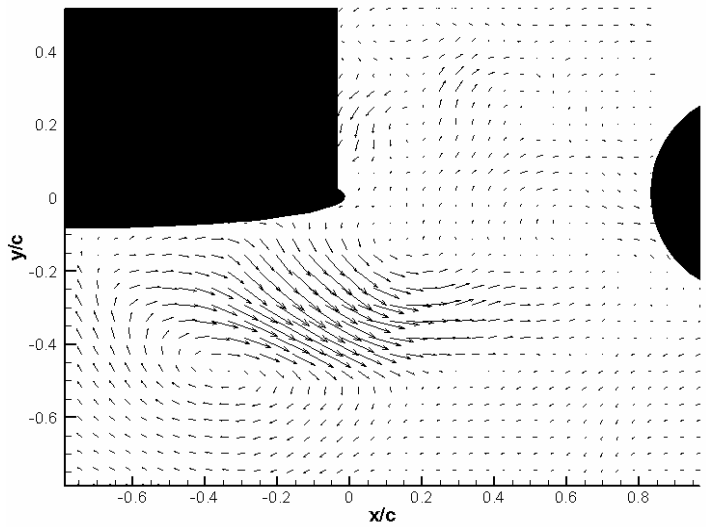

Figure 5.92. No-blowing case, mode 2.

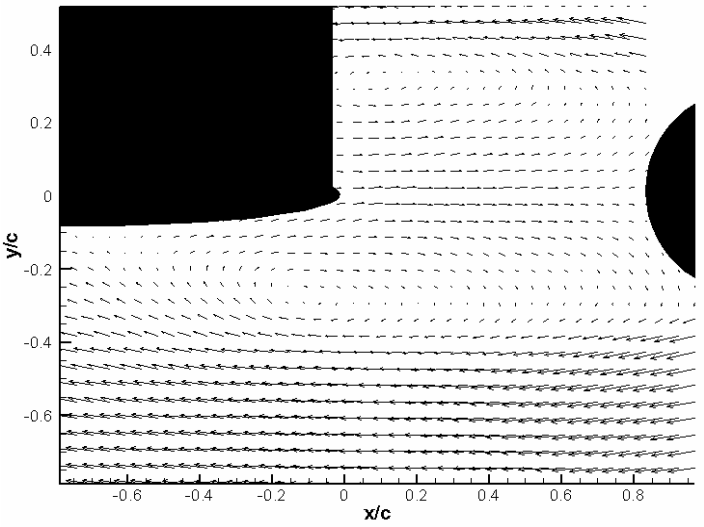

Figure 5.93. Max-blowing case, mode 1.

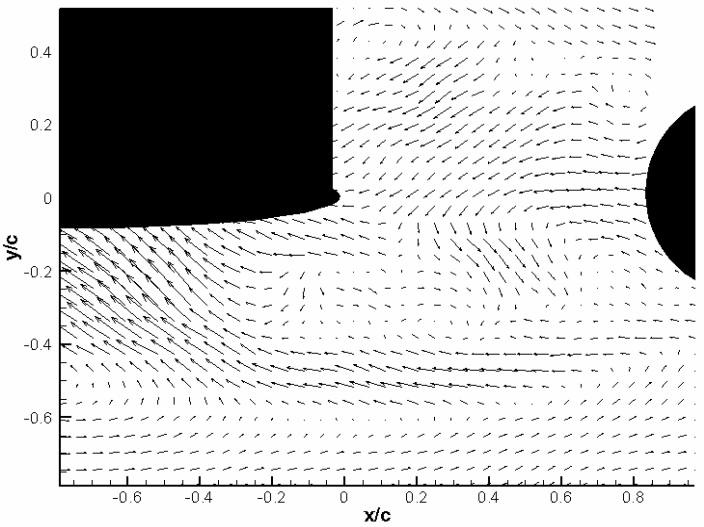

Figure 5.94. Max-blowing case, mode 2.

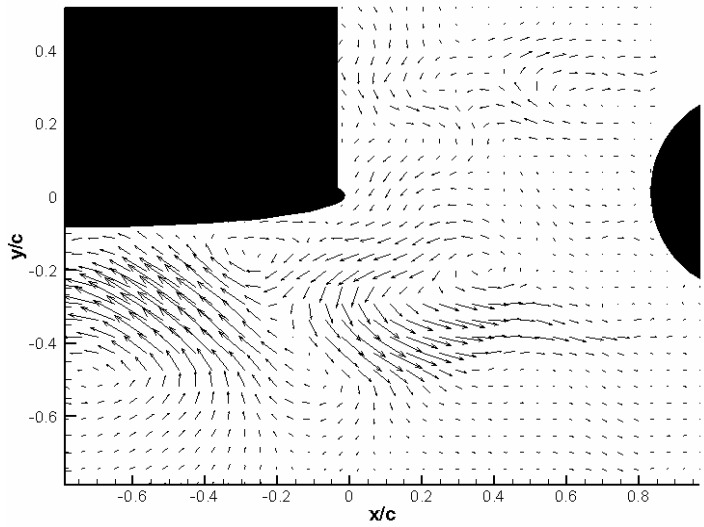

Figure 5.95. No-blowing case, mode 3.

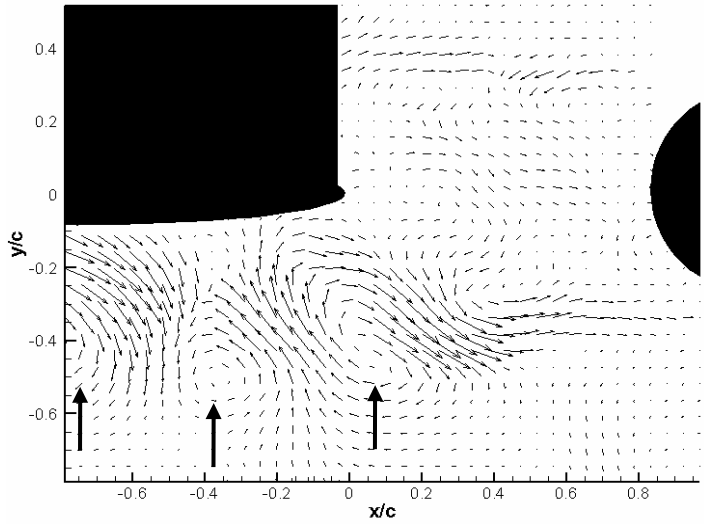

Figure 5.96. No-blowing case, mode 4.

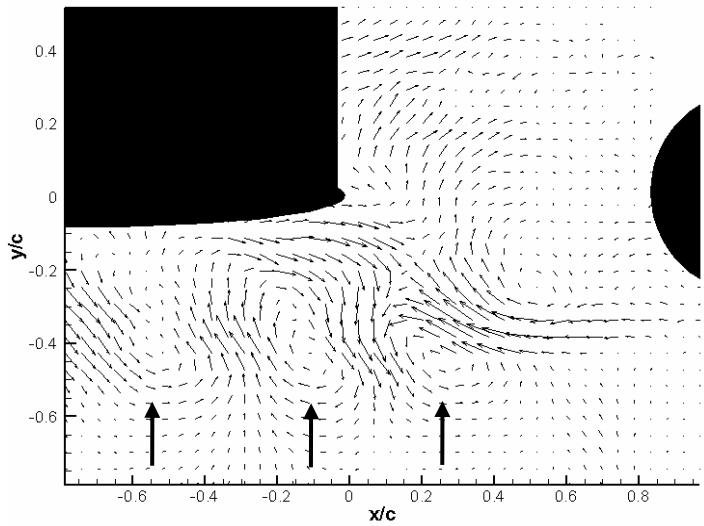

Figure 5.97. No-blowing case, mode 5.

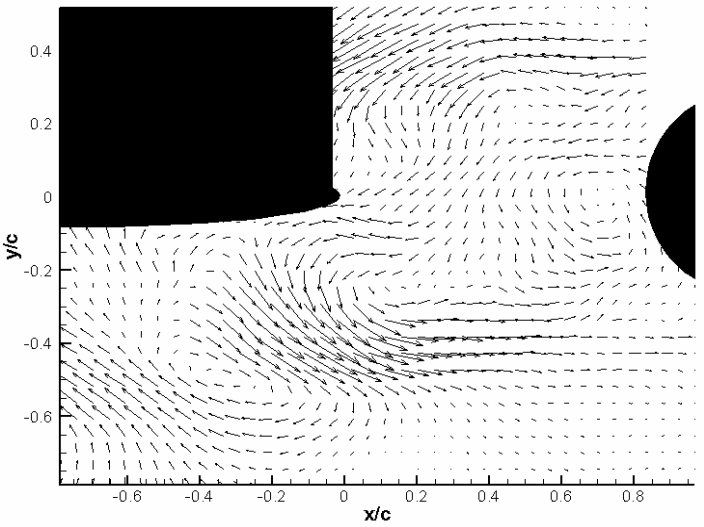

Figure 5.98. Max-blowing case, mode 3.

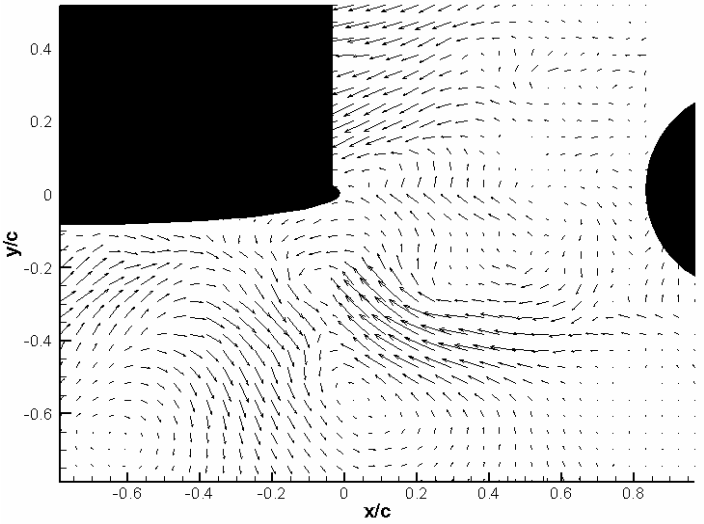

Figure 5.99. Max-blowing case, mode 4.

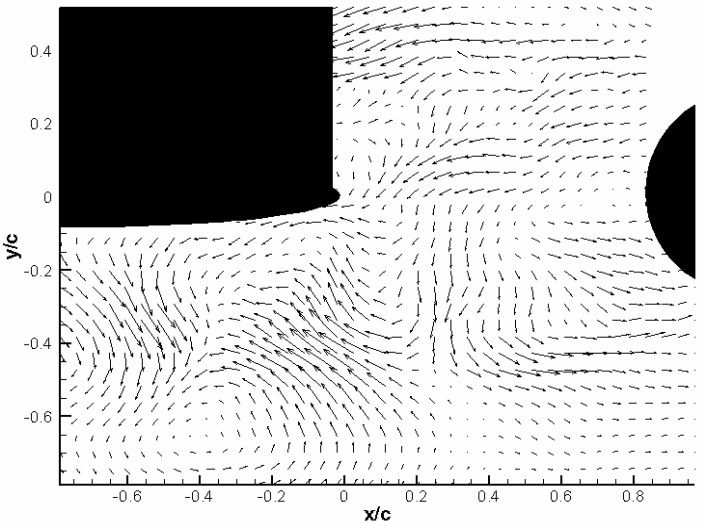

Figure 5.100. Max-blowing case, mode 5.

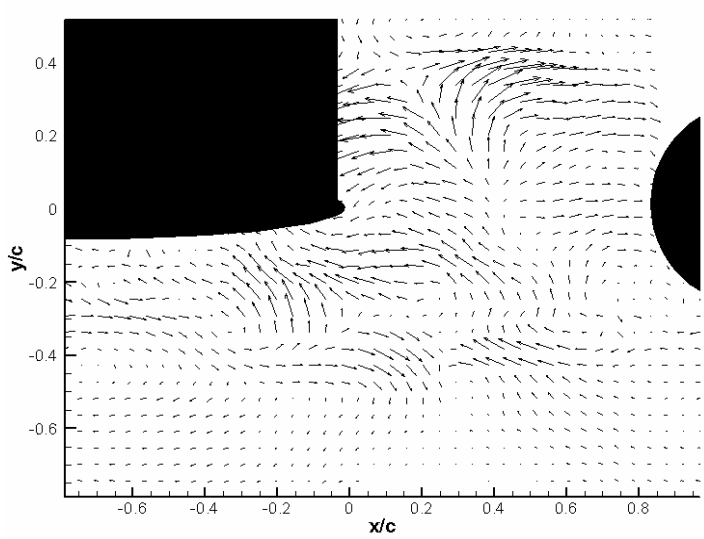

Figure 5.101. No-blowing case, mode 6.

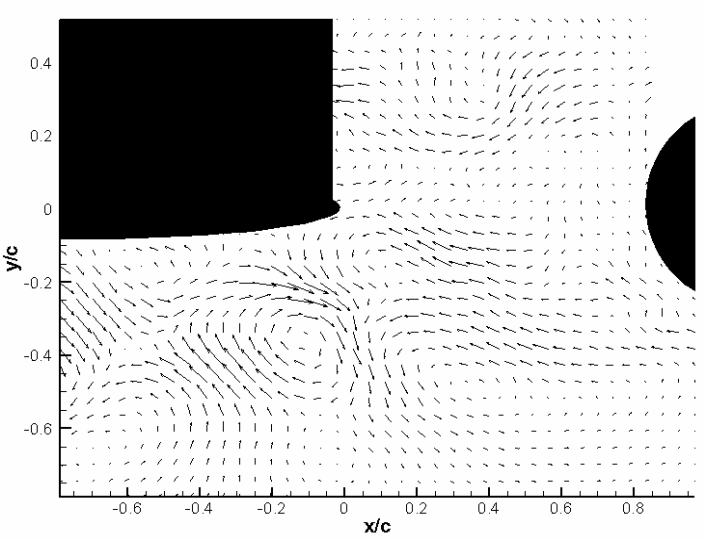

Figure 5.102. Max-blowing case, mode 6.

The projection coefficients (PC) for the first six modes were analyzed to ascertain what each mode physically corresponds to. These are shown in Figure 5.103-Figure 5.114. The first modes for the no-blowing and maximum blowing cases correspond to the mean flow-field; this is demonstrated by the very low frequency seen in these modes. For the no-blowing case, the fourth and fifth modes show strong concentration at the predicted shedding frequency of the circular cylinder; these spectral results may be compared to the mode shapes which show the shear layer instability of the circular cylinder wake.

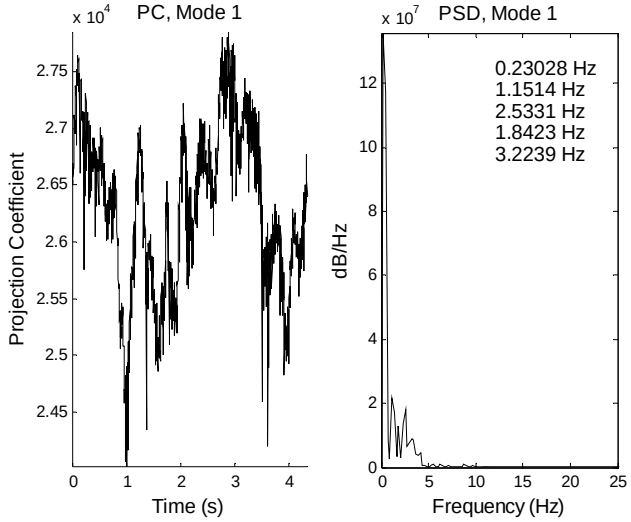

Figure 5.103. No-blowing case, mode 1 projection coefficient.

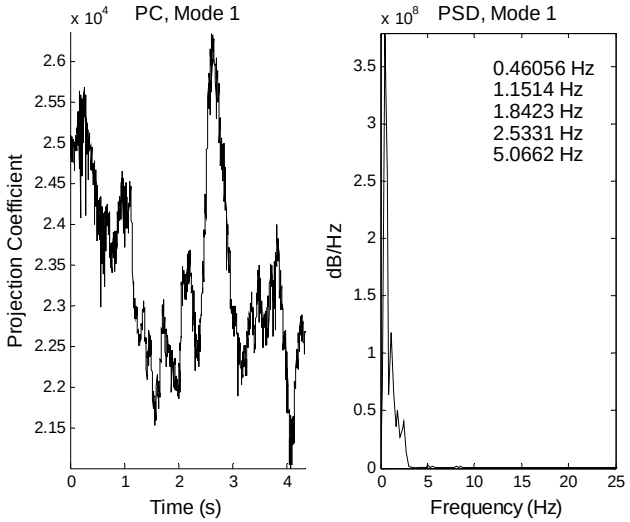

Figure 5.105. Max-blowing case, mode 1 projection coefficient.

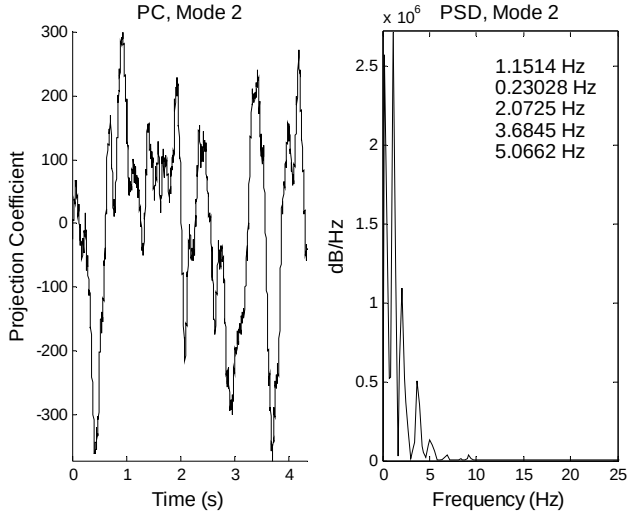

Figure 5.104. No-blowing case, mode 2 projection coefficient.

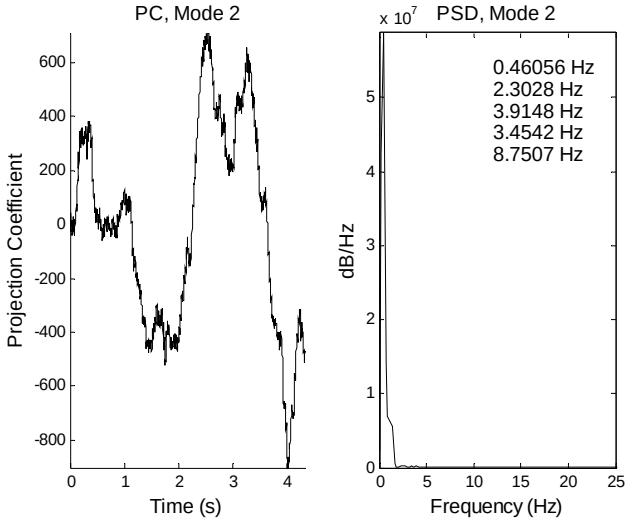

Figure 5.106. Max-blowing case, mode 2 projection coefficient.

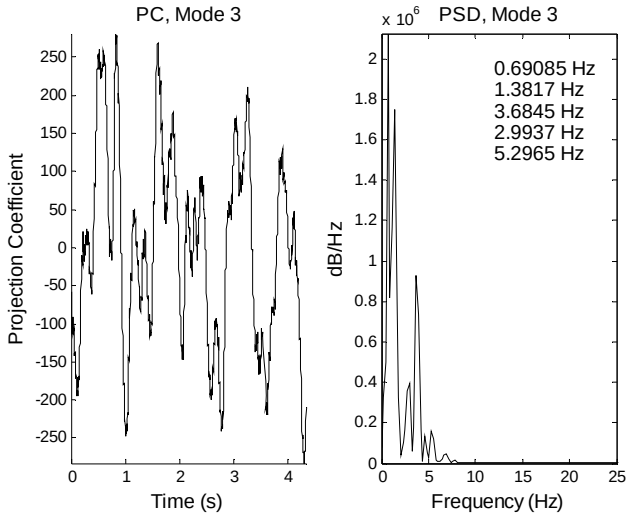

Figure 5.107. No-blowing case, mode 3 projection coefficient.

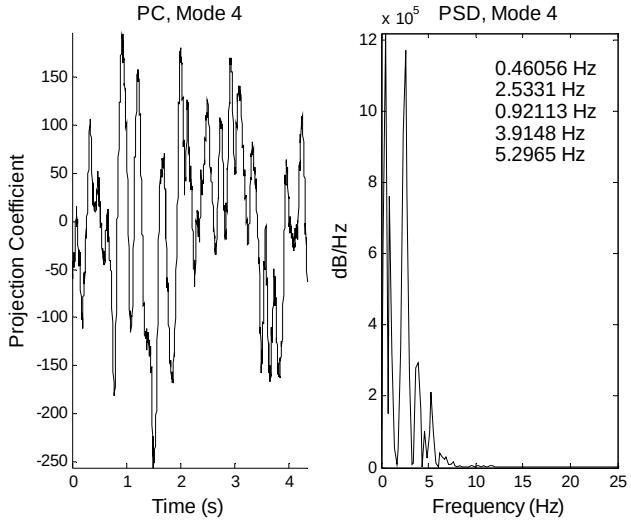

Figure 5.108. No-blowing case, mode 4 projection coefficient.

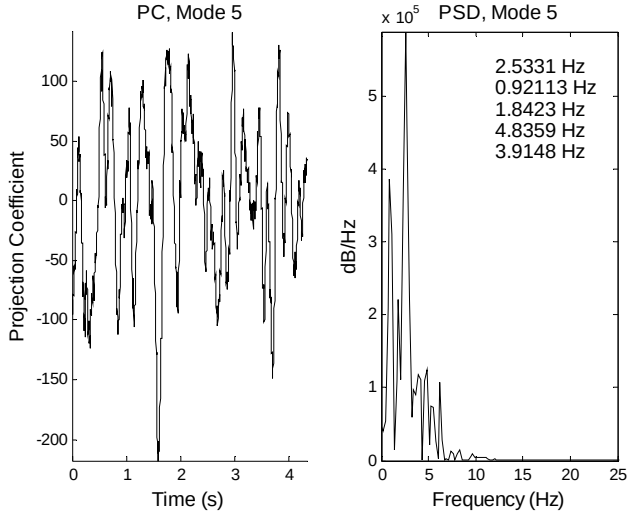

Figure 5.109. No-blowing case, mode 5 projection coefficient.

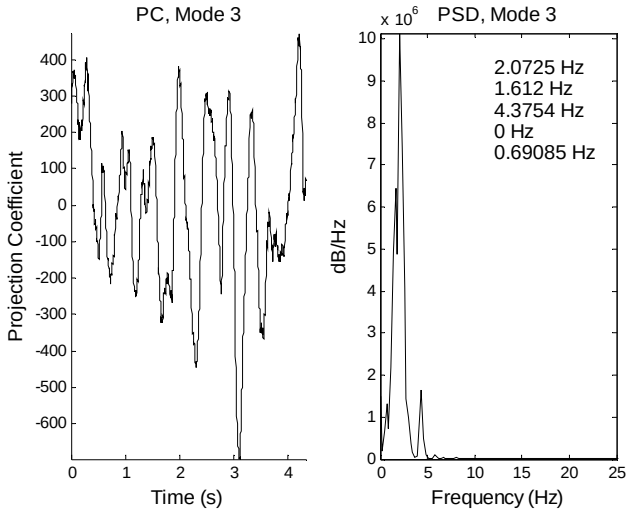

Figure 5.110. Max-blowing case, mode 3 projection coefficient.

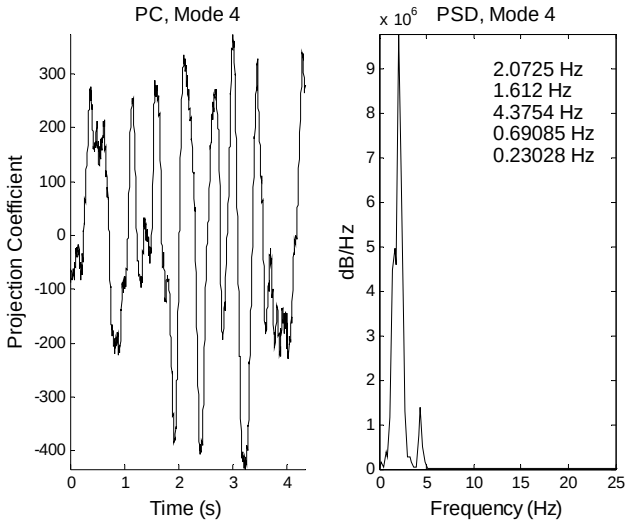

Figure 5.111. Max-blowing case, mode 4 projection coefficient.

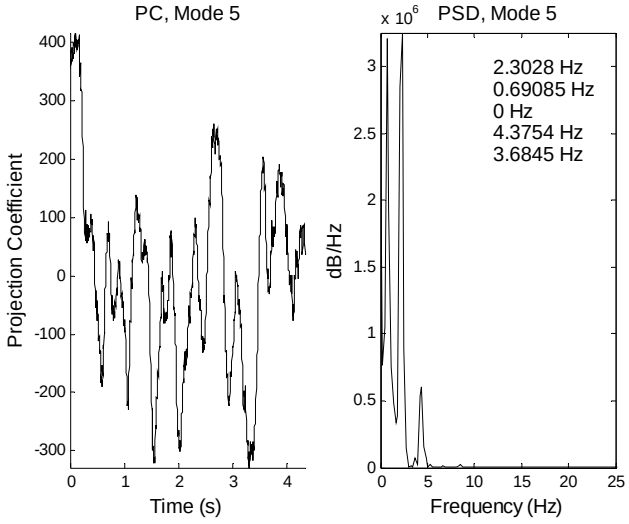

Figure 5.112. Max-blowing case, mode 5 projection coefficient.

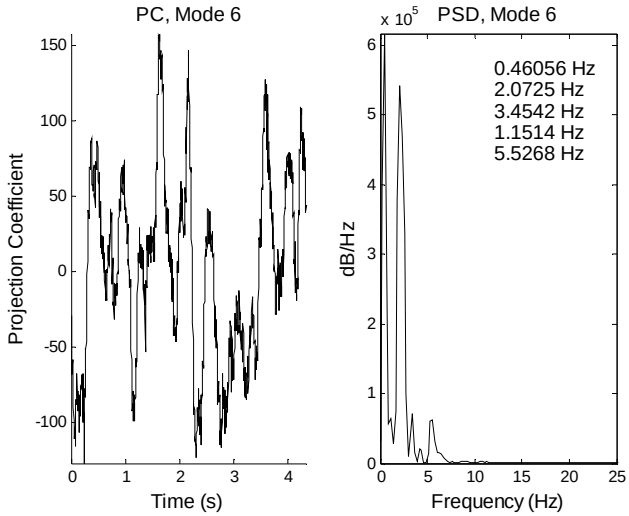

Figure 5.113. No-blowing case, mode 6 projection coefficient.

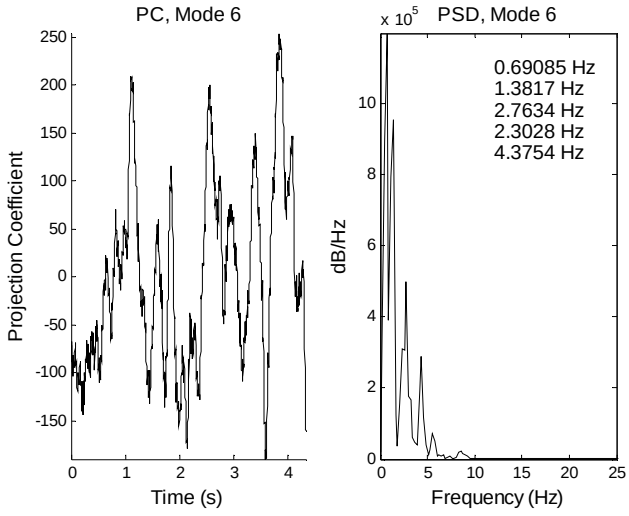

Figure 5.114. Max-blowing case, mode 6 projection coefficient.

6 Appendix IV – Comprehensive Listing of Accelerometer Data Taken

This Appendix contains a listing, organized by time, of all the accelerometer data taken on the LEB test apparatus over the course of the project. Many of the plot legends contain a reference to "station 1, station 2," etc. These refer to the upstream distance of the cylinder being used to excite the airfoil vibration; the center hole of the circular cylinder mount is 2 inches upstream of the edge of the airfoil (station 1), and each descending station is 2 inches upstream from the previous. Station 7 is 14 inches from the tip of the airfoil to the circular cylinder mounting hole.

4.29.05

The first experiment done for this project was measuring the vibration of an air for due to the wake of a circular cylinder. Here, four different diameter cylinders where placed up stream of an air flow in different locations in hopes of inducing vibration due to vortex interaction. The vibration of the air foil was measured using accelerometers.

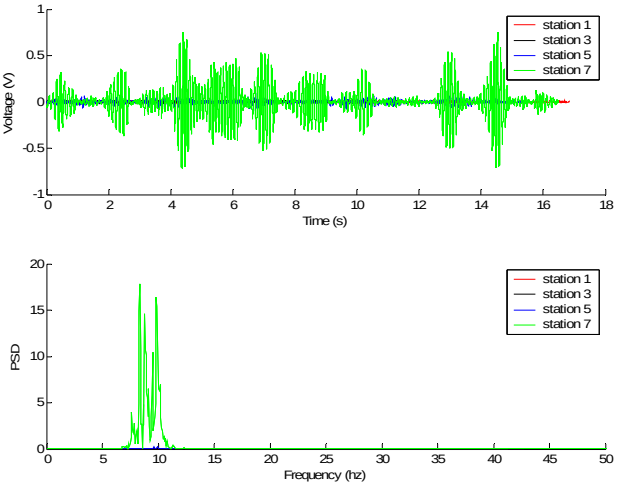

Figure B-1: A plot of Voltage v. Time and PSD v. Frequency for cylinder A at all stations.

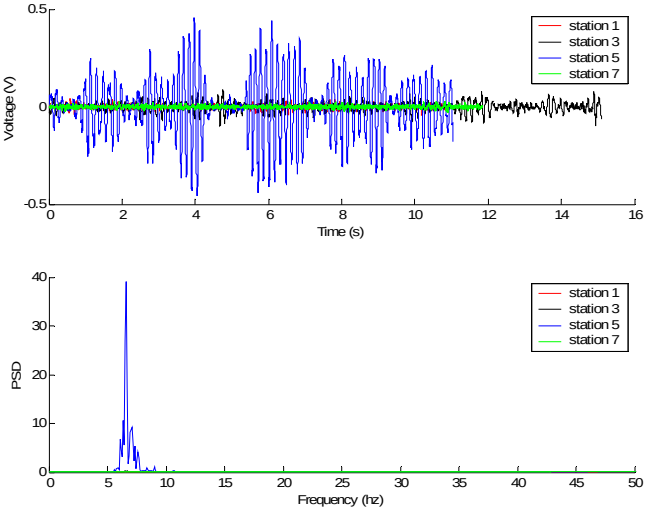

Figure B-2: A plot of Voltage v. Time and PSD v. Frequency for cylinder B at all stations.

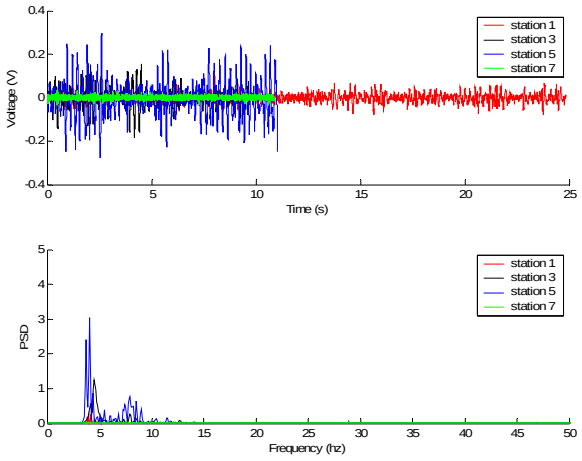

Figure B-3: A plot of Voltage v. Time and PSD v. Frequency for cylinder C at all stations.

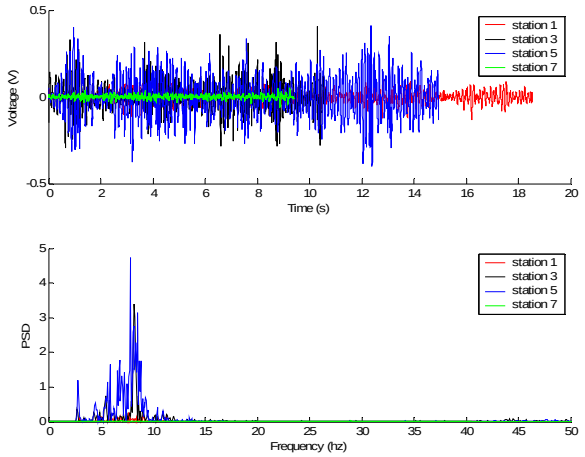

Figure B-4: A plot of Voltage v. Time and PSD v. Frequency for cylinder D at all stations.

4.30.05

The next experiment investigated blowing versus non-blowing for the sharp leading sharp trailing air foil. First, the air foil was tested with zero cross flow at zero and max blowing. Figure B-6 shows that blowing does add a small amount of energy to the system but do to limitations of the accelerators we are unable to detect exact frequencies.

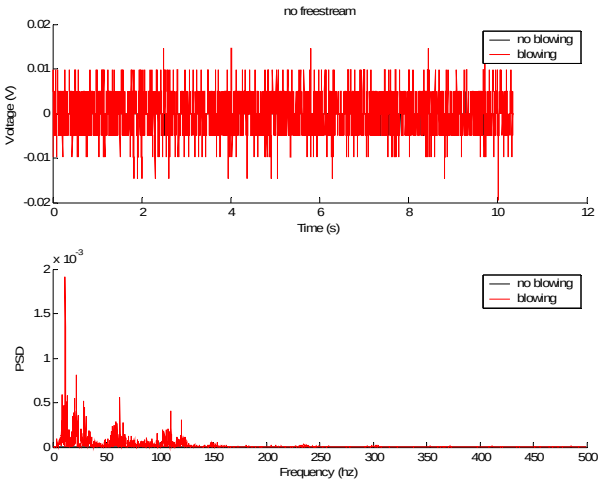

Figure B-5: A plot of both Voltage v. Time and PSD v. Frequency for non-blowing and max blowing. Accelerometer measurements are corrupt.

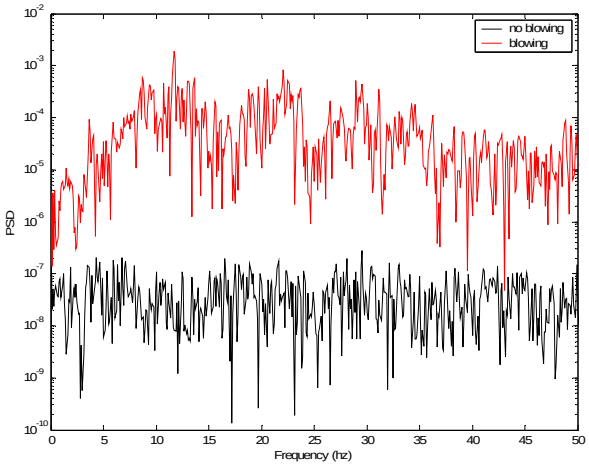

Figure B-6: A plot of PSD for non-blowing and max blowing.

5.01.05

This experiment was similar to the previous experiment as it tested non-blowing and max blowing but here a cross flow was used to impart vibration onto the air foil.

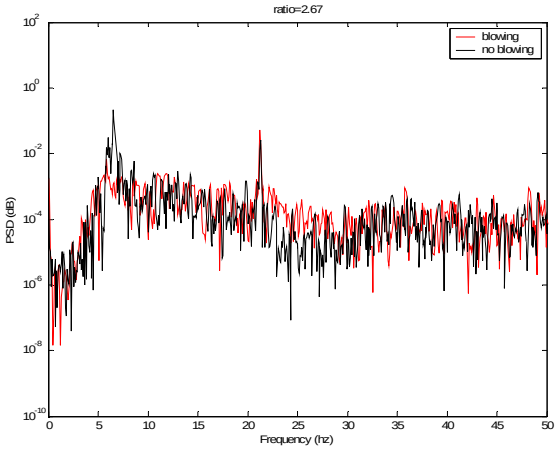

Figure B-8: A plot of PSD v. frequency for cylinder A at station 3 in a cross flow of 0.45 m/s.

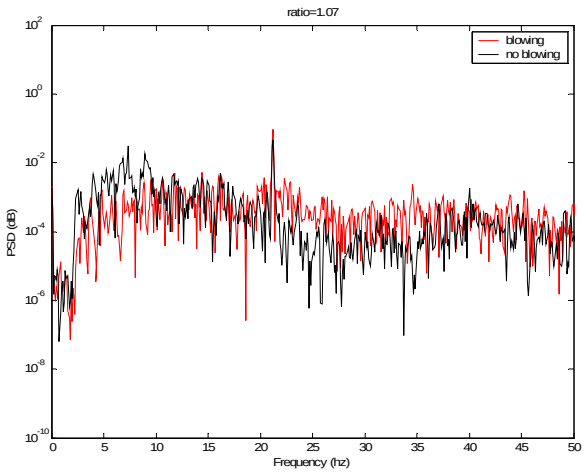

Figure B-9: A plot of PSD v. frequency for cylinder C at station 3 in a cross flow of 0.45 m/s.

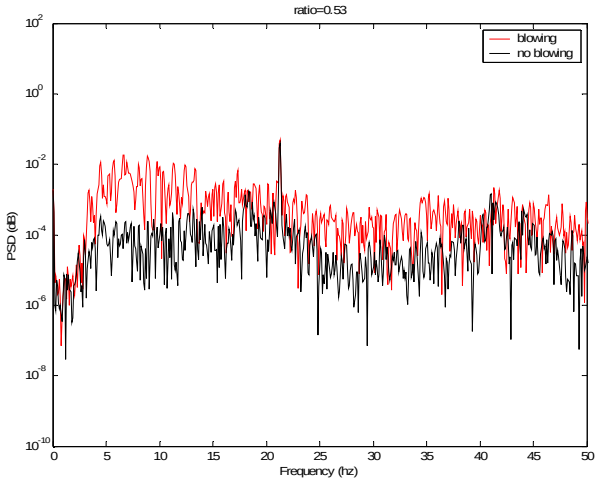

Figure B-10: A plot of PSD v. frequency for cylinder E at station 3 in a cross flow of 0.45 m/s.

5.25.05

Here the experiments ran into a problem with equipment failure. It was noticed that the accelerometers would start giving high voltages at random locations. This problem slowed down the data collection process as it made most measurements useless. Figures A-11 through A-13 shows examples of these high voltages and there effect on the frequency spectrum.

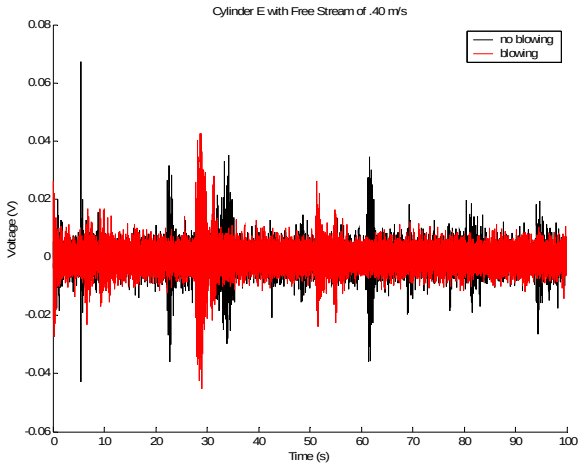

Figure B-11: A plot of Voltage v Time cylinder E with and without blowing. The spikes are random noise from the accelerometers.

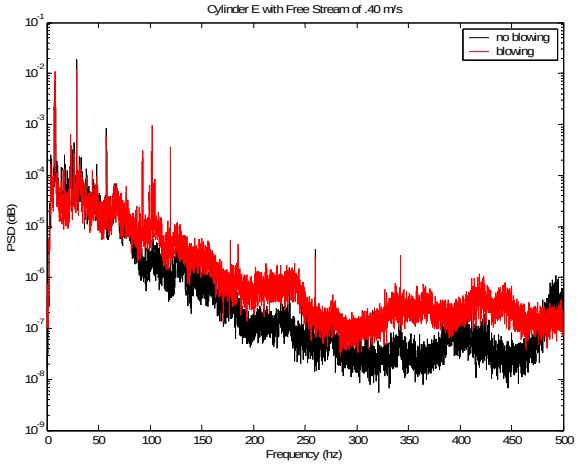

Figure B-12: A plot of PSD v. Frequency for the Voltage v Time data in the above plot.

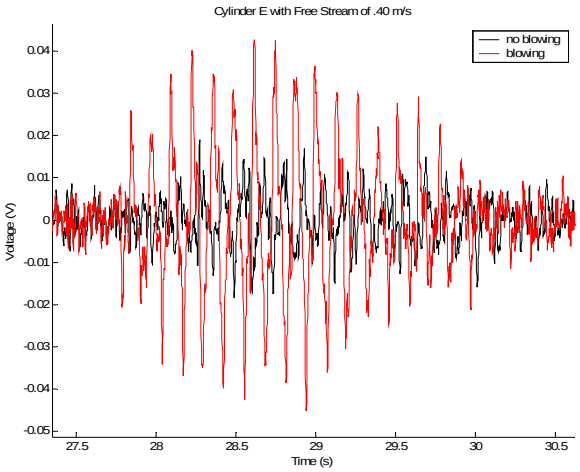

Figure B-13: Zoomed in plot of the voltage plot in Figure B-11. Here the noise from the accelerometers can be seen.
6.09.05

For cylinder E, here is a comparison of the spectra for various c_mu. .

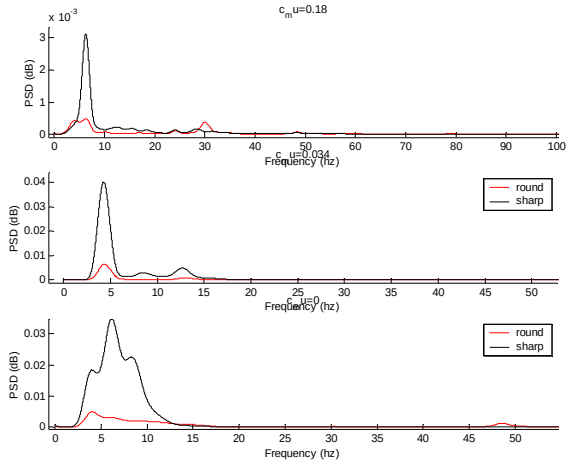

Figure B-14: A plot of PSD Magnitudes v Frequency comparing different blowing speeds for round and sharp leading edge air foils.

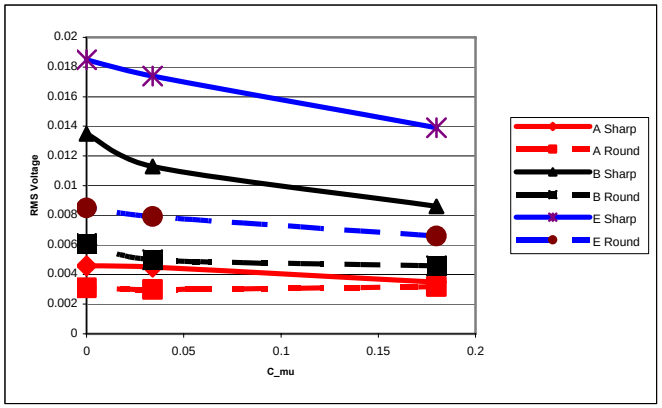

Figure B-15: This is the RMS values for all cylinders and both round and sharp and all c_mu's. Round is better.

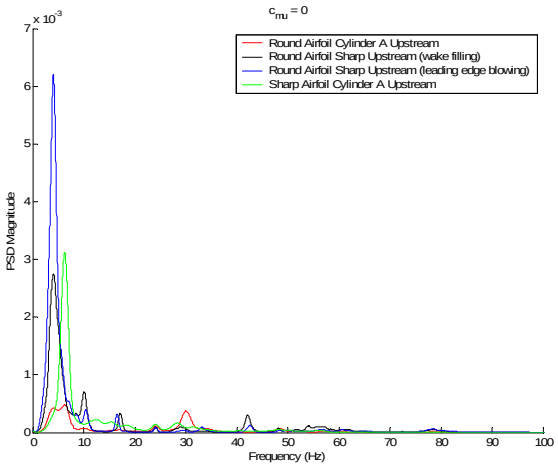

Figure B-16: This is the RMS values for all cylinders and both round and sharp and all c_mu's. Round is better.

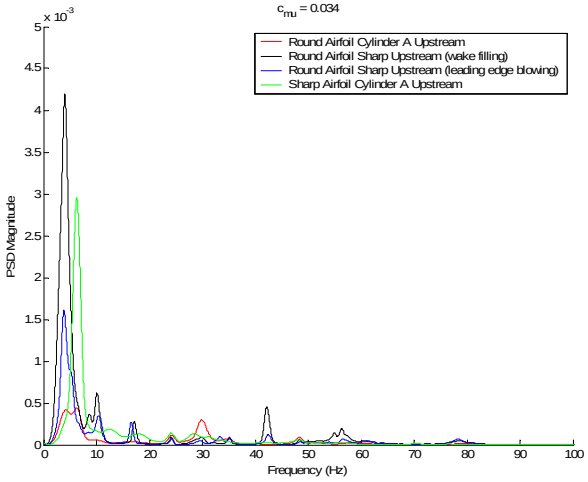

Figure B-17: This is the RMS values for all cylinders and both round and sharp and all c_mu's. Round is better.

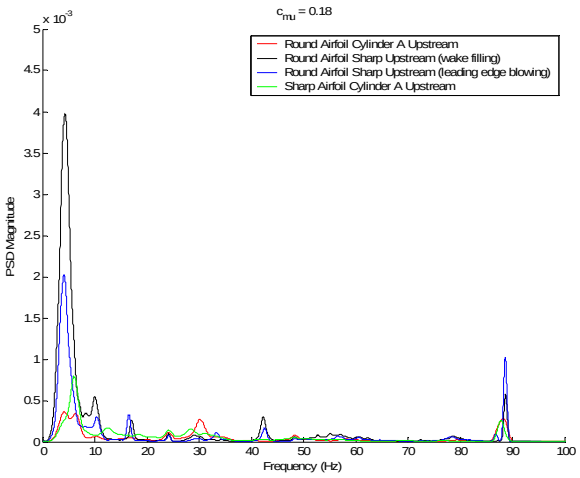

Figure B-18: This is the RMS values for all cylinders and both round and sharp and all c_mu's. Round is better.

6.11.05

This experiment again studied waking filling as well as leading edge blowing. Figures A-19 to A-21 show the effects of different blowing conditions on the vibration of the air foil. Each plot compares all of the different experimental set ups with a single blowing condition.

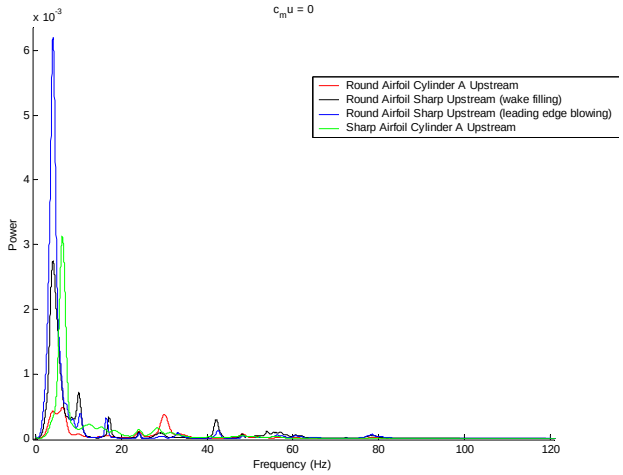

Figure B-19: PSD v Frequency for wake filling and leading edge blowing with Cμ=0.0.

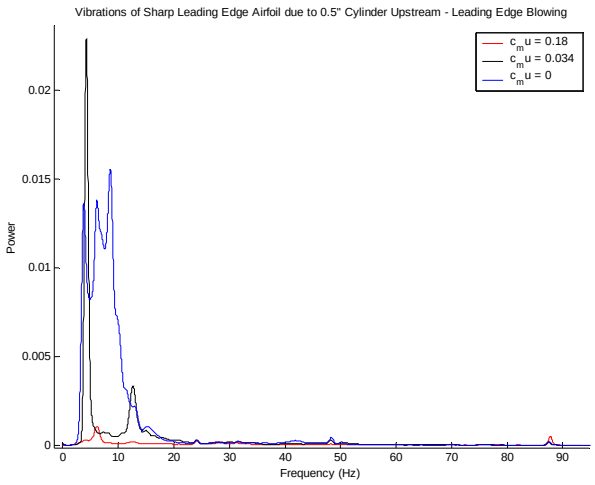

Figure B-20: PSD v Frequency for the sharp leading edge air foil due to a 0.5" cylinder upstream.

7.07.05

Here, vibration measurements where taken on a sharp leading edge air foil due to the wake of an upstream cylinder. The cylinder size and location was changed in order to create different strength vibrations with different frequencies.

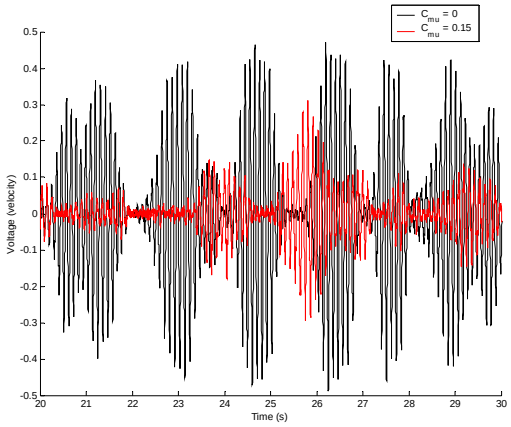

Figure B-21: Voltage v Time for blowing and non blowing for the sharp leading edge air foil.

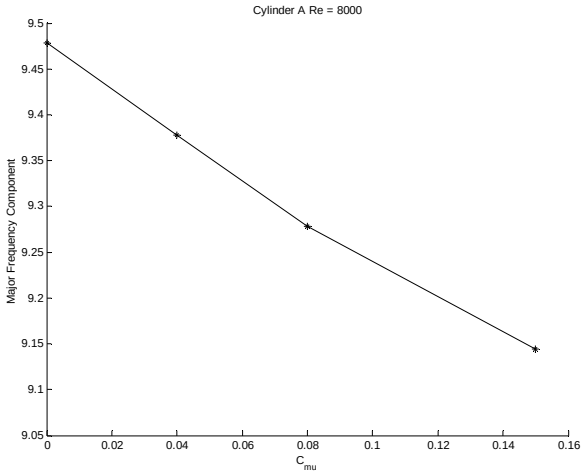

Figure B-22: Motor Frequency v Cμ Re = 8000. All points are the Root Mean Square of the total signal.

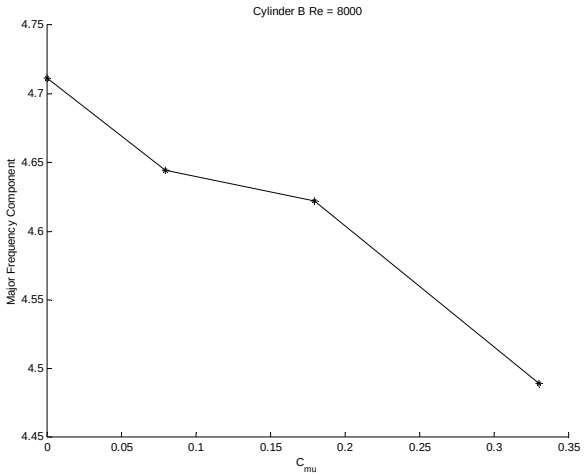

Figure B-23: Motor Frequency v Cμ for Re = 8000. All points are the Root Mean Square of the total signal.

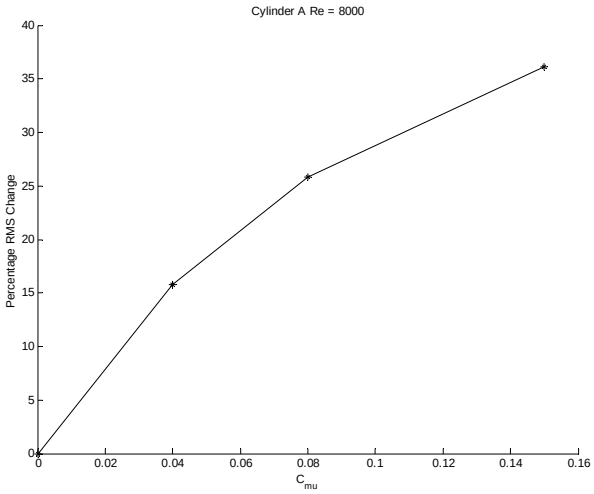

Figure B-24: Percentage change in RMS v Cμ for Re = 8000. All points are the Root Mean Square of the total signal.

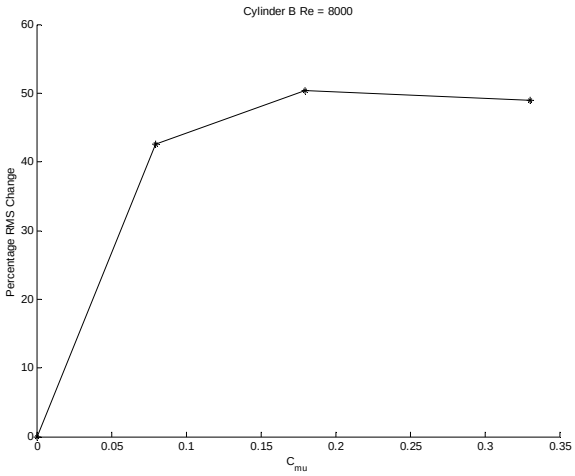

Figure B-25: Percentage change in RMS v Cμ for Re = 8000. All points are the Root Mean Square of the total signal.

8.29.05

The next experiment was a more in depth look into wake filling. Here, 10 different Cμ where tested. Root mean squared values and vibration reduction plots are shown below.

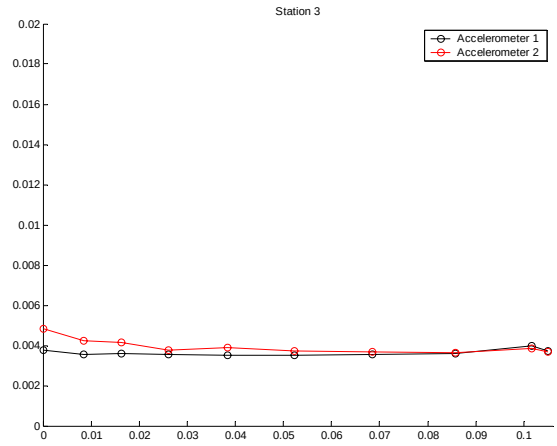

Figure B-26: Root mean square v Cμ for wake filling.

This experiment extensively examined the vibration on a sharp leading edge air foil due to the wake of different circular cylinders. Two Reynolds number where used, Re = 8000 and Re = 20200.

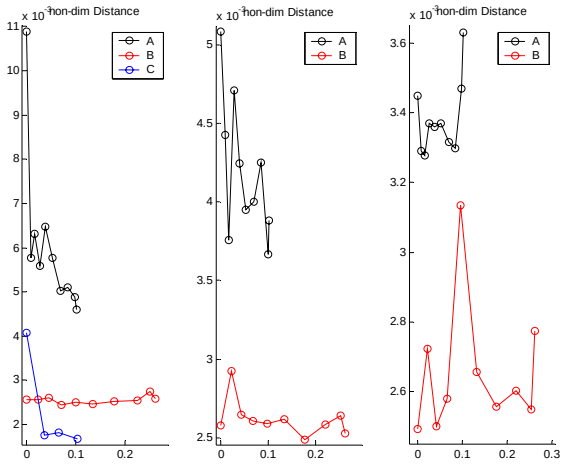

Figure B-27: Voltage v Location for vibration due to a circular cylinder upstream on the sharp leading edge air foil. Re = 8000.

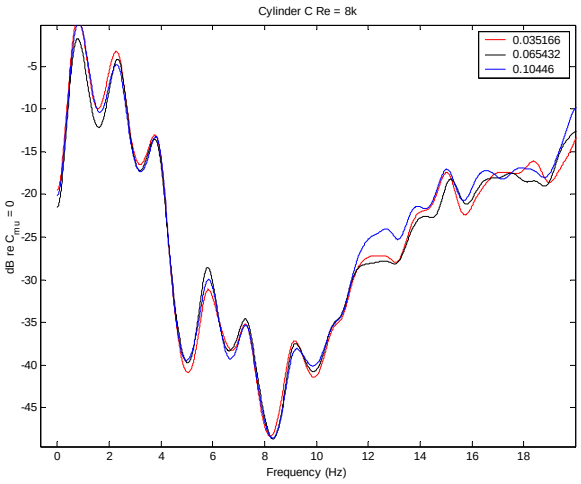

Figure B-28: dB Reduction v Frequency for sharp air foil using 3 Cμ, Re=8000 and cylinder B upstream. The location for this plot is location 2.

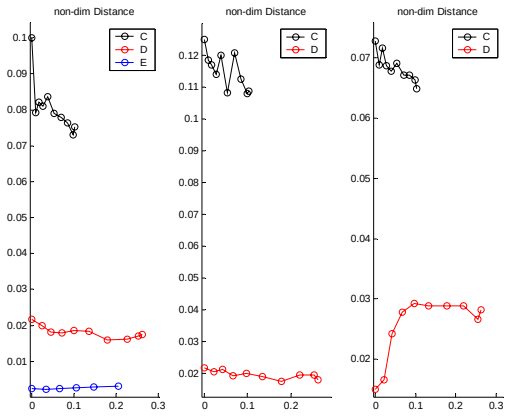

Figure B-29: Voltage v Location for vibration due to a circular cylinder upstream on the sharp leading edge air foil. Re = 20200.

Here the same experiment was done again with the only difference being that the sharp leading edge air foil was replaced with the round leading edge air foil. The same Reynolds numbers and condutions where used.

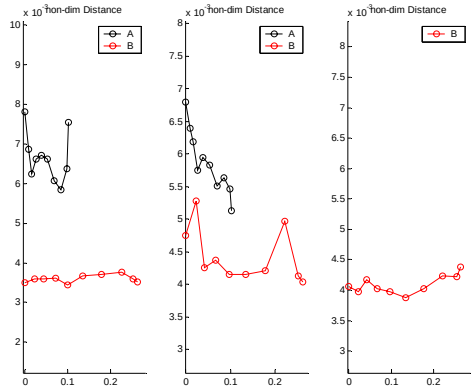

Figure B-30: Voltage v Location for vibration due to a circular cylinder upstream on the round leading edge air foil. Re = 8000.

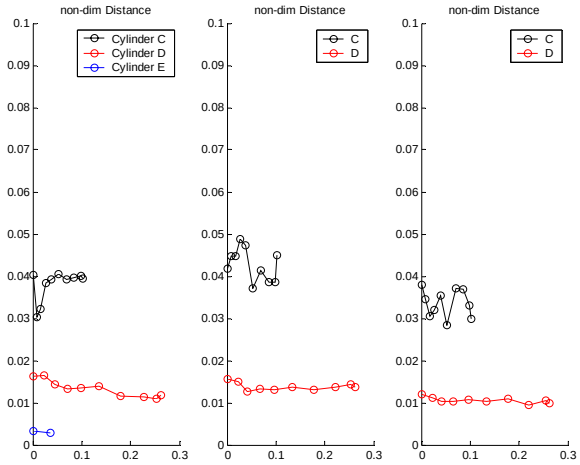

Figure B-31: Voltage v Location for vibration due to a circular cylinder upstream on the round leading edge air foil. Re = 20200.